Photophysics and Photosensitizing Mechanism of Thiothymines Investigated Using Multi-Reference Quantum Chemistry

A thesis

submitted towards partial fulfilment of

MS-PhD Dual Degree

by

Meghna A. Manae

20122033

Indian Institute of Science Education and Research Pune

2019

For my grandmother,

Yashoda Suryavamshe,

her grace and resilience.

"It's not the note you play
that's the wrong note
– it's the note you play afterwards
that makes it right or wrong."
– Miles Davis

"Now, here, you see,
it takes all the running you can do,
to keep in the same place.
If you want to get somewhere else,
you must run at least twice as fast as that."
– The Red Queen
'Through the Looking-Glass'
by Lewis Caroll

Declaration

I declare that this written submission represents my idea in my own words and where others' ideas have been included; I have adequately cited and referenced the original sources. I also declare that I have adhered to all principles of academic honesty and integrity and have not misrepresented or fabricated or falsified any idea/data/fact/source in my submission. I understand that violation of the above will be cause for disciplinary action by the Institute and can also evoke penal action from the sources which have thus not been properly cited or from whom proper permission has not been taken when needed. The work reported in this thesis is the original work done by me under the guidance of Dr. Anirban Hazra.

(Ms. Meghna A. Manae)

Reg. No. 20122033

Pune, India

29th August, 2019

Certificate

I certify that the thesis entitled "Photophysics and Photosensitizing Mechanism of Thiothymines Investigated Using Multi-Reference Quantum Chemistry" presented by Ms. Meghna A. Manae represents her original work which was carried out by her at IISER, Pune under my guidance and supervision during the period from August 2014 to July 2019. The work presented here or any part of it has not been included in any other thesis submitted previously for the award of any degree or diploma from any other University or institutions. I further certify that the above statements made by her in regard to her thesis are correct to the best of my knowledge.

Anirban Hazra

Pune, India
29th August, 2019

(Dr. Anirban Hazra)
Associate Professor
Department of Chemistry

Acknowledgements

Through the years of my PhD, I am grateful for the support, kindness, and patience of my advisor, Dr. Anirban Hazra. Quite apart from science, I have learnt much about how to ask questions and then go about finding the answer, and have a greater appreciation for the importance of being critical and thorough. I deeply admire his ability to get thoroughly involved in any task at hand, and it is my hope that I can carry at least some part of his attitude with me.

Several people have been key in helping me through these years and I would like to take this opportunity to thank them.

Dr. Debashree Ghosh and Dr. Arnab Mukherjee, my Research Advisory Committee members for their encouragement, advice, and extensive discussions. Dr. Amrita Hazra, for helping me see an electronic structure problem from a new and different perspective.

IISER Pune, for the wonderful facilities that made my work possible.

Dr. Avdhoot Datar and Dr. Mahesh Gudem, my two colleagues who were with me through most of my PhD. Mahesh never hesitated to answer any question I had, no matter how simple, and no matter how busy he was. Avdhoot has been my pillar of support, constantly allaying my fears and uncertainties.

Dr. Reman Singh, my dear friend, who has always been great company. His open-mindedness and wonderful perspective on life will always stay with me.

Dr. Padma Balasubramanya, because of whom I fell in love not just with chemistry, but also with teaching.

Satyam, for his faith in me, and his own journey as a PhD student that has inspired me. Jyotirmoy, for all the helpful discussions. Anju, for being a wonderful roommate, and making me forget that I was away from home for the very first time. Aditi, for her bright smile that always lit up the room, and Sneha, for never letting anxieties rule my

life. Hridya, for her calm and optimistic attitude. Vikas, for being far more annoying than little brothers are allowed to be.

Punya, who has always inspired me by being so full of passion, determination and courage. Apart from being amazing, she also takes the time to calm me down every time I am on the verge of a nervous breakdown.

VK Bharadwaj, for being the free spirit that he is. Kiran, for always listening to me with so much patience. Suraj *Anna,* for making Group Theory seem comprehensible and teaching me the difference between a lemma and a corollary. Vinay, for the innumerable cups of coffee we shared.

Ma and *Pa,* for their unconditional support and understanding, despite my work being completely alien to them. But particularly, for teaching me what is most important in life. Abhinay, for his brutal honesty. *Ba,* for her immense love and bedtime stories. *Baba,* for his enormous, if somewhat misplaced, pride in me. Vinod *mama,* for his encouragement, and Harsha *mama,* for the early physics lessons.

Finally, I thank Yagyik Goswami, for being my rock when I needed the support, and a punching bag when I needed to vent. The last few years have been more vibrant because you were in them.

Abstract

Thymine, a DNA nucleobase, when photoexcited, relaxes to the ground state on an ultrafast timescale. In contrast, when one or both oxygen atoms in thymine are replaced with sulphur (yielding three different thiothymines), the molecule on photoexcitation populates its triplet excited state with near unity yield. Thiothymines also exhibit a redshift in their absorption spectrum compared to thymine, and in their triplet state, are able to photosensitize ground state oxygen to singlet oxygen. These photoproperties make thiothymines potential drugs to be used in photodynamic therapy. Three major questions are addressed in this work, all of which focus on understanding how position of substitution affect these photoproperties. Wavefunction-based multi-reference electronic structure methods, specifically, complete active space self-consistent field (CASSCF) and its extensions have been used.

First, we explain the absorption spectra, where, substitution at the 4th position (4-thiothymine) exhibits a significantly higher redshift as compared to thionation at the 2nd position (2-thiothymine). We find that this unexpected trend can be attributed to an interplay between two types of delocalization in thymine: one due to conjugation with a double bond and the other owing to the size of the atom substituted. This work demonstrates that studying substitutions in isolation can be misleading, and the intrinsic features of the parent molecule need to be considered. Also, this study shows that the well-established idea of delocalization is not just affected by conjugation with another pi system, but is also influenced by the size of atoms.

Second, we look at how position of substitution affects triplet lifetimes since 4-thiothymine was found to have a longer triplet lifetime than 2-thiothymine. This difference arises from the decay dynamics of 2-thiothymine being distinct from that of 4-thiothymine and 2,4-dithiothymine. The findings regarding absorption spectra and

triplet lifetimes of thiothymines were extended to another molecule, xanthine, to evaluate their generality. This molecule highlights the generality of absorption properties amongst thiobases, while suggesting prudence in making predictions about excited state properties, especially when excited state structures vary significantly from ground state structures.

Finally, we have investigated the mechanism of photosensitization, and calculated the rates of photosensitization of oxygen by thiothymines. Recently, a method built on certain classical approximations was proposed. In our work, we have employed a time-dependent variant of Fermi's Golden rule, where the treatment is purely quantum mechanical. We believe this is the first instance where this rate expression has been used for bimolecular nonradiative energy transfer.

Contents

Declaration **i**

Certificate **ii**

Acknowledgements **iii**

Abstract **v**

List of Figures **xi**

List of Tables **xv**

1 Introduction **1**

1.1 Role of Computational Studies 5

1.2 Outline of Thesis 5

2 Theoretical Background and Computational Methods **9**

2.1 The Born-Oppenheimer Approximation 10

2.2 Electronic Structure Methods 13

2.3 Nonradiative Transition Rates 20

3 Dependence of Absorption Spectra of Thiothymines on Position of Sulphur Substitution **23**

3.1 Computational Methodology 25
3.2 Hypothesis for the Nature of the LUMO 25
3.3 PIB Model and Prediction for 2SeThy 31
3.4 Role of Cyclic Delocalization and Limitations of the Hypothesis 36
3.5 Effect on Electrophilicity 39
3.6 Conclusions 40

4 Dependence of Triplet Lifetimes of Thiothymines on Position of Sulphur Substitution 43

4.1 Computational Methodology 44
4.2 Effect of Position of Thionation on Triplet Decay Dynamics 45
4.3 Electronic Delocalization Modulates the Energy of the Triplet Minima . . 53
4.4 Design of New Photodynamic Therapy Drugs 53
4.5 Conclusions 56

5 Dependence of Photoproperties of Thioxanthines on Position of Sulphur Substitution 59

5.1 Computational methodology 61
5.2 Electronic Spectra of Thioxanthines 61
5.3 Predictions of the Particle-in-a-Box Model 64
5.4 Topology and Dynamics of the T_1 State of Thioxanthines 67
5.5 2-Thioxanthine: A Cautionary Tale 70

6 How Thiothymines Generate Singlet Oxygen Through Photosensitization 75

6.1 Physical Interpretation of Photosensitization 77
6.1.1 R space and the mode to promote crossing 77
6.1.2 D space and diabatic coupling 79

6.2 Fermi's Golden Rule 81
6.2.1 Classical limit of Fermi's golden rule 82
6.2.2 Time-dependent variant of Fermi's golden rule 83
6.3 Orientation Directions Based on Orbital Overlap 89
6.4 Rates of Photosensitization 90
6.4.1 Computational Methodology 90
6.4.2 Rates with classical limit of Fermi's golden rule 91
6.4.3 Rates with time-dependent variant of Fermi's golden rule 93
6.5 Mechanistic Insights into Photosensitization 94

List of Publications **101**

References **105**

List of Figures

1.1 Canonical DNA and RNA nucleobases. 1

1.2 Thiobases: sulphur substituted nucleobases 2

1.3 Schematic representation of photodynamic therapy 4

2.1 Schematic of the orbital space in CASSCF 18

3.1 Molecules studied in this chapter 23

3.2 Active space of 14 electrons in 10 orbitals used in this study 26

3.3 LIIC scans along rotation of methyl group for thymine 27

3.4 Orbitals characterizing electronic transitions to lowest two bright states . 29

3.5 Transitions characterizing first two bright states in thymine and thiothymines 30

3.6 Two types of delocalization in thymine modeled by the particle-in-a-box . 31

3.7 Particle-in-a-box models for C^2=X and C^6=C^5–C^4=X systems. 33

3.8 HOMO and LUMO energies for the C=X and C=C–C=X systems 34

3.9 LUMO energies for the C=X and C=C–C=X systems 35

3.10 Resonance structures of thymine 36

3.11 Aliphatic models constructed by breaking the thymine ring 37

3.12 Orbitals of aliphatic models constructed by breaking the thymine ring . . 38

4.1 Molecular geometries along with orbitals of both triplet minima of thiothymines 46
4.2 Molecular geometries along with orbitals of both triplet minima of thymine 47
4.3 LIIC scan between both T_1 minima in 2tThy with diabatic states 47
4.4 LIIC scans connecting both T_1 minima of thiothymines 49
4.5 Two types of MECPs in the thiothymines 49
4.6 LIIC scans connecting T_1 minimum to respective MECP 51
4.7 Orbital energies of model π systems 54
4.8 2tThy analogues with electron withdrawing and donating groups 54
4.9 Redshifts/Blueshifts seen in 2tThy analogues 55

5.1 Structure of xanthine and its chalcogen substituted derivatives 60
5.2 Active space used for xanthine and its derivatives 61
5.3 Transitions characterizing first two bright states in Xan and thioxanthines 64
5.4 Particle-in-a-box models for C^2=X and C^8=N^9—C^4=C^5—C^6=X systems. 66
5.5 HOMO and LUMO energies for C^2=X and C^8=N^9—C^4=C^5—C^6=X systems. 67
5.6 LUMO energies as calculated from the Particle-in-a-box model. 68
5.7 Orbitals characterizing electronic transitions to lowest two bright states. . 69
5.8 Structures of both minima on the T_1 PES of Xan and thioxanthines. . . . 70
5.9 LIIC scans connecting the two T_1 minima of Xan and thioxanthines . . . 71
5.10 Minimum energy crossing points of Xan and thioxanthines 72
5.11 Energies of originating orbitals of T_1 minima in 2tThy and 2tXan 73
5.12 Energies of terminating orbitals of T_1 minima in 2tThy and 2tXan 74

6.1 Molecular orbital diagrams of ground and excited states of O_2. 76
6.2 Schematic showing the ordering of states for the PS–O_2 composite system in R space 78

6.3 Schematic showing the states of the PS–O_2 composite system in D space . 79
6.4 Diabatic calculated from D space 80
6.5 Real part of the correlation function 87
6.6 The 3 approach directions studied in this work 89
6.7 Photosensitizing rates using classical approximation of Fermi's golden rule 92
6.8 Comparison of barrier calculations 93
6.9 Photosensitizing rates using the time-dependent variant of Fermi's golden rule 94
6.10 Diabatic couplings plotted as a function of D for all thiothymines 95
6.11 Boltzmann factors as a function of D for all thiothymines 96
6.12 Calculated energies of states in the D space for a representative system . 98
6.13 Hartree-Fock and MP2 energies in the D space 99

List of Tables

1.1 Experimental photoproperties of thiobases 3

3.1 Vertical excitation energies of thymine and thiothymines 28
3.2 Vertical excitation energies of selenothymines 28
3.3 HOMO and LUMO energies for the different π systems from the PIB model. 32

4.1 Some geometrical parameters for thymine and thiothymines 48
4.2 Energetic and topological parameters of thymine and thiothymines 50
4.3 Energetic and topological parameters for 2-thiothymine and 2-thiouracil. . 52
4.4 Energies of orbitals and triplet minima of 2-thiothymine analogues 55
4.5 Spin-orbit coupling values of the MECPs of 2-thiothymine analogues . . . 56

5.1 Vertical excitation energies of xanthine and the thioxanthines. 62
5.2 Vertical excitation energies of selenoxanthines and teluroxanthines. 63
5.3 HOMO and LUMO energies for the different π systems from the PIB model. 65
5.4 Spin-orbit couplings of the MECPs of xanthine and the thioxanthines. . . 72

6.1 Integral values of FCWD(τ) for different time intervals 88
6.2 Value of FCWD with the use of different damping parameters 88

Chapter 1

Introduction

Purine bases, adenine and guanine, and pyrimidine bases, cytosine, thymine, and uracil (Figure 1.1), are one of three components of a nucleotide – the monomer in DNA and RNA. In nucleotides, these bases, otherwise called nucleobases, function as fundamental units to encode genetic information. Apart from the ubiquitous presence of nucleobases in the human body, several substituted derivatives of these canonical nucleobases, are also present for various other functions [1–3]. One such class of nucleobase derivatives are thiobases, shown in Figure 1.2, in which one or more of the exocyclic oxygen atoms (indicated in bold in Figure 1.1) are substituted with sulphur [1].

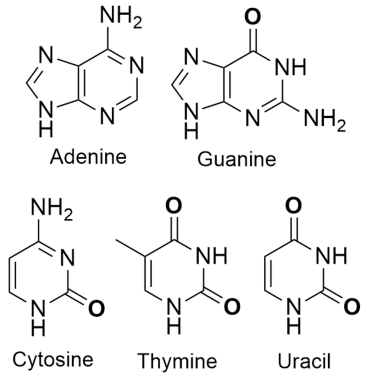

Figure 1.1: The canonical DNA and RNA nucleobases with the exocyclic oxygen atoms indicated in bold.

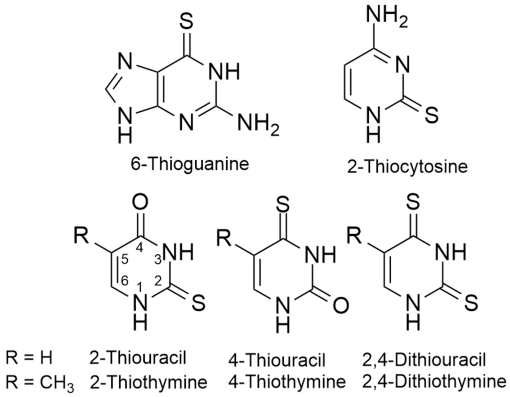

Figure 1.2: The eight possible thiobases obtained by substituting the exocyclic oxygen in canonical nucleobases with sulphur.

Some thiobases occur naturally in tRNAs (transfer RNA), where their predominant functions include improving translational efficiency, regulating cellular processes, and protecting tRNA from oxidative stress [4, 5]. Owing to their chemical and biological properties, thiobases have found wide use in therapeutics since the late 1980s, with four thiobases included in the 'WHO Model List of Essential Medicines'. They have been effective as anticancer, anti-inflammatory [6], and immunosuppressant drugs[7] and also used in the treatment of hyperthyroidism [8].

In the past decade, they have received renewed attention for their photoproperties, and in particular, the significant difference in their photoproperties compared to canonical nucleobases [9, 10]. Firstly, the absorption maxima of thiobases are redshifted with respect to the absorption maxima of the parent molecule. The canonical nucleobases mainly absorb in the UVC (100–280 nm) region [11–13], while thiobases generally absorb in the UVB–UVA (280–400 nm) region [10, 14, 15] as shown in Table 1.1. This general redshift can be explained on the basis of the thionyl double bond being weaker than the carbonyl double bond. Secondly, thiobases are found to have an ultrafast intersystem crossing (ISC) rate with a near unity triplet yield, following photoexcitation (see Table 1.1). Meaning, following photoexcitation, a large population of the thiobase

Table 1.1: Experimental photoproperties of thiobases.

Thiobase	λ^a_{max} (nm)	τ^b_{ISC} (fs)	Φ^b_T	Φ^c_Δ
2-thiothymine	275	620	0.90	0.36
4-thiothymine	335	240	0.85	0.42
2,4-dithiothymine	363	180	0.90	0.46
2-thiouracil	265	360	0.75	
4-thiouracil	328	240	0.90	0.49
2,4-dithiouracil	351	220	0.90	0.49
2-thiocytosine	269	210	0.90	
6-thioguanine	341	560	0.60	0.58

[a]Absorption maxima in phosphate buffer solution at pH 7.4. [b]Intersystem crossing lifetime.
[c]Triplet yield. [d]Singlet oxygen yield. Values taken from References [10, 14, 15]

crosses over to the triplet manifold [9, 10, 14]. Canonical nucleobases on the other hand, return to the ground state on an ultrafast timescale following photoexcitation [16, 17]. Thirdly, owing to their high triplet population and excess energy, thiothymines are able to photosensitize oxygen [14]. This means, a thiobase in its triplet state, transfers its excess energy to an oxygen molecule and electronically excites the oxygen molecule from its ground triplet to its singlet state. Singlet oxygen yields, which are given in Table 1.1 for various thiobases, are a quantitative measure of the photosensitizing ability of a molecule.

The photoproperties of thiobases – a redshift in their absorption, high triplet population and photosensitizing ability, make them attractive options as photodynamic therapy (PDT) drugs [18–20]. Photochemotherapy or PDT is a therapeutic technique which uses light and a photosensitizer [21, 22]. It is used in the treatment of age-related macular degeneration of the eye, psoriasis, atherosclerosis, and herpes. Importantly, PDT is used to treat malignant tumors, including those that occur in the lungs, bladder, head and neck, and skin [21,23]. Being a minimally invasive and a very targeted form of treatment, the most important advantage it offers in lieu of conventional cancer therapies such as chemotherapy and radiation therapy, is its lack of side effects.

The flow chart in Figure 1.3 depicts the steps in PDT [24]. The PDT drug is either

ingested or administered topically, and the drug is designed to get accumulated in diseased tissue. After adequate accumulation, the affected area is irradiated with light of appropriate frequency. Typically, the PDT drug gets photoexcited and its population undergoes ISC from its bright singlet state to a triplet electronic state. This excited molecule functions as a photosensitizing agent and converts molecular oxygen present in the cell to its singlet state [23, 24]. Singlet oxygen is an example of a reactive oxygen species, is highly toxic and causes cell death.

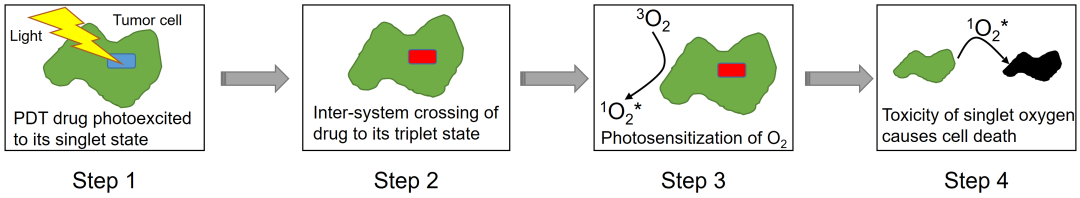

Figure 1.3: Schematic representation of photodynamic therapy.

While photoproperties of canonical nucleobases have been extensively studied [25], there remain several unanswered questions regarding the photoproperties of thiobases. In this thesis, we focus on the photoproperties of thiothymines, with three principal motivations. Firstly, since thymine has two exocyclic oxygen atoms, labeled as positions 2 and 4 (by convention), this allows for sulphur substitution at either position (2-thiothymine and 4-thiothymine) or both positions (2,4-dithiothymine). Therefore, photoproperties can be studied from a position-dependent perspective. Secondly, investigating these particular photoproperties, all of which make for an ideal PDT drug, would help in the design of better PDT drugs [18]. Thirdly, thiothymines present us with an opportunity to better understand the mechanism of photosensitization. Further, since all three thiothymines have significant photosensitizing abilities as evidenced by their singlet oxygen yields (Table 1.1), the photosensitizing rates can be calculated relatively.

1.1 Role of Computational Studies

Quantum chemical computations can help us investigate the photophysical properties of thiothymines. The excitation energies can be calculated to a high degree of accuracy, the molecular orbitals involved in the excitation can be closely studied, and the exact origin of redshift in the thiothymines can be identified. Theoretical calculations can also help us understand the photophysics following photoexcitation. The pathway taken by the thiothymine can be mapped in detail and help in understanding why the molecule prefers to undergo ISC instead of returning to the ground state, unlike its canonical counterpart [26]. Further, features of its triplet state can be studied including the structural changes it undergoes upon reaching the triplet state. This will contribute to estimating how long the molecule will spend on its triplet state before it finally loses the excess energy and returns to the ground state.

Photoexcitation and ISC have been studied extensively, and established protocols already exist to study these processes. To study photosensitization, however, models are still being explored [27, 28]. These existing methods can be improved to better understand the mechanism of photosensitization. This would not only help us gain useful insights into photosensitization but also aid in the development of a model for bimolecular nonradiative energy transfer in general.

1.2 Outline of Thesis

The title of this thesis refers to 'multi-reference' quantum chemical methods, which are most suited for studying excited states. The reasons for their suitability, along with some basic theory underlying the multi-reference methods used in this work have been discussed in Chapter 2.

An unexpected trend is observed in the redshift in absorption across the thiothymines, with 4-thiothymine (4tThy) exhibiting a higher redshift as compared to 2-thiothymine

(2tThy). The reason for this position-dependent trend in redshift is investigated in Chapter 3. It is seen that the carbonyl in the fourth position in the parent nucleobase, thymine, is conjugated with a neighboring carbon-carbon double bond, thus lowering the energy of these π orbitals significantly in comparison to the π orbitals of the carbonyl at the second position. Moreover, either of the carbonyl bonds can gain additional stability when the size of the atom substituted is large. We hypothesize that an interplay between these two stabilization effects is responsible for the observed trend in redshift. This proposition is supported by ab initio quantum chemical calculations and a simple particle-in-a-box model.

With regard to the triplet lifetimes of the thiothymines, 4tThy is found to have a longer triplet lifetime than 2tThy. A detailed study of the triplet excited state also reveals that 2tThy can exist in two possible conformers, while one conformer predominates in 4tThy. These differences of the triplet lifetimes and structures are studied in Chapter 4. The reason why 2tThy has two possible structures and 4tThy has only one can be tied back to the orbital energy trends, discussed in Chapter 3. Position of sulphur substitution also affects the triplet decay dynamics, with 2tThy having different decay pathway compared to 4tThy and 2,4-dithiothymine (dtThy). The difference in decay pathways is found to be responsible for the longer triplet lifetime of 4tThy compared to 2tThy. It is also shown that a thorough understanding of the electronic structure of thiothymines can help us manipulate excited state properties such as redshift in absorption and triplet lifetime.

In Chapter 5, we evaluate the generality of the findings of Chapters 3 and 4, regarding position-dependent trends in redshift and triplet lifetimes. We do this by repeating these investigations on thioxanthines – another class of thionated purine bases, with two possible sites of thionation. We make predictions for trends in redshift and possible conformers on the triplet state based on orbital energies. While the trends predicted for redshifts hold, the trends regarding the structures on the triplet state are no longer

valid. This implies that the orbital energies obtained at the Franck-Condon geometry (minimum energy structure on the ground state) are reliable indicators of redshift in absorption, but are inadequate to make predictions about excited state properties.

In Chapter 6, we investigate the mechanism of photosensitization of oxygen by triplet thiothymines. Although experimental photosensitization rates of 2tThy and 4tThy were found to be similar, a recently proposed method to calculate photosensitization rates, built on certain classical approximations, was unable to reproduce this [28]. We therefore use a time-dependent formalism of Fermi's golden rule to calculate the rates of photosensitization of thiothymines, where the treatment is purely quantum mechanical. To the best of our knowledge, this is the first instance where this rate expression has been used in the case of photosensitization.

Chapter 2

Theoretical Background and Computational Methods

The primary goal of quantum chemistry is to solve the electronic structure of molecules – the nonrelativistic time-independent Schrödinger equation. This includes, solving for the energies, and more importantly, the wavefunction, of electrons which are subject to the electrostatic field of the nucleus. Electronic structure calculations are made possible by the Born-Oppenheimer approximation, which is discussed in the first section of this Chapter. We then look at electronic structure methods in the second section, with a focus on studying electronically excited states. In the third section, transition between electronic states, in particular nonradiative transitions, and methods to calculate these transition rates are discussed.

Throughout this Chapter, precedence is given to physical insights, rather than rigorous mathematical formalism. This is also in part because the methods discussed here are well established and routinely used by computational chemists. A detailed description of these methods can be found in References [29], [30] and [31].

2.1 The Born-Oppenheimer Approximation

The total Hamiltonian of a molecule can be generally written as,

$$\hat{H} = \hat{T}_N + \hat{V}_{NN}(R) + \hat{T}_e + \hat{V}_{ee}(r) + \hat{V}_{Ne}(R, r) \tag{2.1}$$

where, $\hat{T}_N$ and $\hat{T}_e$ are kinetic energies of the nuclei and electrons, respectively. $\hat{V}$ represents the potential energy with subscripts NN and ee denoting nuclear-nuclear and electron-electron repulsion terms. The $\hat{V}_{Ne}(R, r)$ is the nuclear-electronic attraction, and the only term that depends on both the nuclear and electronic coordinates.

To start, the nuclei is assumed to be stationary because of which $\hat{T}_N$ becomes zero and the nuclear coordinates in $\hat{V}_{NN}(R)$ and $\hat{V}_{Ne}(R, r)$ become constants. Eq. 2.1 now becomes a purely electronic Hamiltonian,

$$\hat{H}_{el} = \hat{V}_{NN}(R) + \hat{T}_e + \hat{V}_{ee}(r) + \hat{V}_{Ne}(r; R) \tag{2.2}$$

Solving the Schrödinger equation for the electronic Hamiltonian,

$$\hat{H}_{el} \left|\psi(r; R)\right\rangle = E_{el}(R) \left|\psi(r; R)\right\rangle \tag{2.3}$$

gives the electronic energy, at a particular fixed nuclear configuration, R. Therefore, Eq. 2.3 would have to be solved several times by varying R, to get $E_{el}(R)$, as a function of the nuclear geometries. $E_{el}(R)$, along with $\hat{T}_N$, is then used to obtain a nuclear Hamiltonian, $\hat{H}_{nu}$,

$$\hat{H}_{nu} = \hat{T}_N + E_{el}(R) \tag{2.4}$$

and the corresponding Schrödinger equation,

$$\hat{H}_{nu}\chi(R) = E\chi(R) \tag{2.5}$$

According to the BO approximation, the total energy of the molecule, including both the electronic and nuclear components, is E, and the corresponding total wavefunction is $\psi(r;R)\chi(R)$.

The terms that are neglected within the BO approximation are the coupling terms between the electronic states as a result of nuclear motions, and this coupling is approximately proportional to $\langle\psi_i(r;R)|\hat{\nabla}_R\psi_j(r;R)\rangle$, where i and j are indices of the coupled electronic states. Neglecting these coupling terms results in the simplified product form of the total wavefunction, $\psi(r;R)\chi(R)$. The large difference in mass of the nucleus and the electrons, and correspondingly their different scales of motion, is the physical basis for this approximation. The coupling is inversely proportional to the electronic energy difference between two states. Therefore, the BO approximation is acceptable when the electronic energies, calculated for different electronic states, i.e., the eigenvalues of Eq. 2.3, are well separated, for all R.

Potential Energy Surface

The solution of $\hat{H}_{el}$, $E_{el}(R)$, is called the potential energy surface (PES). Within the BO approximation, each electronic state can be associated with its own PES, and the molecule essentially 'lives' on this PES, with its nuclear configuration determining its energy. To obtain $E_{el}(R)$, the $\hat{H}_{el}$ is computed repeatedly by infinitesimally changing R. Practically, however, it would be very expensive to solve $\hat{H}_{el}$ for every infinitesimal change in R. Typically, one or two important coordinates, which best represent the process being studied, are identified and the PES is constructed along these.

In every step of a 'relaxed scan', the coordinate under study is incremented and con-

strained, while the other coordinates are optimized. While relaxed scan calculations are considerably expensive, they are fairly accurate in terms of predicting the barriers and the pathway taken by the molecule. Often, it is not possible to identify a couple of important coordinates. In such cases, the PES is constructed using the 'linear interpolation in internal coordinates' or LIIC method. In LIIC, linearly interpolated geometries are generated between two critical points, and single point energy calculations are performed on all the generated points. A pathway is thus produced between the critical points. Since nuclear geometries are not allowed to relax in LIIC scans, they are significantly inexpensive calculations. However, the barriers calculated are not very accurate, and are upper bounds to the actual barriers [32]. LIIC scans are the predominant method used to calculate PESs in this thesis. In the following subsection, critical points which are required to construct LIIC paths are briefly discussed.

Critical points on the PES

The ground and excited states are described by different PESs, and therefore, every PES will generally have a different nuclear geometry with the lowest energy, i.e., the global minimum. Calculating these minima on excited PESs, or excited minima, are important since this is where the molecule will try to relax to on the corresponding PES.

So far, we have ignored the coupling between electronic states. This coupling, also called nonadiabatic coupling, cannot be ignored near those R where two or more electronic states are nearly degenerate. Geometries where two or more electronic states of the same spin multiplicity are degenerate are called conical intersections (CI), and such geometries are characterized by a breakdown of the BO approximation. These CIs essentially act as funnels through which the molecule can get transferred to a different electronic state nonradiatively on an ultrafast timescale.

Nuclear geometries which are points of degeneracy between two electronic states of different spin multiplicities lie on a multi-dimensional seam, and the minimum on this

seam is called a minimum energy crossing point (MECP). MECPs differ from CIs, in that their nonadiabatic coupling is zero. This is because the operator in the nonadiabatic coupling, $\hat{\nabla}_R$, does not depend on spin, so when it operates on two wavefunctions of different spin multiplicities, their spin parts do not get operated on by $\hat{\nabla}_R$, and go to zero because of their orthogonality.

$$\langle \psi_i(r,R)\alpha(\omega)|\hat{\nabla}_R\psi_j(r,R)\beta(\omega)\rangle = \langle \alpha(\omega)|\beta(\omega)\rangle \langle \psi_i(r,R)|\hat{\nabla}_R\psi_j(r,R)\rangle$$
$$\langle \alpha(\omega)|\beta(\omega)\rangle = 0$$

Intersystem crossing (ISC) then, is facilitated by a different kind of coupling known as spin-orbit coupling (SOC). SOC is a relativistic effect and not typically considered in quantum chemistry, which assumes that ISC is a spin-forbidden process. In reality, however, relativistic effects do come into play, especially in heavier atoms, and hence promote ISC. SOC is generally calculated perturbatively and a typical Hamiltonian, routinely used for the calculation of SOC, is the Breit-Pauli Hamiltonian [33,34]. When the SOC at a MECP is substantial, it essentially becomes a funnel to enable, the otherwise forbidden, ISC process.

2.2 Electronic Structure Methods

Solving the electronic structure of a molecule involves solving the $\hat{H}_{el}$, to get wavefunctions and energies of the molecule. However, $\hat{H}_{el}$ is exactly solvable only for hydrogen-like atoms (2 particle system), and requires approximate treatments for bigger systems. We start by discussing Hartree-Fock, a conceptually rich and elegant approximation, which generally forms the basis for more sophisticated approximations.

Hartree-Fock Approximation

Hartree-Fock (HF) starts by taking the form of the molecular wavefunction to be a Slater determinant, which is given below for a N electron molecule as,

$$\Psi = \frac{1}{\sqrt{N!}} \begin{vmatrix} \chi_1(1) & \chi_2(1) & \cdots & \chi_n(1) \\ \chi_1(2) & \chi_2(2) & \cdots & \chi_n(2) \\ \vdots & \vdots & \ddots & \vdots \\ \chi_1(N) & \chi_2(N) & \cdots & \chi_n(N) \end{vmatrix} \tag{2.6}$$

where, $(N!)^{-1/2}$ is a normalization factor and χ_a is a one electron wavefunction, or spin orbital, written as a linear combination of atomic orbitals, ϕ_n.

$$\chi_a = \sum_n c_n \phi_n \tag{2.7}$$

The variational principle is then used to obtain the Slater determinant (wavefunction) with the lowest possible energy, i.e., $E_0 = \langle \Psi_0 | \hat{H} | \Psi_0 \rangle$ is minimized by varying the coefficients c_n. This minimization leads to the HF equation,

$$f(i)\chi_a(i) = \epsilon_a \chi_a(i)$$

where, $f(i)$ is a one-electron operator, called the Fock operator and is given by

$$f(i) = -\frac{\hbar^2}{2m_e}\nabla_i^2 - \sum_{A=1}^{M} \frac{1}{4\pi\epsilon_0}\frac{Z_A e^2}{r_{iA}} + \nu^{HF}(i) \tag{2.8}$$

where, r_{iA} is the distance between the ith electron and the Ath nucleus, and M is the number of nuclei. The essence of HF is in the $\nu^{HF}(i)$ term, which is the average potential experienced by the ith electron due to all the other electrons, and is called the HF potential. Therefore, within the HF approximation, a many-electron problem has

been reduced to a one-electron problem.

The set of n spin orbitals, $\{\chi_a\}$, and respective orbital energies, ϵ_a, are obtained when we solve for the eigenfunctions of the HF operator. However, information of the spin orbitals is required for the estimation of $\nu^{HF}(i)$. In effect the HF operator depends on its eigenfunctions. Therefore, the HF equations need to be solved iteratively, and this is done by starting with a set of 'guess' spin orbitals and calculating $\nu^{HF}(i)$, the eigenfunctions of which will yield a new set of spin orbitals. This process is repeated till the average field, $\nu^{HF}(i)$, converges i.e., the spin orbitals which are used to construct $\nu^{HF}(i)$, also happen to be its eigenfunctions.

The elegance of HF is that the wavefunction is maintained as a product of orbitals throughout. Therefore, the shapes and energies of the orbitals which emerge from HF have an underlying physical interpretation, and can be used to explain experimentally observed phenomena.

Static and Dynamic Correlation

Correlation energy, by definition, is the difference between the HF energy (assumed to be calculated with a complete basis) and the exact nonrelativistic energy, i.e., it is all the electronic energy contribution that HF cannot capture. All attempts to develop better electronic structure methods, therefore, aim to account for as much of the correlation energy as possible.

$$E_{corr} = E_{exact} - E_{HF}$$

The correlation energy is further divided into two components – static and dynamic (sometimes called dynamical) correlation, but the decomposition of the correlation energy into these two components is not delineated clearly. Nevertheless, here we attempt to understand the electronic contributions of static and dynamic correlation, and the

methods than can be used to describe them.

In HF, an electron does not respond to all the other electrons instantaneously, but instead interacts with the average field generated by all the other electrons taken together. In reality however, an electron does respond to each of the other electrons in the system, and not just the average field. This is the dynamic correlation component and is called so because it originates due to the motion of the other electrons. Strictly speaking, HF does account for some part of the energy which arises from the motion of electrons, since two electrons of the same spin are not allowed to occupy the same orbital. However, nothing restricts two electrons of the opposite spin to come very close to each other within the HF formalism.

Clearly, dynamic correlation plays a role when two electrons are close, and the motion of one affects the other. This implies that when a bond gets stretched, and the electrons move apart from each other, the correlation energy should decrease. However, this was not found to be the case, and in fact, for stretched geometries, there is an increase in the correlation energy and HF does quite badly. This is because within HF, the wavefunction is described by a single Slater determinant. However, at stretched geometries, two configurations become nearly degenerate and both these configurations are required for the correct description of the wavefunction. This is the 'static' component of the correlation energy, also called 'non-dynamic', since it does not involve the motion of electrons. Static correlation is an important consideration while studying excited states as geometries in the excited states tend to be 'floppier' compared to ground states structures, with stretched bonds and loose angles. In the following subsections, we discuss methods, broadly called post-HF methods, that account for static and dynamic correlation, and the manner in which they are able to do better than HF.

Configuration Interaction

To account for static correlation, several determinants need to be included in the wavefunction, and a conceptually simple way to do this is achieved in Configuration Interaction. Here, determinants are generated by replacing occupied spin orbitals in the HF Slater determinant with unoccupied orbitals, and is given as,

$$\Psi = C_0\Psi_0 + \sum_s C_s\Psi_s + \sum_d C_d\Psi_d + \sum_t C_t\Psi_t \ldots \tag{2.9}$$

where, Ψ_0 is the HF Slater determinant, and Ψ_s, Ψ_d and Ψ_t correspond to all possible single, double and triple excitations in Ψ_0. Further, linear combinations of these determinants are taken to ensure that they are eigenfunctions of the $\hat{S}^2$ operator. Such spin-adapted determinants are called Configuration State Functions (CSF).

In view of computational costs, the excitations are generally limited to single and double excitations. Full configuration interaction or FCI is when all possible excitations are considered. While computationally it is only feasible for small systems, it guarantees very accurate results.

Complete-Active Space Self-Consistent Field (CASSCF) method

Although configuration interaction includes several CSFs in its wavefunction, it is constrained by the HF Slater determinant. While the coefficients, C_n in Eq. 2.9, are flexible, the spin orbitals contained within the CSFs themselves remain as they were following the HF optimization.

This deficiency is rectified in the Complete-Active Space Self-Consistent Field (CASSCF) method [35,36]. In CASSCF, the orbital space is divided into 3 types of orbitals labelled inactive, active and secondary orbitals, as shown in Figure 2.1. Intuitively, we understand that the inactive orbitals, being very close to the nucleus, are very low in energy to be involved in excitations at reasonable energies, while the secondary orbitals are too

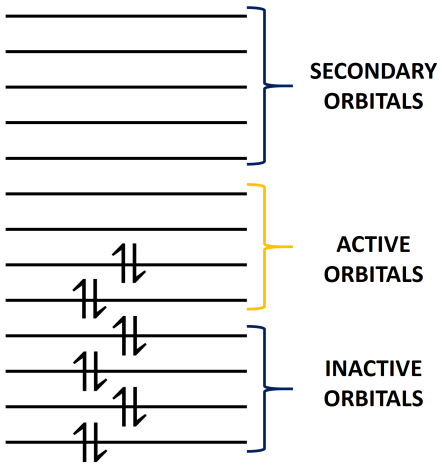

Figure 2.1: Schematic showing the division of the orbital space into inactive, active and secondary orbitals in CASSCF. In this figure the active space shown consists of 4 electrons in 4 orbitals.

high in energy. The wavefunction in CASSCF involves CSFs with all possible excitations within the active space – it can be thought of as FCI within the active space with the added flexibility that the orbitals themselves can also be varied. Thus, along with optimization of the coefficients which appear before the CSFs (C_n in Eq. 2.9), CASSCF also allows for the optimization of the coefficients which make up the spin orbitals inside the CSFs (c_n in Eq. 2.7). Therefore, the shapes of the CASSCF orbitals, which are qualitatively different from HF orbitals, capture excited state properties effectively. Their energies, however, are not as meaningful as HF orbital energies.

While it may seem prudent to include several electrons and orbitals in the active space, the computational cost scales very quickly. For an active space composed of n_e electrons in N_O spatial orbitals, the number of determinants for a state with total spin S is given by

$$D(N_O, n_e, S) = \binom{N_O}{n_e/2 + S}\binom{N_O}{n_e/2 - S}$$

of which, the number of CSFs is given by

$$CSF(N_O, n_e, S) = \frac{2S+1}{N_O+1}\binom{N_O+1}{n_e/2-S}\binom{N_O+1}{n_e/2+S+1}$$

The number of determinants and CSFs depend on the total spin, S, since the determinants and CSFs need to be spin-adapted, i.e., they need to be eigenfunctions of the spin operator, $\hat{S}^2$. Not all determinants will fulfil this criterion to begin with and their linear combinations need to be taken to make spin-adapted.

As an example: an active space of 14 electrons in 10 orbitals, which is one of the active spaces used in this study, would have 4950 and 6930 CSFs for a singlet and triplet state calculation, respectively. To manage computational costs, electrons and orbitals in the active space need to be chosen such that they best represent the process being studied. For instance, if a bond is being broken and another formed, then the σ and σ^* orbitals along these bonds need to be included. The processes studied in this thesis only include photophysical processes, and accordingly, orbitals that are likely to take part in excitations, such as π, π^* and high energy lone pairs, have been included in the active spaces used. Choosing orbitals in the active space is a balancing act between correct description of the wavefunction and computational cost.

Many-body perturbation theory

Second order Møller-Plesset perturbation theory, or MP2, is a perturbative way to recover some dynamic correlation from HF [37]. The MP2 wavefunction is built up of the HF Slater determinant along with some single, double, triple and quadruple excitations from the HF state. This accounts for dynamic correlation, by providing some virtual orbitals for the electrons to occupy and hence 'respond' to the instantaneous coulombic repulsion from other electrons – the dynamic correlation. A perturbative treatment however, can only do as well as the reference it is built on, which for MP2 is the HF

Slater determinant. Therefore, in a system with strong static correlation, where HF does badly because of a single-configurational treatment, MP2 does not help significantly.

This is addressed in CASPT2, which is a second order perturbative treatment where a multi-configurational wavefunction – the CASSCF wavefunction, is used as a reference [38]. CASPT2 generates CSFs in the CASSCF wavefunction by switching orbitals between the inactive-active and the active-secondary spaces. Note that all active-active switches are already accounted for in the CASSCF wavefunction. CASPT2 therefore, accounts for both static and dynamic correlations.

CASPT2 calculations, do however, come with a high computational cost, since the number of CSFs are now more than those present in CASSCF. Therefore, for much of the calculations in this thesis, the geometries have been optimized using the CASSCF method, and CASPT2 (in two different variants of single-state CASPT2 [38] and multi-state CASPT2 [39, 40]) has been used to refine energies.

2.3 Nonradiative Transition Rates

Critical points like CIs and MECPs have been previously discussed which allow for a population transfer from one electronic state to another. The main difference between CIs and MECPs was also discussed and was found to be the presence of nonadiabatic coupling in the case of the former and SOC in the latter. Nonadiabatic coupling is typically a very strong coupling, especially close to a CI, meaning the coupling between the two states is significantly higher than the adiabatic energy difference between the two states. This is usually not true for SOC which is generally a weak coupling. In this section, Fermi's golden rule is discussed, which is a rate expression for nonradiative transition between two weakly coupled states.

Fermi's golden rule

Fermi's golden rule (FGR) is a rate expression, derived using time-dependent perturbation theory, and gives the transition rate between two weakly coupled states [31, 41]. The system at a certain time is assumed to have a particular set of eigenfunctions and eigenvalues which get perturbed when a weak perturbation is 'switched on' at $t = 0$ and then 'switched off' after some time $t = t'$. This perturbation can possibly induce a transition between the initial and final states and FGR quantifies the probability of this transition. The perturbation itself can be a constant or a time-dependent function.

FGR gives the nonradiative transition rate between a discrete initial state to a final continuum of states. In the case of molecules, where the states are considerably discrete, FGR is applicable when the adiabatic energy gap between the states is high. This will ensure that the vibrational states of the final state is high enough that it can be assumed to behave as a continuum.

The rate of transition between an initial and final state, k_{if}, is given as,

$$k_{if} = \frac{2\pi}{\hbar} \int |\langle \Psi_i | \hat{H}_{if} | \Psi_f \rangle|^2 \delta(E_i - E_f) dE_f \tag{2.10}$$

where, $\hat{H}_{if}$ is the Hamiltonian that describes the coupling between the initial and final states, and E_i and E_f are the energies of the initial and final states, respectively. The Dirac delta function ensures conservation of energy, by requiring the energy transfer to happen from the initial to the final state at the energy of the initial state. Following integration over the delta function, which is strictly speaking, a distribution and not a function, the following form of FGR is obtained,

$$k_{if} = \frac{2\pi}{\hbar} |\langle \Psi_i | \hat{H}_{if} | \Psi_f \rangle|^2 \rho_{E_f = E_i} \tag{2.11}$$

where, $\rho_{E_f=E_i}$ is the density of final states calculated at the energy of the initial state.

The coupling Hamiltonian, $\hat{H}_{if}$, is SOC in the case of ISC. FGR can also be used to calculate nonradiative transition rates between two electronic states of the same spin multiplicity (internal conversion) provided the states are weakly coupled. In this case, $\hat{H}_{if}$ will be nonadiabatic coupling, which needs to be converted to diabatic coupling with an appropriate diabatization scheme. This will be further elaborated in Section 6.2 of Chapter 6.

Chapter 3

Dependence of Absorption Spectra of Thiothymines on Position of Sulphur Substitution

In this Chapter, we explain the experimental trends observed in the absorption spectra of thiothymines [42]. Recently, Pollum et al. performed a comparative study of the absorption spectra and triplet yields of thiothymines [14]. As expected, they observed a redshift in the absorption due to sulphur substitution with respect to the parent

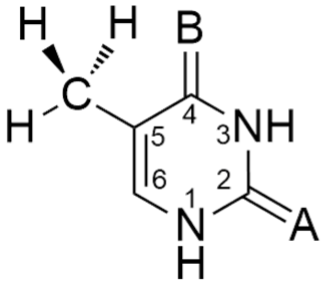

Thy, A = O, B = O
2tThy, A = S, B = O
4tThy, A = O, B = S
dtThy, A = S, B = S
2SeThy, A = Se, B = O
4SeThy, A = O, B = Se
dSeThy, A = Se, B = Se
2TeThy, A = Te, B = O
4TeThy, A = O, B = Te

Figure 3.1: Molecules studied in this chapter. The orientation of the hydrogen atoms of the methyl group at C^5 corresponds to the calculated most stable conformation.

molecule, thymine (Thy). Unexpectedly, however, they observed that thionation at the C^4 position of Thy led to a significantly greater red-shift than thionation at the C^2 position (Figure 3.1 shows atom numbering). This was also observed in uracil by the same authors, which only differs from Thy by the absence of a methyl group at C^5 [15]. This curious observation was explained by Bai and Barbatti who noted that in 2-thiothymine (2tThy) and 4-thiothymine (4tThy) the excitation took place to LUMOs with different electron density distributions [43]. In 2tThy, the electron density of the LUMO extends over the oxygen atom, whereas in 4tThy it extends over sulphur.[1] The greater redshift in 4tThy was attributed to the LUMO being along the weaker C=S bond as compared to the C=O bond in 2tThy. This brings up the puzzling question, "Why does the LUMO extend over oxygen or sulphur depending on the site of sulphur substitution?" The answer, besides being of fundamental interest, can help predict the absorption properties of other sulphur- and selenium- substituted thymine or uracil analogues. Moreover, knowledge of the nature of the LUMO can rationalize certain chemical properties such as electrophilic sites in the molecule [44].

In this Chapter, we seek to explain how and why the nature and energy of the LUMO and other frontier orbitals, which are responsible for the observed trends in absorption spectra, vary across sulphur-substituted thymines. Our hypothesis invokes an intriguing interplay of two types of electronic delocalization, which can either compete with or reinforce each other within a molecule. The hypothesis is tested on selenium-substituted thymines. A striking prediction is made about the nature of the LUMO in 2-selenothymine (2SeThy), which is validated by electronic structure calculations. Similar results are obtained for tellurium-substituted thymines. Our investigation is based on calculating accurate vertical excitation energies, assigning these transitions to molecular orbitals, examining the nature of these orbitals, and using a simple particle-

[1] There appears to be a typographical error in Reference [43] on page 6345 where it says, "The electron density in the 1' orbital of 2tThy extends to the sulphur atom, whereas the density in 1' of 4tThy extends over the oxygen." The description of the 1' orbital is correct when sulphur and oxygen are interchanged in this phrase.

in-a-box (PIB) model to obtain trends in these orbital energies based on their extent of delocalization. To ascertain the effect of cyclic delocalization, which might appear significant in Thy, and which has not been considered in our PIB model, we have studied model aliphatic systems based on Thy where this effect can be scrutinized.

3.1 Computational Methodology

All vertical excitation energy calculations were performed at the MS-CASPT2 [39, 40] (level shift of 0.3) [45] and EOM-CCSD [46] level of theory with the cc-pVTZ [47–50] (cc-pVTZ-PP [51] for Te) basis set. In order to include at least two bright states for all molecules, the state-averaged complete active space self-consistent field (SA-CASSCF) reference wave function used for MS-CASPT2 was composed of the lowest six singlet states. The active space consisted of 14 electrons in 10 orbitals and is shown for dtThy in Figure 2. Ground state structures were optimized at the Møller–Plesset second-order perturbation (MP2) level of theory [37] with the cc-pVDZ (cc-pVDZ-PP for Te) basis set, and frequency calculations were performed to confirm that these were true minima. All calculations were performed using the Molpro 2012 [52, 53] suite of quantum chemistry programs, and Molden [54] was used to visualize molecular orbitals.

3.2 Hypothesis for the Nature of the LUMO

The optimized ground state structures of all the molecules studied (Figure 1) were found to have C_s symmetry, although no symmetry was explicitly imposed. Our calculations show that of the 3 hydrogen atoms of the methyl group at C^5, the one that is in the plane of the molecule points away from the oxygen (or sulphur, selenium) atom at C^4 (Figure 1). An earlier calculation of another minimum energy structure for Thy, where the planar hydrogen atom of the methyl group points toward the oxygen [55], is in fact a first-order saddle point in light of our frequency calculations. The energy profile along

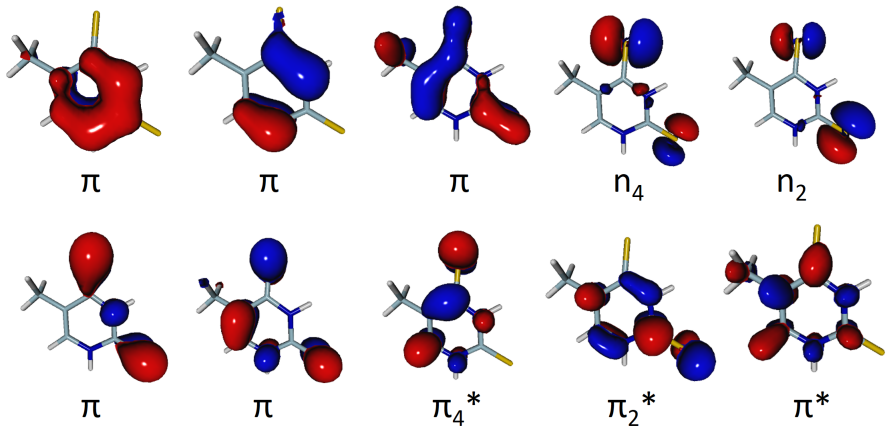

Figure 3.2: Active space of 14 electrons in 10 orbitals used in this study, shown for 2,4-dithiothymine, calculated at the SA-CASSCF (cc-pVTZ) level of theory with a state-averaging of 6 singlet states.

the rotation of the methyl single bond explains the nature of the imaginary frequency mode (Figure 3.3a). The higher barrier in the case of 2,4-dithiothymine (dtThy), along with consideration of van der Waals radii (Figure 3.3b), suggests that sterics play a governing role in determining the conformation of the methyl group in the minimum energy geometry of the ground state.

The vertical excitation energies and the orbital nature of the excitations of the lowest excited states of Thy at the MS-CASPT2 level are presented in Table 3.1, along with the energies of the corresponding states at the EOM-CCSD level. There is good agreement in energy values between the two electronic structure methods, and these energies concur with previous theoretical studies [43,55,60,61]. While vertical excitation energies cannot be directly compared to experimentally measured electronic excitation spectra, they are consistent with the measured peak maxima [57]. Oscillator strengths are nearly zero for the $n\pi^*$ states, while they are significant for the $\pi\pi^*$ states suggesting that the latter are the optically bright states. The two distinct bands in the longest wavelength region of the absorption spectrum of Thy can be assigned to the first two $\pi\pi^*$ states. Likewise, results for the different sulphur (Table 3.1) and selenium-substituted (Table 3.2) thymines using

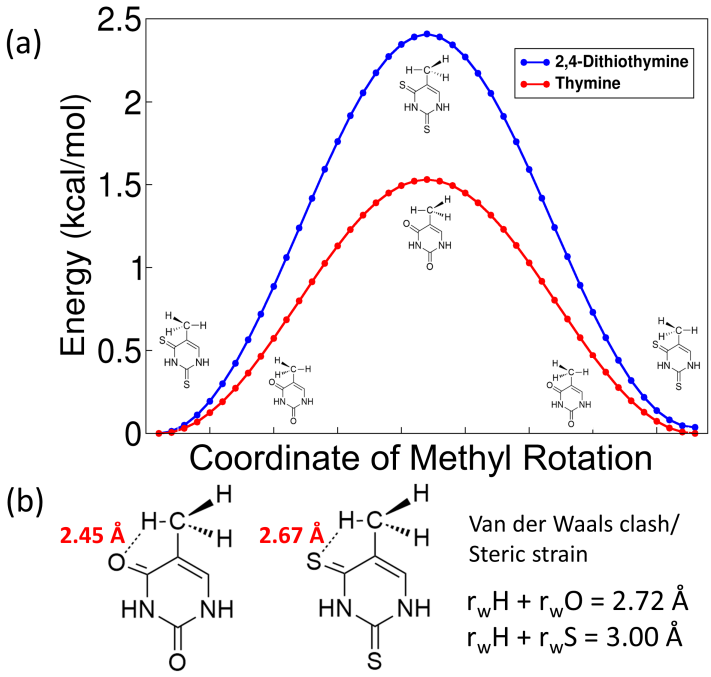

Figure 3.3: (a) Linear interpolation in internal coordinates plots showing energy barrier along rotation of the methyl group for thymine (red) and 2,4-dithiothymine (blue). (b) The distance between hydrogen and oxygen/sulphur in the less stable conformer is shown in red along with the sum of the van der Waals radii, r_w (taken from Ref [56]) indicating steric strain.

MS-CASPT2 and EOM-CCSD are presented, and the vertical energies of the optically bright states are found to be consistent with the experimental peak maxima. For all molecules, the lowest $\pi\pi^*$ state is of primary interest in the current study. The orbitals involved in the two lowest bright states, optimized at the SA-CASSCF level are shown in Figure 3.4. CASSCF orbitals do not have meaningful energies. Therefore, to analyze their energy trends, they are tallied with the corresponding canonical HartreeFock (HF) orbitals which are qualitatively similar and have well-defined orbital energies.

There are a few noteworthy observations one can make by focusing on the nature and energies of orbitals of Thy and the three thiothymines. These observations are schematically shown in Figure 3.5. (1) In Thy and all the thiothymines, the natures of the LUMO and LUMO+1 are consistently π_4^* and π_2^*, respectively. Here, π_4^* (π_2^*)

Table 3.1: Vertical excitation energies in eV (oscillator strengths in parenthesis) of thymine and thiothymines. Calculated at the MS-CASPT2 and EOM-CCSD levels of theory, on MP2 optimized ground state geometries, along with experimental values.

	Thy		Expt[a]		2tThy		Expt[b]
State	MS-CASPT2	EOM-CCSD		State	MS-CASPT2	EOM-CCSD	
$^1n_4\pi_4^*$	5.32 (0.00)	5.20 (0.00)		$^1n_2\pi_2^*$	4.26 (0.00)	4.13 (0.00)	
$^1\pi_c\pi_4^*$	5.82 (0.18)	5.53 (0.22)	4.95	$^1n_4\pi_4^*$	5.00 (0.00)	5.12 (0.00)	
$^1n_2\pi_2^*$	6.69 (0.00)	6.63 (0.00)		$^1\pi_c\pi_4^*$	5.22 (0.18)	4.81 (0.43)	4.13
$^1\pi_4\pi_4^*$	6.72 (0.16)	6.83 (0.06)	6.20	$^1\pi_c\pi_2^*$	5.32 (0.58)	5.21 (0.11)	4.49
$^1n_2\pi_4^*$	7.50 (0.00)	7.70 (0.00)		$^1n_2\pi_4^*$	5.80 (0.00)	5.94 (0.00)	
	4tThy		Expt[c]		dtThy		Expt[d]
State	MS-CASPT2	EOM-CCSD		State	MS-CASPT2	EOM-CCSD	
$^1n_4\pi_4^*$	3.20 (0.00)	3.15 (0.00)		$^1n_4\pi_4^*$	3.18 (0.00)	3.12 (0.00)	
$^1\pi_c\pi_4^*$	4.49 (0.40)	4.41 (0.43)	3.68	$^1n_2\pi_2^*$	4.14 (0.00)	4.05 (0.00)	
$^1\pi_4\pi_4^*$	5.19 (0.20)	5.18 (0.01)	4.58	$^1\pi_c\pi_4^*$	4.15 (0.01)	4.23 (0.23)	3.42
$^1n_4\pi_2^*$	6.00 (0.00)	6.15 (0.00)		$^1n_2\pi_4^*$	4.45 (0.00)	5.03 (0.00)	
$^1\pi_c\pi_2^*$	6.27 (0.13)	6.09 (0.07)		$^1\pi_4\pi_4^*$	4.65 (0.63)	4.54 (0.30)	4.38

Experimental values taken from [a]Ref [57], [b]Ref [58], [c]Ref [59] and [d]Ref [14].

Table 3.2: Vertical excitation energies in eV (oscillator strengths in parenthesis) of thymine and thiothymines. Calculated at the MS-CASPT2 and EOM-CCSD levels of theory, on MP2 optimized ground state geometries, along with experimental values.

2SeThy			4SeThy			dSeThy	
State	MS-CASPT2	Expt[a]	State	MS-CASPT2	Expt[b]	State	MS-CASPT2
$^1n_2\pi_2^*$	3.74 (0.00)		$^1n_4\pi_4^*$	2.69 (0.00)		$^1n_4\pi_4^*$	2.69 (0.00)
$^1\pi_c\pi_2^*$	4.48 (0.50)	4.04	$^1\pi_c\pi_4^*$	3.97 (0.44)	3.36	$^1n_2\pi_2^*$	3.62 (0.00)
$^1\pi_c\pi_4^*$	4.90 (0.23)		$^1\pi_4\pi_4^*$	4.94 (0.22)		$^1\pi_c\pi_4^*$	3.62 (0.02)
$^1n_2\pi_4^*$	5.21 (0.00)		$^1n_4\pi_2^*$	5.53 (0.00)		$^1n_2\pi_4^*$	3.85 (0.00)
$^1\pi_2\pi_2^*$	5.86 (0.02)		$^1\pi_c\pi_2^*$	5.85 (0.07)		$^1\pi_4\pi_4^*$	3.98 (0.73)

Experimental values taken from [a]Ref [62] and [b]Ref [63]. Experimental data not available fro dSeThy.

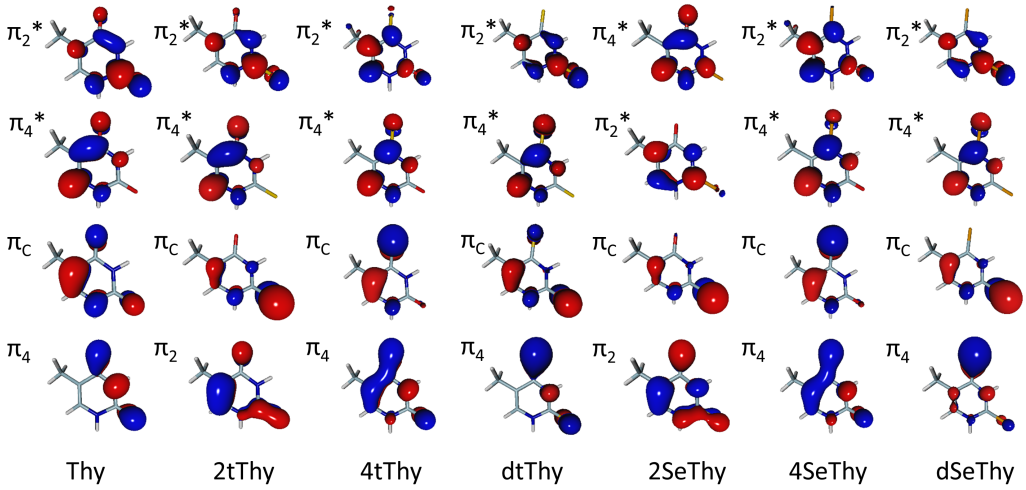

Figure 3.4: Orbitals characterizing the electronic transitions to the lowest two bright states for all molecules studied, optimized at the SA-CASSCF level at the MP2 optimized geometry. Subscript '2' denotes location of the orbital primarily on the C^2=X bond, '4' on the C^4=X bond (X=O, S, and Se), and 'C' on the C^5=C^6 bond.

denotes a π^* orbital located along the C^4=X (C^2=X) bond where X can be O or S. (2) In Thy and two of the thiothymines (4tThy and dtThy), the two lowest bright states are both characterized by transitions to the LUMO. In 2tThy, on the other hand, the two lowest bright states are characterized by excitations to the LUMO and LUMO+1; both transitions originate from the same occupied orbital. (3) The energy gap between the π_4^* and π_2^* orbitals (ΔE_L), shows a remarkable modulation on single sulphur substitution at two different sites: for canonical Thy, ΔE_L is 2.1 eV. In 2tThy, ΔE_L decreases to 0.7 eV, while in 4tThy, it increases to 2.5 eV.

Consider point (1). In 2tThy, the π_4^* orbital, which extends along C^4=O, being the LUMO is unanticipated. A C=S bond is longer and weaker than a C=O bond, and the molecular orbitals in C=S are more delocalised than in C=O. The bonding π orbital in C=S is destabilized and antibonding π^* orbital stabilized with respect to the stronger C=O bond. Thus, the π_2/π_2^* orbitals (which extend along C^2=S) is expected to be the HOMO/LUMO. Moreover, although the observation in point (2) and the trends in ΔE_L

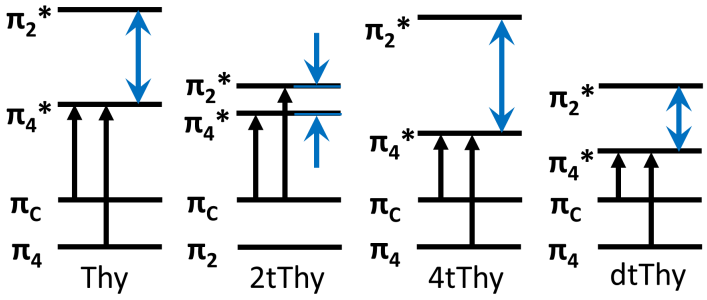

Figure 3.5: Transitions characterizing the first two bright states (black arrows) and the relative magnitude of ΔE_L (blue double-arrows) in Thy and the thiothymines.

in point (3) might seem justifiable based on the stabilization of a C=S π^* orbital with respect to a C=O π^* orbital, the very different magnitudes of the changes in ΔE_L for 2tThy and 4tThy with respect to Thy points to a more involved phenomenon.

All the above observations can be explained by hypothesizing an interplay between two types of delocalization: one due the conjugated C^4=X and C^6=C^5 bonds which is intrinsic to the molecular skeleton of the thymine molecule; two, attributable to the greater size of the atom substituted (X) at either the C^2 or the C^4 position (i.e., the larger the atom substituted, the greater the delocalization). Clearly, when X is the same, the π and π^* orbitals on C^4=X are more delocalised than the orbitals on C^2=X. The two types of delocalization compete with each other in the LUMO and LUMO+1 of 2tThy where the π_4^* (on C^4=O) is stabilized by conjugation while the π_2^* (on C^2=S) is stabilized by size-driven delocalization. Conjugation dominates due to which π_4^* is the LUMO, but the LUMO+1 (where there is size-driven delocalization) gets extremely close in energy to the LUMO. In 4tThy, on the other hand, these two effects enhance each other in the LUMO and are absent in the LUMO+1; the π_4^* (on C^4=S) has both conjugation and size-driven delocalization. This leads to a more delocalised LUMO that is drastically lowered in energy than the LUMO+1 (on C^2=O). In dtThy, the two effects neither compete nor enhance each other. The ΔE_L value (1.1 eV) is thus intermediate to that of 2tThy and 4tThy. The ΔE_L is lower than that of Thy because the presence

of two weaker C=S (compared to C=O) bonds causes an overall lowering and clustering of states and, consequently, a reduction in the gap.

3.3 PIB Model and Prediction for 2SeThy

We have used the PIB model to analyze the implications of our hypothesis. The model is used to estimate energy trends of the LUMO and LUMO+1 energies of Thy and substituted thymines. The PIB model is routinely used for the calculation of HOMO–LUMO energies in π conjugated systems. As described in introductory quantum chemistry textbooks [64–66], the π electrons are considered to be independent particles in a one-dimensional box whose length is estimated using the constituent bond lengths and an additional distance at the ends of the molecule. In this study, we have employed the PIB model in a different manner to compare the two types of delocalisation within the thymine molecule. Considering our hypothesis, we divide the thymine skeleton into two separate π systems: the 4-electron C^6=C^5–C^4=X system and the 2-electron C^2=X system (Figure 3.6). The various substituted thymines correspond to different combinations

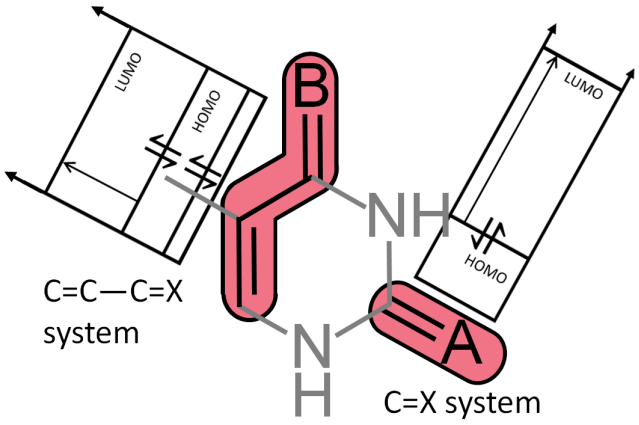

Figure 3.6: Thymine skeleton showing the two types of delocalization modeled by the particle-in-a-box.

of the two π systems where X=O, S, and Se. The calculation of the length of the box

for each case is shown in Figure 3.7. Two electrons are filled in each energy state or spatial orbital following the Pauli principle (Figure 3.6), and the energies of the HOMO and LUMO for each molecule are shown in Table 3.3 and graphed in Figure 3.8. The

Table 3.3: HOMO and LUMO energies for the C^2=X and C^4=C^5—C^6=X systems with different substitutions (X=O, S, Se, Te) from the PIB model.

	C^2=X		C^4=C^5—C^6=X	
X	HOMO (eV)	LUMO (eV)	HOMO (eV)	LUMO (eV)
O	5.48	21.91	5.06	11.40
S	3.18	12.71	3.81	8.58
Se	2.69	10.75	3.49	7.84
Te	2.18	8.73	3.11	7.00

energies of the HOMO are similar for the C^6=C^5–C^4=X and C^2=X systems, which are related to the energy of a state being directly proportional to the square of the quantum number ($n_{HOMO} = 2$ for the former and 1 for the latter) and inversely to the square of the box length (the former length is approximately two times the latter, see Figure 3.7). Furthermore, for different X in either C^6=C^5–C^4=X or C^2=X systems, the HOMO energies do not change significantly as compared to the LUMO energies (Figure 3.8). This is because the energy depends on the square of the quantum number, and n_{LUMO} is greater than n_{HOMO}. We therefore focus on the energies of the LUMOs to explain the observations about Thy and substituted thymines (Figure 3.9).

The sharper decrease in the energy of the LUMOs of the C^2=X system in comparison to the C^6=C^5–C^4=X system stands out in Figure 3.9. This can be understood by considering the energy expressions for the LUMOs of the C^2=X (Eq. 3.1) and C^6=C^5–C^4=X (Eq. 3.2) systems.

$$E_{LUMO}^{C=X} = c\frac{2^2}{l_{C=X}^2} \tag{3.1}$$

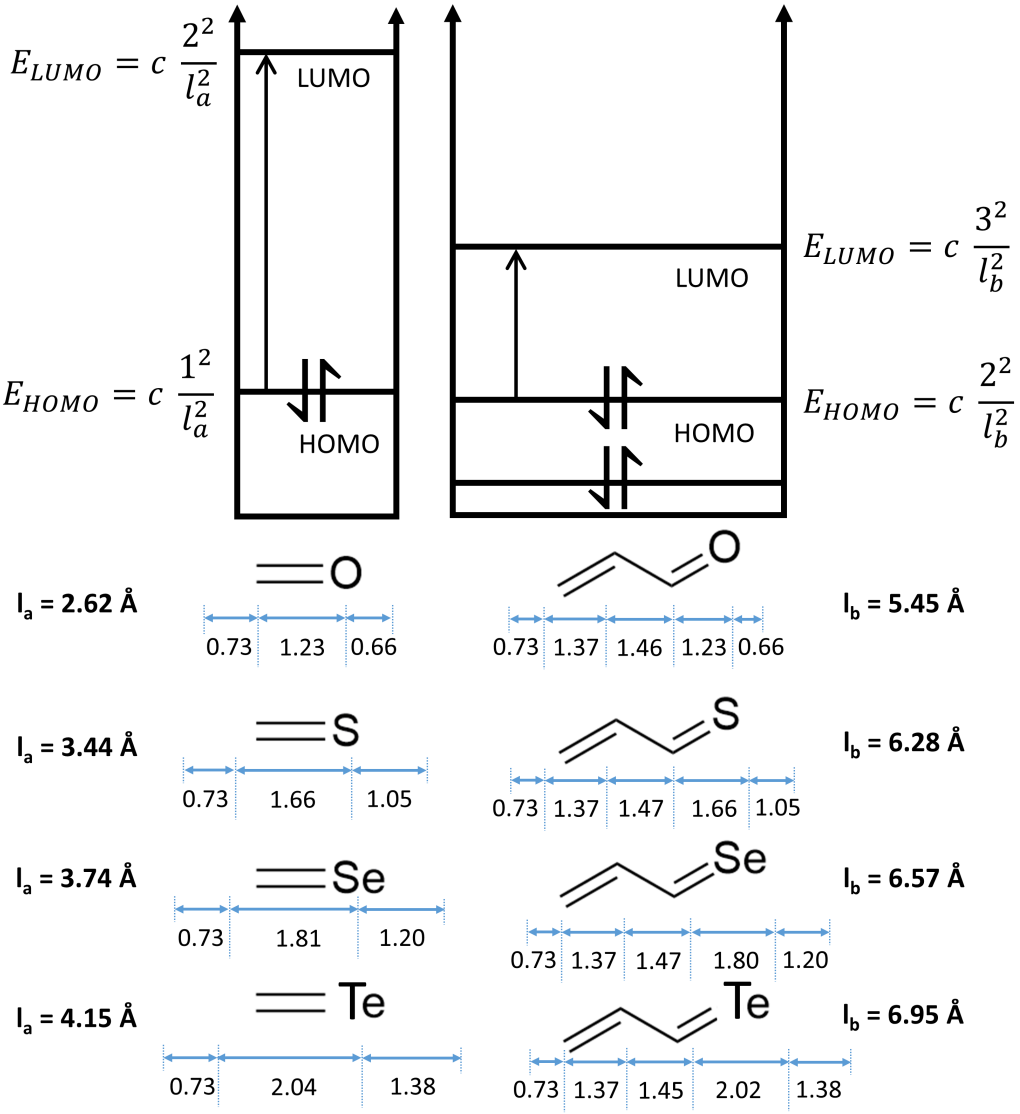

Figure 3.7: Particle-in-a-box models for the C^2=X and C^6=C^5–C^4=X (X = O, S, Se, Te) systems. The lengths and energy levels of the two boxes are to scale for the C^2=O and C^6=C^5–C^4=X systems. All bond lengths are given in Angstroms and taken from MP2/cc-pVDZ optimized calculations. The additional lengths at the ends of the molecule are covalent radii taken from Ref [67]. The energy states are filled according to Pauli's exclusion principle and the formulae to calculate HOMO and LUMO energies are given alongside. The constant c (37.606 eV) incorporates Planck's constant, mass of electron, a factor of 1/8 and conversion of joules to electron volts. The variables l_a and l_b represent the box length in Å of the C^2=X and C^6=C^5–C^4=X systems respectively.

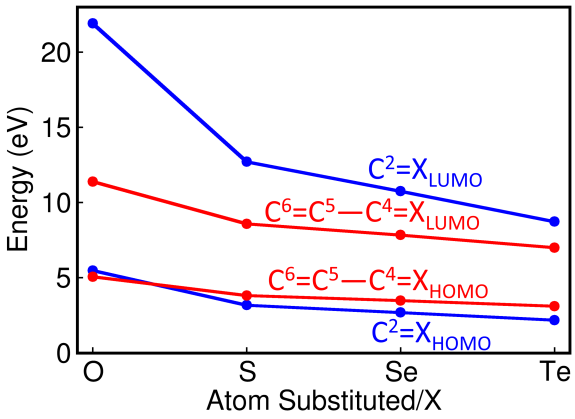

Figure 3.8: HOMO and LUMO energies (in eV) for the C=X (blue) and C=C–C=X (red) (X=O, S, Se, Te) systems

$$E_{LUMO}^{C=C-C=X} = c\frac{3^2}{l^2_{C=C-C=X}} \tag{3.2}$$

where c is a constant. When X = O, $l_{C=C-C=X} \approx 2l_{C=X}$, implying that $E_{LUMO}^{C=X} > E_{LUMO}^{C=C-C=X}$ (Figure 3.9). On the other hand, for large size of atom X, the C=X length is large, $l_{C=C-C=X} \approx l_{C=X}$, and consequently $E_{LUMO}^{C=X} < E_{LUMO}^{C=C-C=X}$. Since $E_{LUMO}^{C=X}$ LUMO crosses over $E_{LUMO}^{C=C-C=X}$ at large X, the former must fall faster than the latter as the size of X increases.

The different redshifts and unusual modulation of ΔE_L for singly substituted thymines can be understood based on the overall trend in the LUMO energies. For example, 2tThy has the components C^6=C^5–C^4=O and C^2=S. As seen from Figure 3.9, the energy of the LUMO of decreases significantly compared to that of C^2=O but still remains higher than the LUMO of C^6=C^5–C^4=O. This suggests that the LUMO of 2tThy extends over C^6=C^5–C^4=O and the LUMO+1 over C^2=S. Notably, the ΔE_L in 2tThy (red pair of arrows near S) becomes much smaller compared to Thy (green double-headed arrow near O) because of the stabilization of the LUMO+1. In 4tThy, the LUMO corresponds to the LUMO of C^6=C^5–C^4=S and ΔE_L (brown double-headed arrow near S) is greater than Thy (green double-headed arrow near O). The different magnitudes of the changes

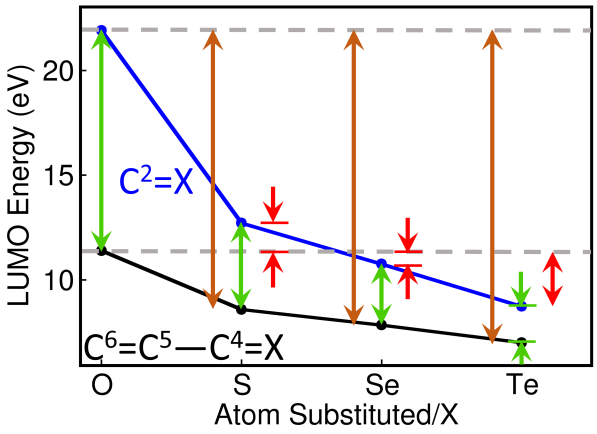

Figure 3.9: LUMO energies (in eV) as calculated from the PIB model for the two π systems for X = O, S, Se, and Te. The values of ΔE_L estimated from the model are represented by green double-headed arrows for disubstituted, brown double-headed arrows for 4-substituted, and red double-headed arrows for 2-substituted thymines. The gray dashed lines are the LUMO energies for X=O for the two systems.

in ΔE_L for 2tThy and 4tThy with respect to Thy are now clearly evident and originate in the effect of sulphur substitution being different in C^2=X versus C^6=C^5–C^4=X. In dtThy, since both the C^6=C^5–C^4=S and C^2=S systems are stabilized by thionation, ΔE_L (green double-headed arrow near S) is lower than in Thy (green double-headed arrow near O), and also intermediate of 4tThy and 2tThy.

For the selenothymine series, the model makes an unanticipated prediction. The LUMO energy of the C^2=Se system is lower than that of the C^6=C^5–C^4=O system (Figure 3.9), which suggests that the LUMO in 2SeThy extends over C^2=Se in contrast to all the other substituted thymines considered so far. This prediction is confirmed by ab initio calculations (Figure 3.4, top two rows) which indicate the flipping of the nature of the LUMO and LUMO+1 in the case of 2SeThy in contrast to the other six molecules. The magnitude of ΔE_L accompanying the crossover of orbital nature is predicted to be small (red pair of arrows near Se in Figure 3.9), and in line with this, the ΔE_L for 2SeThy, calculated from HF orbital energies, is -0.6 eV. The negative sign indicates that the π_2^* (along C^2=Se) has flipped to be lower in energy than the π_4^* (along C^6=C^5–

C^4=O). A similar observation is made for tellurium- substituted thymines (2TeThy and 4TeThy).

The LUMO energies calculated from the PIB model not only explain the modulation of ΔE_L but also successfully predict the origin of redshifts in the absorption spectra of these molecules. The underlying premise is that in the sulphur-substituted thymines, the energies of the LUMOs are most significant in determining redshifts [43]. From Figure 3.9, we see the "lowest energy LUMO" is predicted to extend over C^6=C^5–C^4=O for Thy and 2tThy and on C^6=C^5–C^4=S for 4tThy and dtThy. Incidentally, this persistent delocalization of the LUMO on the fourth position means that it is located on different atoms (O or S) depending on the site of substitution (2tThy or 4tThy, respectively). In previous work, the explanation of the different redshifts in 2tThy or 4tThy was based on the observation of the LUMO in these molecules being located on different atoms [43]. However, the reason for the LUMOs being this way, a question that is stated in the introduction, had not been investigated so far and can be precisely understood based on the hypothesis presented above.

3.4 Role of Cyclic Delocalization and Limitations of the Hypothesis

Thy and its sulphur- and selenium-substituted analogues have certain resonance structures which exhibit cyclic delocalization (Figure 3.10). To study the influence of this

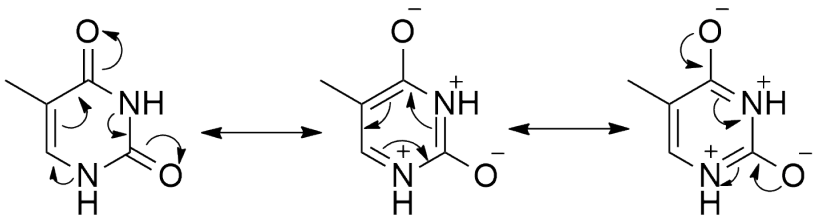

Figure 3.10: Resonance structures of thymine

type of cyclic delocalization on our hypothesis which is based on electron delocalization in two distinct π systems in the molecule, we have examined the molecular orbitals of an aliphatic model system obtained by breaking the N^3–C^4 bond of Thy, whereby the effect of cyclic delocalization is eliminated (Figure 3.11a). We see that in the model

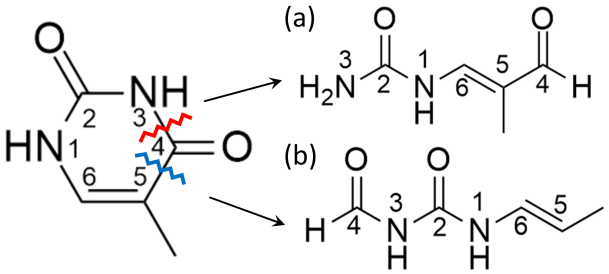

Figure 3.11: Aliphatic models constructed by breaking Thy between bonds (a) N^3–C^4 (red line) and (b) C^4–C^5 (blue line), respectively, to examine the role of cyclic delocalization.

molecule, like in Thy, the π^* orbital located on the fourth position continues to be the LUMO and is delocalised over C^6=C^5–C^4=O, while the π^* orbital located on the second position is higher in energy and extends primarily over C^2=O (Figure 3.12a). Thus, cyclic delocalization does not qualitatively affect the nature of the LUMO. However, if we consider another aliphatic model system obtained by breaking the C^4–C^5 bond of Thy (Figure 3.11b), where in addition to cyclic delocalization, conjugate delocalization is absent, we see the orbitals are significantly different from Thy (Figure 3.12b). Now the two lowest π^* orbitals are equally delocalised over both C=O bonds. On the basis of the two model systems, it is evident that the conjugated C^6=C^5–C^4=O unit plays a governing role in determining the nature of the LUMO of Thy, and cyclic delocalization is insignificant.

A limitation of our hypothesis is the underlying assumption that the 4-electron and 2-electron π systems in Thy do not interact at all. Because of this assumption, certain observations cannot be accounted for. For instance, the LUMO energy predicted from

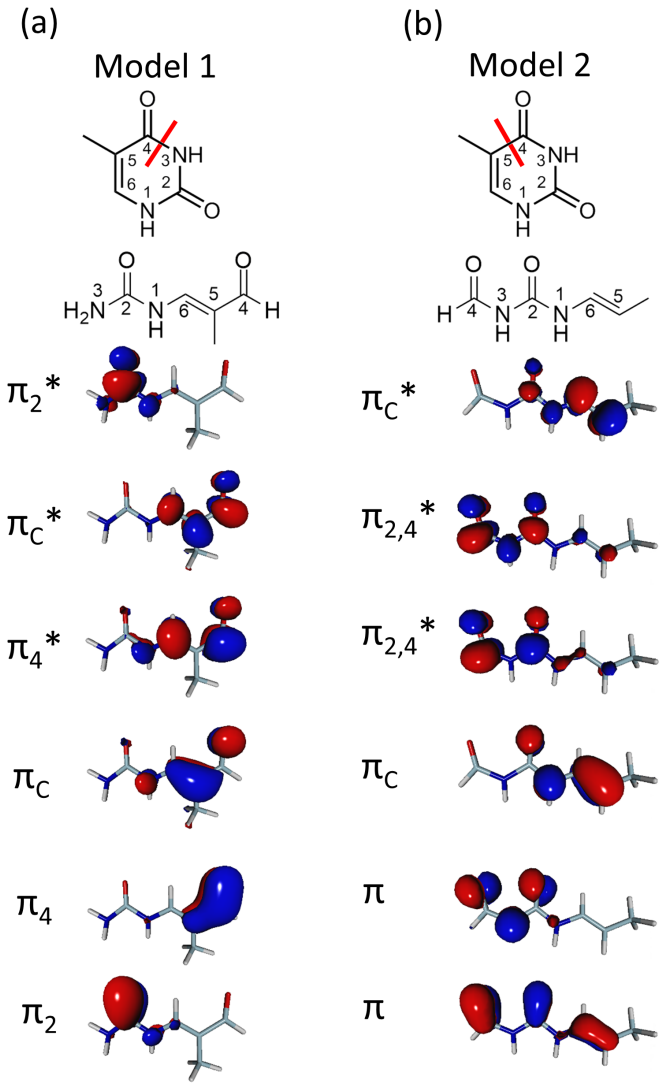

Figure 3.12: Aliphatic models constructed by breaking Thy between the bonds (a) N^3–C^4, which is denoted as Model 1 and (b) C^4–C^5 which is denoted as Model 2. The most relevant π and π^* orbitals optimized at the SA-CASSCF/cc-pVTZ level, composed of 5 singlet states at the MP2/cc-pVDZ optimized geometries of these models are shown.

Figure 3.9 for 2tThy is the same as that of Thy, which incorrectly implies that substitution at C^2 does not result in a redshift. Explaining this redshift would require taking into account an interaction between the two π systems. In that case, the presence of a C=S bond in the molecule, which is weaker than the C=O bond, will affect the C=C–C=O system and can be expected to lower the energy of all the states as compared to Thy. A reflection of this is the lowered energy of all the calculated excited states of 2tThy with respect to Thy (Table 3.1). In our study, however, the approach is kept deliberately simple by considering only the most influential factors, thereby allowing us to analyze the effect of substitution and obtain valuable physical insight.

3.5 Effect on Electrophilicity

The interplay between the two types of electronic delocalization has implications on the chemical properties of thymines as well. For instance, the LUMO of Thy (Figure 3.4) is delocalised along the C^6=C^5–C^4=O region and the largest coefficient of the LUMO is on C^6 followed by C^4 and none at all on C^2. This suggests that nucleophilic addition is most likely to happen on C^6 rather than on the carbonyl carbons, C^4 and C^2 [44], and this is confirmed experimentally [44, 68–70]. As an example, when thymidine reacts with N-bromosuccinamide and sodium azide, addition of the nucleophile (azide) takes place on C^6 [70]. This trend can be expected to persist in the sulphur-substituted thymines based on the strong similarity of their LUMOs with that of Thy (Figure 3.4). Interestingly, in 4tThy, where conjugation and size-driven delocalization assist each other, the LUMO energy is significantly lowered as compared to Thy and thus 4tThy can be expected to be a stronger electrophile as compared to Thy. In 2tThy, however, the LUMO energy does not change appreciably as compared to Thy but ΔE_L decreases dramatically, which suggests a possible competing electrophilic site, namely the C^2 carbon atom. In 2SeThy, based on the crossover of the LUMO to the C^2=Se region (Figure 3.4), nucleophilic

addition is predicted to take place at C^2 in this molecule. Additionally, considerations such as the hard–soft classification of electrophiles (which are affected by van der Waals radius and electronegativity among other aspects) and the groups next to the carbonyl group (for instance electron donating/withdrawing propensity) play a role. These factors may influence the site of nucleophilic attack and need to be kept in mind while predicting the site of nucleophilic addition.

3.6 Conclusions

A hypothesis providing a fundamental basis for explaining the unexpected trends in absorption spectra, and chemical properties like electrophilicity of different substituted thymine nucleobases is proposed. The different redshifts in the two singly substituted sulphur thymines as compared to Thy are explained by considering an interplay between two types of delocalization: One, due to the conjugation of the C^4=X (X = O, S) bond with the C^5=C^6 bond, which is intrinsic to the thymine skeleton. Two, due to the longer C=S bond compared to the C=O bond, which is because of the nature of substitution. While these factors compete with each other in 2tThy (with the first factor dominating), they augment each other in 4tThy. In both molecules, the LUMO is predicted to be located along the C^4=X bond, which happens to be along a C=O bond in 2tThy while along a C=S bond in 4tThy. The implications of the hypothesis are analyzed using a PIB model with variable lengths and electron occupations. The model explains the characteristic nature of the LUMO, as well as the unusual modulation in the energy gap between LUMO and LUMO+1 orbitals on sulphur substitution in Thy. Moreover, the model predicts an intriguing crossover in the nature of the LUMO in 2SeThy and 2TeThy where the size of the substituted atom, selenium/tellurium, is even larger than sulphur. In effect, a 2-center delocalization (C=Se/Te) can surpass a 4 center delocalization (C=C–C=O) in its influence on molecular properties. This is

verified using ab initio quantum chemical calculations. The PIB model can be applied to any molecule, where there are two or more distinct π systems, to predict the location of the LUMO. However, given the qualitative nature of the predictions, it is likely to be most useful for obtaining trends when there is a systematic change in size of one of the π systems while the others remain unchanged.

In general, this work provides a new framework to understand the variation in physical and chemical properties of molecules, obtained from atomic substitutions at different sites of a single parent molecule. It emphasizes the importance of atomic size, in addition to double-bond conjugation, in determining electronic delocalization in molecules.

Chapter 4

Dependence of Triplet Lifetimes of Thiothymines on Position of Sulphur Substitution

In the previous Chapter, we explained how the redshifts of the absorption maxima of thiothymines depend appreciably on the position of sulphur substitution [14, 42, 43]. After excitation, all three thiothymines undergo intersystem crossing (ISC) on an ultrafast timescale [14, 58, 59, 71–73] and the mechanism of ISC in these molecules has been extensively studied [9, 10, 74–78]. However, processes occurring after triplet formation, importantly decay phenomena which determine the triplet lifetime [58, 59], are not well understood.

An important implication of the triplet lifetime of thiothymines is the yield of reactive singlet oxygen produced by photosensitization of molecular oxygen in a cellular environment. Longer T_1 lifetime and greater T_1 yield of thiothymine generally translates to greater reactive oxygen yield [20]. Experimentally, while all thiothymines are found to have near unity T_1 yield, they do not have the same singlet oxygen yields [14, 58, 59].

In fact, the triplet lifetimes of 2- and 4-thiothymines correlate directly with the singlet oxygen yields (lifetime data of 2,4-dithiothymine (dtThy) not available). The lifetimes of 2-thiothymine (2tThy) and 4-thiothymine (4tThy) are estimated to be 2.7 μs and 4.2 μs in acetonitrile, and the corresponding singlet oxygen yields are 0.36 and 0.50 [58, 59]. The reason for the differing triplet lifetime depending on position of sulphur substitution motivates exploration of the triplet decay mechanism.

In the present Chapter, we investigate the fate of the different thiothymines after they are formed in the triplet state, and thereby explain trends in their triplet lifetimes. Given that thiothymines have negligible phosphorescence yields [73, 79–83], the lifetime can be expected to be controlled by the nonradiative decay dynamics from T_1 to the ground state. A comparison of geometries, barriers, and spin-orbit couplings (SOCs) associated with the decay channels in the different thiothymines has been made to understand the mechanism of triplet decay, especially how the mechanism varies across the molecules. The triplet decay dynamics of 4tThy and dtThy are found to be distinctly different compared to 2tThy, and this is explained based on their characteristic molecular structure. Building on this new understanding, substituted analogues of 2tThy have been proposed, which are expected to have increased T_1 lifetimes, therefore providing a strategy to make potentially better PDT drugs.

4.1 Computational Methodology

All excited minima and MECPs have been optimized using the state-averaged complete active space self-consistent field (SA-CASSCF) [35, 36] method, with a state-averaging comprising the lowest 2 singlet and lowest 3 triplet states and the 6-31G** basis set. Hessian calculations have been performed at the stationary points to ensure that they are true minima. An active space composed of 10 electrons in 7 orbitals has been used, which includes two lone pairs on the exocyclic oxygen or sulphur substituted at C^2

and C^4 (see Figure 3.1 for numbering), three highest energy π and two lowest energy π^* orbitals. Spin-orbit couplings (SOC) at the MECPs have been calculated using the Breit-Pauli Hamiltonian at the SA-CASSCF level of theory [34]. Linear interpolation in internal coordinate (LIIC) scans have been used to connect critical points on the potential energy surface (PES) and the energies have been calculated at the multi-state complete active-space second-order perturbation (MS-CASPT2) level of theory [39, 40]. A level shift [45] of 0.3 a.u. has been used in the MS-CASPT2 calculations to avoid non-convergence due to intruder states, along with the same active space and basis set as that used in the SA-CASSCF optimizations. All calculations have been performed using the Molpro 2012 [52, 53] quantum chemical suite of programs and orbitals have been visualized using Molden [54].

4.2 Effect of Position of Thionation on Triplet Decay Dynamics

The position of sulphur substitution is found to make a significant difference to the topology of the T_1 surface and consequently the triplet lifetime. Recent work on 2tThy has shown that its T_1 surface has two minima, one characterized by the sulphur atom going out of plane, i.e., pyramidalization of C^2 (T_1^{pyr}) and the other involving distortion of the ring (T_1^{ring}) [84]. The existence of two minima on the T_1 surface has also been shown for the closely related 2-thiouracil molecule both theoretically [85] and experimentally [86]. Our calculations give consistent results for this molecule and we find that the T_1^{pyr} energy is only 0.002 eV lower than T_1^{ring}. Assuming that the two other thiothymines, 4tThy and dtThy, would have similar topological features, we have found two minima on the T_1 PES of both these molecules by starting the geometry optimization from two distinct points: one, the Franck-Condon (FC) structure, and two, a structure in which C^2 is pyramidalized by 30°and the C^2=X (X=O, S) bond is stretched by 0.2 Å with

respect to the FC structure. These two minima were also optimized in the case of the canonical nucleobase, Thy.

In all molecules, the two triplet minima have consistently different electronic character. The T_1^{pyr} is characterized by an electronic transition to the π^* orbital localized over the C^2=X (X=O, S) bond, while the T_1^{ring} is characterized by a transition to the π^* orbital localized over the X=C^4–C^5=C^6 (X=O, S) atoms (Figure 4.1 and Figure 4.2). These two orbitals are referred to as π_2^* and π_4^* for brevity. The two T_1 minima can be

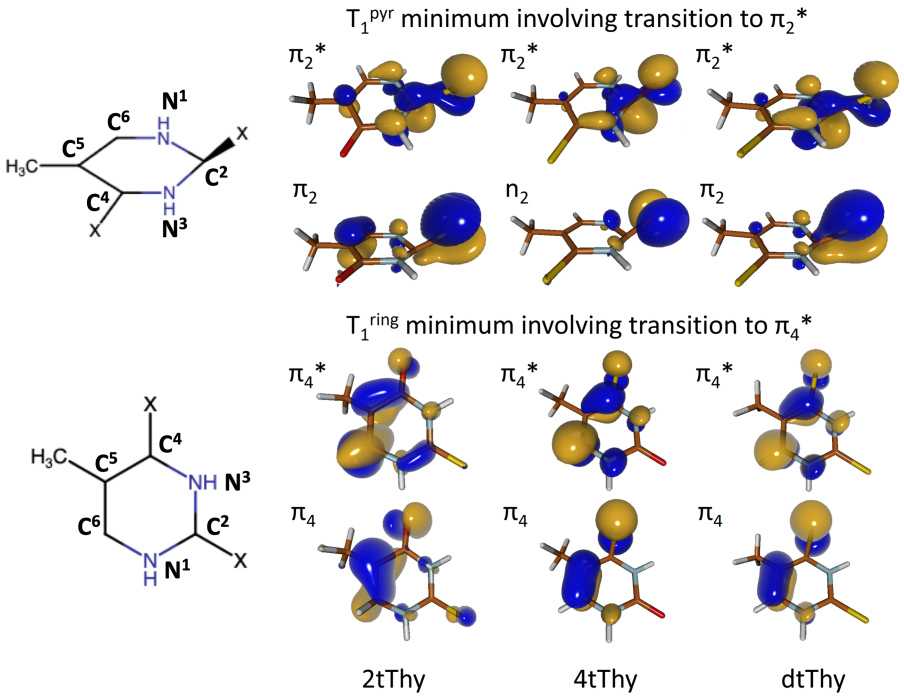

Figure 4.1: Molecular geometries of the two minima on the T_1 PES of all three thiothymines along with the orbitals involved in the T_1 transition. The minimum with strong pyramidalization at C^2=X (X=O, S) is characterized by a transition to the π_2^* orbital, while the nearly planar structure is characterized by a transition to the π_4^* orbital.

thought to be associated with two diabatic surfaces, which are coupled to give the adiabatic T_1 surface of mixed electronic character (Figure 4.3). The geometries of the two minima in all molecules follow trends that are consistent with their electronic nature. At T_1^{pyr}, the principal geometric variation with respect to the ground state is the elongation

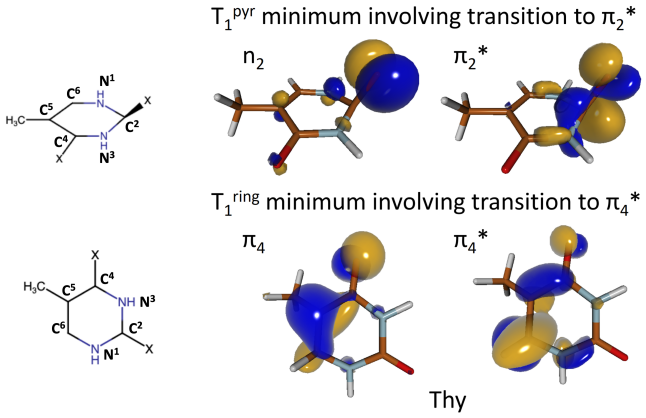

Figure 4.2: Molecular geometries of the two minima on the T_1 PES of Thy along with the orbitals involved in the T_1 transition.

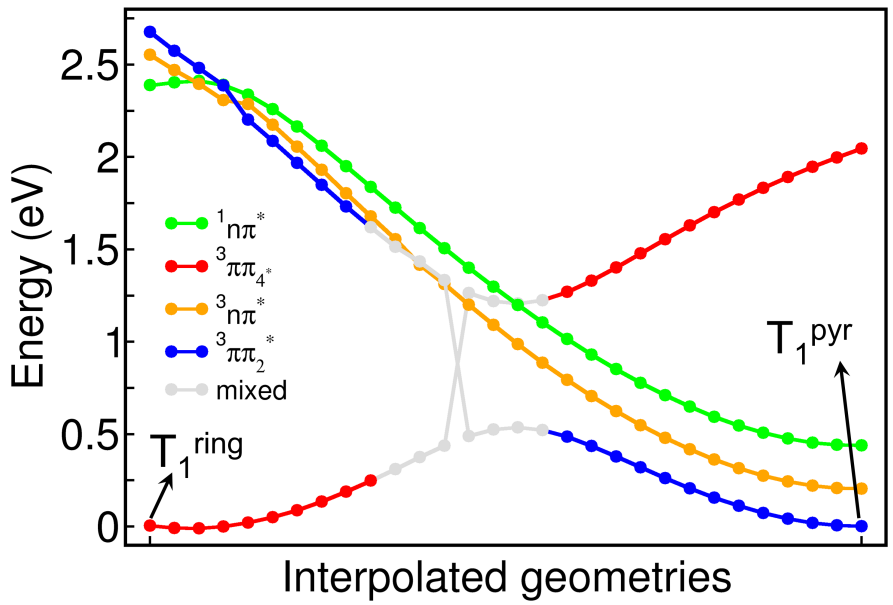

Figure 4.3: LIIC scan between the T_1^{ring} and T_1^{pyr} minima in 2tThy at the MS-CASPT2 level of theory, showing the diabatic natures of states. The state natures have been identified by examining the orbitals and cross-referencing them with the CI vector coefficients.

of the C^2=X (X=O, S) bond by about 0.2 Å and out of plane displacement of the X atom by about 50°(Table 4.1). For T_1^{ring} however, the principal geometric variation with respect to the ground state is the elongation of the C^5=C^6 bond by about 0.1 Å.

Table 4.1: Some geometrical parameters for thymine and the thiothymines at their Franck-Condon structure and T_1 minima.

Molecule	Geometry	C^2=X (Å)	$\delta(N^1C^2N^3X)$	C^5=C^6 (Å)
2tThy	Franck-Condon[a]	1.64	180°	1.35
	T_1^{pyr}	**1.82**[b]	**230°**	1.35
	T_1^{ring}	1.64	180°	**1.49**
4tThy	Franck-Condon	1.20	180°	1.35
	T_1^{pyr}	**1.39**	**230°**	1.33
	T_1^{ring}	1.20	180°	**1.43**
dtThy	Franck-Condon	1.66	180°	1.33
	T_1^{pyr}	**1.81**	**229°**	1.34
	T_1^{ring}	1.68	180°	**1.43**
Thy	Franck-Condon	1.20	180°	1.36
	T_1^{pyr}	**1.39**	**231°**	1.35
	T_1^{ring}	1.20	179°	**1.49**

[a]Franck-Condon geometries have been optimized at the SA-CASSCF level so that the geometrical parameters can be better compared with the values of the excited minima. [b]Values in bold are those that change significantly with respect to the Franck-Condon geometry.

The similarity of the T_1 surface across the molecules is striking, yet there is a very significant difference. The relative energy of the two T_1 minima is very different and this has consequences on the triplet decay dynamics. While these minima are almost equal in energy in 2tThy, T_1^{ring} is more stable than T_1^{pyr} by 2.3 eV in 4tThy and 0.7 eV in dtThy (LIIC scans connecting the two minima are shown in Figure 4.4). The relative energies of the T_1 minima are modulated in such a manner that there is an effective double well only in 2tThy, and not in the case of 4tThy and dtThy. In the case of 4tThy and dtThy, despite the presence of two minima, only the lower one, T_1^{ring}, can be expected to be relevant for the T_1 decay dynamics.

Two distinct MECPs were obtained for each molecule by starting the geometry optimization from the two T_1 minima. Like the triplet minima, these MECPs have the same

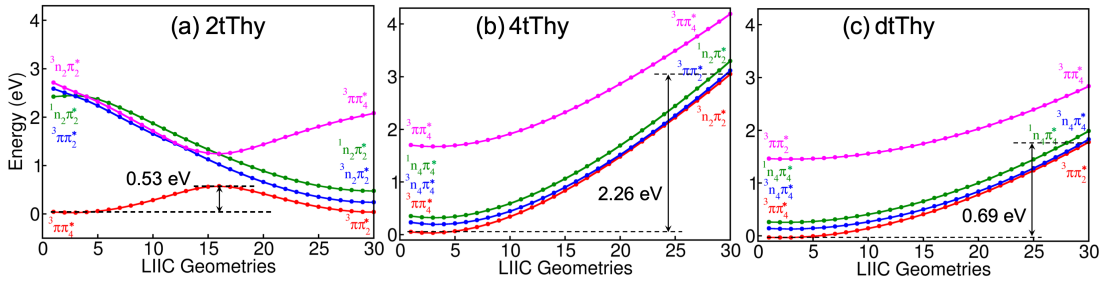

Figure 4.4: LIIC scans connecting the two minima on the T_1 PES of the thiothymines – 2tThy, 4tThy and dtThy.

overall geometrical features in all three molecules (Figure 4.5). The MECP connecting

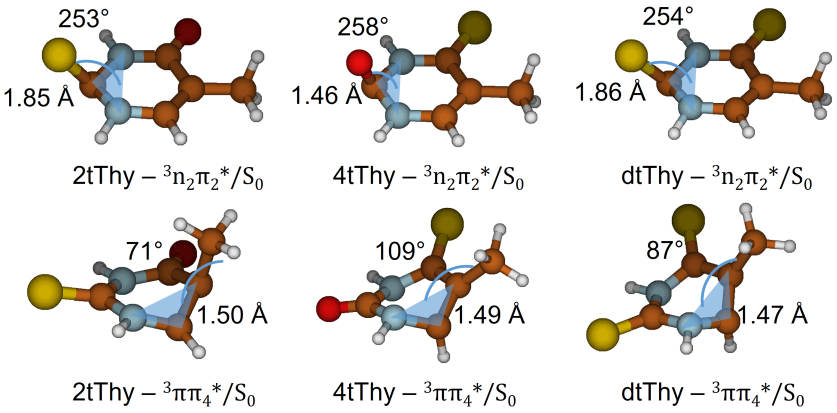

Figure 4.5: Two types of MECPs in the thiothymines: the MECP which is close to the T_1^{pyr} minimum (top) and the MECP which is close to the T_1^{ring} minimum (bottom).

the T_1^{ring} minimum with the ground state is a highly distorted structure, and deviates from the T_1^{ring} minimum by a pyramidalization of the methyl group for all three thiothymines (Figure 4.5). The geometry of the MECP connecting T_1^{pyr} to the ground state is similar to the T_1^{pyr} minimum itself. The T_1 deactivation channels of each molecule were then obtained by finding the path connecting the energetically relevant T_1 minima to the respective MECPs with the S_0 PES.

After electronic excitation, each molecule can be expected to relax to the S1 state

according to Kasha's rule and then undergo ISC to the triplet manifold. In 2tThy, as discussed above, both minima of T_1 are energetically accessible. However, the decay from T_1 to the ground state is likely to happen primarily through the MECP close to T_1^{pyr} because of its high SOC of 105 cm^{-1} as compared to the MECP close to T_1^{ring} with SOC of only 0.9 cm^{-1} (Table 4.2). In the case of 4tThy and dtThy, the MECP closest

Table 4.2: Energetic and topological parameters of thymine and the thiothymines.

	2tThy	4tThy	dtThy	Thy
T_1^{pyr} – T_1^{ring} energy (eV)[a]	–0.002	2.26	0.69	1.79
Relevant T_1 minimum	Both	T_1^{ring}	T_1^{ring}	T_1^{ring}
$\pi_2^* - \pi_4^*$ orbital energy (eV)[b]	0.71	2.47	1.06	2.02
SOC of MECP near T_1^{pyr} (cm^{-1})	**105.3**[c]	23.0	49.7	30.7
SOC of MECP near T_1^{ring} (cm^{-1})	0.9	**3.4**	**3.4**	0.5
Barrier associated with MECP near T_1^{pyr}, $\Delta E^{\ddagger}$ (eV)[a]	0.25	0.45	0.30	0.07[d]
Barrier associated with MECP near T_1^{ring}, $\Delta E^{\ddagger}$ (eV)[a]	0.23	0.64	1.07	0.15[d]

[a]Calculated at the MS-CASPT2 level on SA-CASSCF optimized structures. [b]Orbital energies calculated at the Hartree-Fock/cc-pVDZ level on MP2/cc-pVDZ optimized ground state minima. [c]SOCs in bold indicate the MECP involved in the feasible T_1 decay pathway. [d]This pathway is not feasible due to low SOC.

to T_1^{ring}, the only energetically relevant minimum, have reasonable SOCs of 3.4 cm^{-1} (Table 4.2). The large SOC at the the MECP close to T_1^{pyr} is in stark contrast with the relatively small SOC at the MECP close to T_1^{ring}, and is seen across all molecules. This is in accordance with El-Sayed's rule as the MECP close to T_1^{pyr} is of $n\pi_2^*$ nature (Figure 4.5), which is different from the molecular symmetry of the ground state, while the MECP close to T_1^{ring} is of $\pi\pi_4^*$ nature, and thus has the same molecular symmetry as that of the ground state [87, 88].

The T_1 deactivation channels of each molecule are obtained by finding the path connecting the relevant T_1 minimum to the respective MECP with the S_0 PES (Figure 4.6). The energy barrier to access the MECP from the T_1^{pyr} minimum in the case of 2tThy is 0.25 eV, which is just the energy difference between the minimum and MECP and

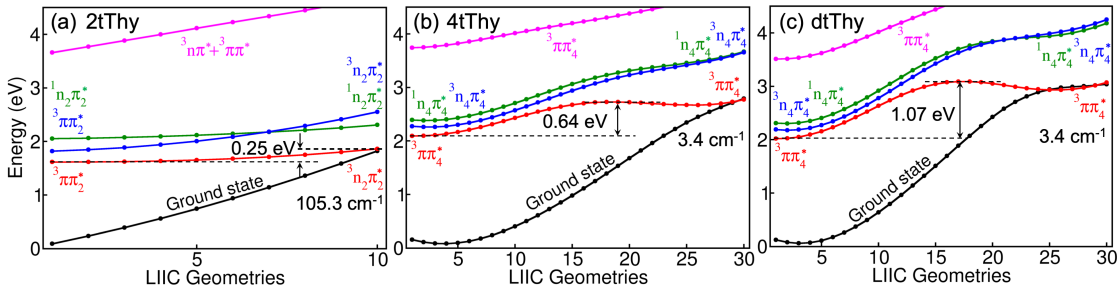

Figure 4.6: LIIC scans connecting the T_1 minimum to the respective minimum energy crossing point for the thiothymines – 2tThy, 4tThy and dtThy.

there is no additional barrier along the path. For 4tThy and dtThy, the energy barriers to reach the MECPs from the relevant minima are 0.64 eV and 1.07 eV, respectively, as estimated from LIIC scans shown in Figure 4.6. Regarding the barriers associated with the high-energy MECP in 4tThy and dtThy, while at first glance, the values may seem small (Table 1), note that the barriers are calculated from the T_1 minimum closest to the MECP (T_1^{pyr}), which in turn are high-lying minima.

The mechanisms of triplet decay and barriers for the three molecules are thus quite different. 2tThy decays through the MECP close to the pyramidalized triplet minimum, while 4tThy and dtThy decay through the MECP near the ring-distorted minimum and have higher barriers. The trend in the barrier heights of 2 and 4tThy are consistent with their T_1 lifetimes measured in acetonitrile, which are 2.7 μs and 4.2 μs [58, 59]. While the calculated SOCs and barriers suggest a greater difference than the experimentally observed difference of 1.5 μs, our calculations do not account for other factors which affect ISC like spin-vibronic coupling [87] and solvent effects [85]. It should be pointed out that the gas phase lifetimes of thiothymines have not been reported so far, which would have allowed for better comparison with our calculations. Also, the lifetime of dtThy has not been reported either in the gas or solution phase. In any case, the major focus of this work is identifying the underlying electronic structure responsible for the

different triplet decay mechanisms, rather than quantitatively modeling the observed lifetimes. This is discussed in the next subsection.

It is worth noting here that recent gas phase experiments on the closely related molecules, 2- and 4-thiouracil, estimate the triplet lifetime of these molecules to be 109 ps and $>$ 1500 ps, respectively [85, 89], a trend just like the thiothymines. Experiments also bring into consideration another seemingly inconsequential aspect namely the role of the methyl group at the C^5 position, which differentiates uracil and thymine. In a study by Vendrell-Criado et al, the T_1 lifetimes of 2tUra and 2tThy in acetonitrile were measured to be 70 ns and 2.3 μs, respectively [83]. To understand the cause of this significant difference, we calculated T_1 decay pathways for 2tUra analogous to the pathways in 2tThy. The structures, barriers and SOCs were found to be similar to the ones in 2tThy (Table 4.3) and do not explain the observed difference in T_1 lifetimes. We speculate that this difference has a dynamical origin [90, 91] and warrants further investigation.

Table 4.3: Energetic and topological parameters for 2-thiothymine and 2-thiouracil.

	2-thiothymine	2-thiouracil
$T_1^{pyr} - T_1^{ring}$ energy (eV)[a]	0.02	–0.14
Relevant T_1 minimum	Both	Both
$\pi_2^* - \pi_4^*$ orbital energy (eV)[b]	0.71	0.84
SOC of MECP near T_1^{pyr} (cm^{-1})	103	80
SOC of MECP near T_1^{ring} (cm^{-1})	0.9	0.7
Barrier for relevant T_1 decay pathway, $\Delta E^{\ddagger}$ (eV)[a]	0.3	0.3

[a] Calculated at the SS-CASPT2 level on SA-CASSCF optimized structures with a 14,10 active space and 6-31G** basis set. [b] Orbital energies calculated at the Hartree-Fock/cc-pVDZ level on MP2/cc-pVDZ optimized ground state minima.

4.3 Electronic Delocalization Modulates the Energy of the Triplet Minima

The striking difference in the triplet dynamics depending on the position of thionation in thymine can be explained by a careful analysis of the electronic delocalization in each molecule. There is an interplay between two types of delocalization: that due to (a) conjugation of the C^4=X and C^5=C^6 double bonds, which stabilizes the π_4^* orbital, and (b) the size of the atom X, wherein the π_2^* and π_4^* orbitals get stabilized depending on whether C^2 or C^4 is substituted with the larger atom, respectively [42].

In 2tThy, while the π_4^* orbital enjoys stabilization due to conjugation of C^4=O and C^5=C^6, π_2^* is stabilized due to thionation and this brings the two orbitals very close in energy with a difference of only 0.71 eV between them (Table 4.2). In 4tThy, the gap between the π_2^* and π_4^* orbitals is the largest (2.47 eV) as the π_4^* orbital is stabilized by both thionation and delocalization. It follows that the gap between the two anti-bonding orbitals in dtThy is the intermediate of the two, at 1.06 eV. Since the two minima, T_1^{pyr} and T_1^{ring}, are characterized by excitation to the π_2^* and π_4^* anti-bonding orbitals, respectively, the difference in energy between the orbitals is reflected in the energy difference between the two minima in each molecule (Table 4.2).

4.4 Design of New Photodynamic Therapy Drugs

The T_1 decay pathways and the calculated lifetimes indicate that 2tThy with its short lifetime would not make for a good PDT drug, while 4tThy and dtThy would be potential candidates.

The T_1 decay pathways and the calculated lifetimes indicate that 2tThy with its short lifetime would not make for a good PDT drug, while 4tThy and dtThy would be ideal candidates. This is corroborated by studies which have probed the efficacy of 4tThy [9, 92, 93] and dtThy [94] as potential PDT drugs. However, to broaden the library of

possible drug molecules, it is worth exploring if minor modifications of 2tThy would lead to an increased T_1 lifetime. A substitution could be made to 2tThy to increase the gap between the π_2^* and π_4^* orbitals, by stabilizing the π_4^* orbital. This would make T_1^{ring} significantly more stable than T_1^{pyr}, and increase the barrier to decay to the ground state. It would be reasonable to hypothesize that substituting an electron withdrawing group (EWG) at C^6 on the X=C^4-C^5=C^6 π system would pull electron density away from it, effectively increasing the nuclear attraction and decreasing the energy of the π system, both the bonding and anti-bonding π orbitals. An electron donating group (EDG) on the other hand, would have the opposite effect.

The hypothesis was first tested with three model π systems – ethylene, butadiene and $\alpha\beta$-unsaturated carbonyl – and it was seen that the prediction holds (Figure 4.7). Then, 2tThy was substituted with EWGs and EDGs at C^6 (see Figure 4.8) and the

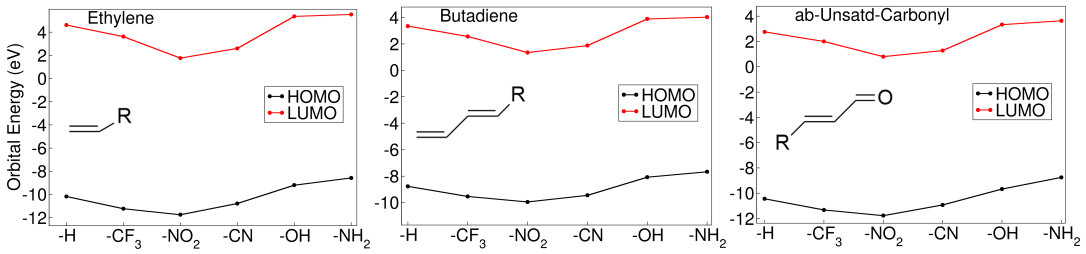

Figure 4.7: Orbital energies of model π systems substituted with electron withdrawing (–NO_2, –CF_3, –CN) and electron donating (–OH, –NH_2) groups.

orbital energies of these molecules were found to give consistent trends (Table 4.4).

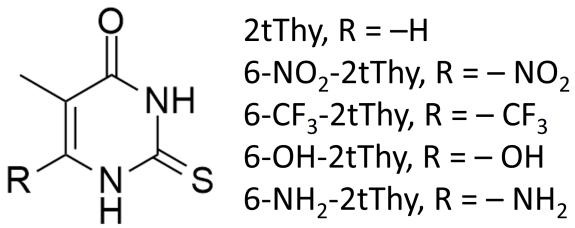

Figure 4.8: 2tThy analogues with electron withdrawing (–NO_2, –CF_3) and electron donating (–OH, –NH_2) groups substituted at C^6.

Table 4.4: Energies of the π_4^* and π_2^* orbitals and their comparison with the energy difference between the two minima optimized on the T_1 of 2-thiothymine analogues.

Substituent at C^6 of 2tThy	–H	$–NO_2$	$–CF_3$	–OH	$–NH_2$
π_4^* energy (eV)[a]	2.4	–0.2	1.6	3.3	3.3
π_2^* energy (eV)	3.1	2.3	2.7	2.7	2.8
$\pi_2^* - \pi_4^*$ energy (eV)	0.7	2.5	1.1	–0.6	–0.5
$T_1^{pyr} - T_1^{ring}$ energy (eV)[b]	–0.002	1.01	0.27	–[c]	–[c]

[a]Orbital energies calculated at the Hartree-Fock/cc-pVDZ level of theory on MP2/cc-pVDZ optimized ground state structures. [b]Calculated at the MS-CASPT2/10,7/6-31G** level of theory. [c]Only the T_1^{pyr} minimum could be optimized for these molecules.

The calculated orbital energies also indicate that the absorption maxima of 2tThy derivatives with EWGs should be redshifted with respect to 2tThy, while the derivatives with EDGs should be blue shifted. This is seen in Figure 4.9, where the vertical excitation energy for the first bright state of each molecule is plotted. It is also seen from Table 4.4

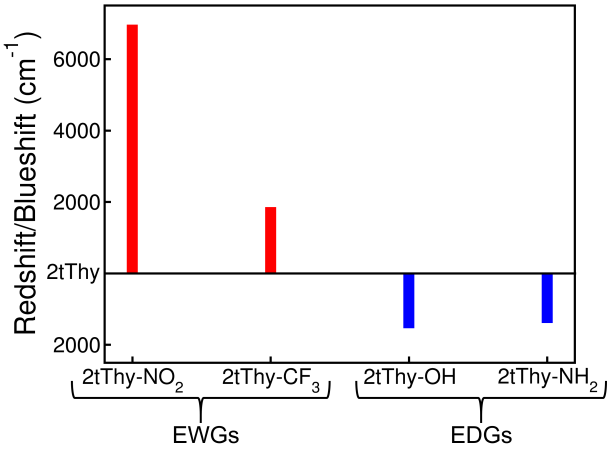

Figure 4.9: Redshifts/Blueshifts seen in 2tThy analogues with respect to 2tThy, by calculating the vertical excitation energy of their first bright state at CASPT2 (SA-CASSCF wave function composed of first six singlet states, 6-31G** basis set, (14,10) active space and a level shift of 0.2 a.u.) level of theory on MP2/cc-pVDZ optimized ground state geometries. The 2tThy analogues are generating by substituting EWGs ($–NO_2$, $–CF_3$) and EDGs (–OH, $–NH_2$) at C^6 of 2tThy.

that the trends in the orbital energies get reflected in the energy difference between the two minima on the T_1 state. In 2tThy analogues with a EWG substituted at C^6,

T_1^{ring} is the energetically relevant minimum on the T_1 PES. The MECP associated with this minimum has low SOC (Table 4.5) and this translates to slow T_1 decay. On the

Table 4.5: Spin-orbit coupling values of the MECPs of the 2-thiothymine analogues.

	SOC (cm^{-1})
SOC of MECP near T_1^{ring}	0.28
SOC of MECP near T_1^{pyr}	41.16
SOC of MECP near T_1^{ring}	0.40
SOC of MECP near T_1^{pyr}	102.69
SOC of MECP near T_1^{pyr}	99.17
SOC of MECP near T_1^{pyr}	106.68

other hand, for 2tThy analogues with an EDG at C^6, the orbital energies suggest that T_1^{pyr} is the energetically relevant minimum and the high SOC of the MECP associated with this minimum implies that these analogues would have favorable ISC and a short triplet lifetime. Effectively, we have a design principle to increase as well as decrease the lifetime of the T_1 state of 2tThy, by substituting EWGs, $–NO_2$ and $–CF_3$, and EDGs, –OH, $–NH_2$, at C^6, respectively.

4.5 Conclusions

The T_1 decay dynamics of thiothymines has been investigated using the multi-reference CASSCF and MS-CASPT2 electronic structure methods. For all the thiothymines, two triplet minima, T_1^{pyr} and T_1^{ring} have been optimized, and are found to be characterized by transitions to two different anti-bonding orbitals, π_2^* and π_4^*, respectively. Due to the energetic proximity of these two orbitals in 2tThy, this molecule exhibits a double well feature in its T_1 PES. Conversely, in 4tThy and dtThy, the large separation between the π_2^* and π_4^* orbitals ensures that there is only one effective minimum, T_1^{ring}, on the T_1 PES. The fundamental reason for the characteristic orbital energies is the different electronic natures of the C^2=X and C^4=X (X=O, S) bonds in thiothymines. The C^4=X

bond is conjugated with C^5=C^6 and therefore the associated π_4 and π_4^* orbitals are more delocalised than the corresponding π_2 and π_2^* orbitals. Moreover, electrons along a C=S bond are more delocalised than a C=O bond due to the larger atomic size of S. There is an interplay between these two factors, conjugation and size-driven delocalization, which ultimately determines the orbital energies and T_1 surface topologies of thiothymines.

The pathways for triplet decay of all the thiothymines have been determined and compared by optimizing the T_1/S_0 MECPs, and estimating the energy barriers for intersystem crossing. A strategy for controlling intersystem crossing and excitation energy by substitution on the thiothymine ring has been proposed, thus demonstrating how fundamental understanding of molecular electronic structure can assist in designing molecules with desired properties.

Chapter 5

Dependence of Photoproperties of Thioxanthines on Position of Sulphur Substitution

Xanthine is a purine base, very similar to the purine nucleobase, guanine. It is found widely in plants and animals, and can be found in most human tissues and fluids. Several derivatives of xanthine (Xan), obtained by methylation of the nitrogen atoms at positions 1, 3 and 7 (see Figure 5.1 for numbering), are naturally occurring stimulants. Caffeine is a derivative of Xan where all three N are methylated. Theobromine, found in cacao (chocolate) and kola, is a derivative of Xan where N^3 and N^7 are methylated, and theophylline, found in tea and cacao, is a derivative where N^1 and N^3 are methylated. Its wide presence in humans, animals, and plant sources endorses its bio compatibility.

Xan has two exocyclic oxygen atoms, not unlike thymine (Thy), which can be substituted with sulphur. Interestingly, 2,6-dithiopurine, which is equivalent to 2,6-dithioxanthine (dtXan), has been proposed as a potential PDT. This is attributed to not just its redshift in absorption, but also a nearly two-fold increase in its triplet life-

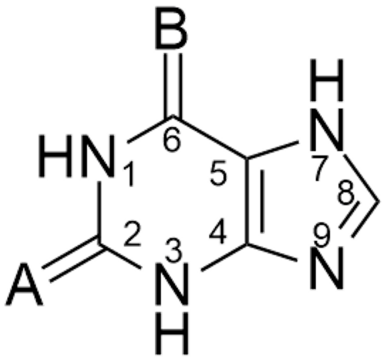

Xan, A = O, B = O
2tXan, A = S, B = O
6tXan, A = O, B = S
dtXan, A = S, B = S
2SeXan, A = Se, B = O
6SeXan, A = O, B = Se
dSeXan, A = Se, B = Se
2TeXan, A = Te, B = O
6TeXan, A = O, B = Te
dTeXan, A = Te, B = Te

Figure 5.1: Structure of xanthine indicated as Xan, and its derivatives obtained by substituting sites A and B with chalcogens, S, Se and Te.

time compared to thiothymines [94]. The study which proposed this, also studied the anti-tumor activity of 2,6-dithiopurine on human skin cancer cells in vitro [94]. Drawing another similarity to Thy, one of the carbonyls in Xan, at C^6, is conjugated with an adjacent double bond, while the other carbonyl at C^2, is an isolated π system. Xanthine, therefore, presents us with the opportunity to study the substitution of these exocyclic oxygen atoms with other chalcogens on its photophysical properties, in a site-dependent manner. Previously, in Chapters 3 and 4, some very clear trends were found in the photophysical properties of Thy derivatives depending on the position of substitution. If these trends prevail in Xan as well, it would attest to the generality of these structure-property relationships.

Another motivation to study Xan is its structural similarity to several naturally occurring stimulants such as caffeine, theobromine and theophylline, only differing by a methyl group. Since the methyl group is unlikely to significantly change the electronic structure properties, studying Xan will help in understanding their electronic structure as well.

5.1 Computational methodology

All ground state structures were optimized at the MP2 [95] level of theory using the cc-pVDZ [47–51] basis set. Vertical excitation energies were calculated on these optimized structures using the MS-CASPT2 [39, 40] method (a level shift [45] of 0.3 was used) for the first 7 singlet states, to account for at least two bright states for each molecule. The cc-pVTZ basis set was used for all atoms, except for Te, where the pseudopotential basis set, cc-pVTZ-pp was used [47–51]. An active space consisting of 12 electrons in 9 orbitals was used, and is shown in Figure 5.2 for dtXan. The same active space was used for geometry optimizations of triplet excited states which was carried out at the SA-CASSCF [35, 36] level of theory using a state-averaging of two singlet and three triplet states. The energies of the obtained excited minima were refined using the SS-CASPT2 [38] (a level shift of 0.3) method, in lieu of the more expensive MS-CASPT2 method. SS-CASPT2 was used to calculate energies along the LIIC pathways as well.

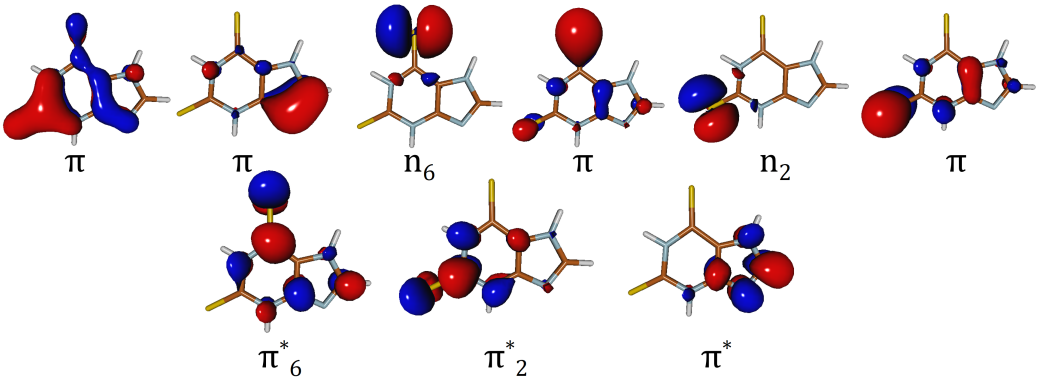

Figure 5.2: Active space of dtXan optimized at the SA-CASSCF level. The same active space of 12 electrons in 6 orbitals has been used for Xan and all its derivatives.

5.2 Electronic Spectra of Thioxanthines

The vertical excitation energies of Xan and the thioxanthines (2-thioxanthine (2tXan), 6-thioxanthine (6tXan) and dtXan) can be found in Table 5.1. For lack of a comprehensive

experimental study, where the excitation energies of Xan and the thioxanthines are given, the calculated values are compared with the experimental values of caffeine and the thiocaffeine series [96]. The same study also gives excitation energies for theophylline and the thiothephylline series (given in parenthesis along with the caffeine values). Excitation energies for the thiotheophylline series are very similar to those of the thiocaffeine series. This again points to the lack of significant change in the electronic structure due to the methyl group, which makes it reasonable to compare our calculations with that of the caffeine/theophylline series.

Table 5.1: Vertical excitation energies in eV (oscillator strengths in parenthesis) of xanthine and the thioxanthines. Calculated at the MS-CASPT2 level of theory, on MP2 optimized ground state geometries. Experimental values given for caffeine (theophylline) and thiocaffeine (thiotheophylline) series.

Xan		Expt[a]	2tXan		Expt
State	Energy		State	Energy	
$^1\pi\pi^*_6$	5.68 (0.10)	4.54 (4.56)	$^1n_2\pi^*_2$	4.27 (0.00)	
$^1n_2\pi^*_2$	5.91 (0.00)		$^1\pi\pi^*_6$	5.14 (0.07)	4.34 (4.34)
$^1n_6\pi^*_6$	6.54 (0.00)		$^1\pi\pi^*_2$	5.37 (0.71)	5.15 (5.23)
$^1\pi\pi^*_6$	6.85 (0.22)		$^1n_2\pi^*_6$	5.90 (0.00)	
$^1n_2\pi^*_6$	7.72 (0.00)		$^1\pi\pi^*$	6.46 (0.05)	
$^1\pi\pi^*_6$	8.16 (0.54)		$^1\pi\pi^*_6$	7.31 (0.31)	
6tXan		Expt	dtXan		Expt
State	Energy		State	Energy	
$^1n_6\pi^*_6$	3.42 (0.00)		$^1n_6\pi^*_6$	3.54 (0.00)	
$^1\pi\pi^*_6$	4.49 (0.54)	3.59 (3.59)	$^1n_2\pi^*_2$	4.15 (0.00)	
$^1\pi\pi^*$	5.85 (0.18)	3.68 (3.69)	$^1\pi\pi^*_6$	4.47 (0.15)	3.45 (3.52)
$^1\pi\pi^*_6$	5.88 (0.02)	4.61 (4.54)	$^1n_2\pi^*_6$	4.83 (0.00)	
$^1n_6\pi^*$	6.32 (0.00)		$^1\pi\pi^*_6$	5.02 (0.84)	4.09 (4.13)
$^1n_6\pi^*$	7.36 (0.00)		$^1\pi\pi^*_2$	5.32 (0.60)	4.77 (4.84)

[a]Experimental values taken from Reference [96].

The calculated values are consistently higher than the experimental values, which are expected since the experiment was carried out in solvent (ethanol) [96]. The relative values however, match reasonable well with the experimental values. Most significant, is the observation that the redshift is significantly higher when sulphur is substituted at

Table 5.2: Vertical excitation energies in eV (oscillator strengths in parenthesis) of selenoxanthines and teluroxanthines. Calculated at the MS-CASPT2 level of theory, on MP2 optimized ground state geometries.

2SeXan		6SeXan		dSeXan	
State	Energy	State	Energy	State	Energy
$^1n_2\pi^*_2$	3.73 (0.00)	$^1n_6\pi^*_6$	3.03 (0.00)	$^1n_6\pi^*_6$	3.05 (0.00)
$^1\pi\pi^*_6$	4.60 (0.62)	$^1\pi\pi^*_6$	3.98 (0.48)	$^1n_2\pi^*_2$	3.59 (0.00)
$^1\pi\pi^*_2$	4.96 (0.15)	$^1\pi\pi^*$	5.51 (0.21)	$^1\pi\pi^*_6$	3.93 (0.08)
$^1n_2\pi^*_6$	5.33 (0.00)	$^1n_6\pi^*$	5.79 (0.00)	$^1n_2\pi^*_6$	4.14 (0.00)
$^1\pi\pi^*$	6.31 (0.02)	$^1\pi\pi^*$	5.97 (0.03)	$^1\pi\pi^*_6$	4.32 (0.88)
$^1\pi\pi^*_6$	7.05 (0.20)	$^1n_6\pi^*$	7.02 (0.00)	$^1\pi\pi^*_2$	4.75 (0.59)
2TeXan		6TeXan		dTeXan	
State	Energy	State	Energy	State	Energy
$^1n_2\pi^*_2$	3.15 (0.00)	$^1n_6\pi^*_6$	2.29 (0.00)	$^1n_6\pi^*_6$	2.45 (0.00)
$^1\pi\pi^*_2$	3.76 (0.60)	$^1\pi\pi^*_6$	3.28 (0.49)	$^1n_2\pi^*_2$	2.91 (0.00)
$^1\pi\pi^*_6$	4.67 (0.03)	$^1\pi\pi^*$	4.94 (0.19)	$^1\pi\pi^*_6$	3.13 (0.19)
$^1n_2\pi^*_6$	4.89 (0.00)	$^1n\pi^*$	5.22 (0.00)	$^1\pi\pi^*_6$	3.35 (0.69)
$^1\pi\pi^*$	6.19 (0.01)	$^1\pi\pi^*$	5.47 (0.03)	$^1n_2\pi^*_6$	3.54 (0.00)
$^1\pi\pi^*$	6.82 (0.04)	$^1n_6\pi^*$	6.25 (0.00)	$^1\pi\pi^*_2$	4.03 (0.53)

the 6th position (1.19 eV calculated and 0.95 eV experimentally) as opposed to sulphur substitution at the 2nd position (0.54 eV calculated and 0.20 eV experimentally). The excitation energies of other chalcogen (Se and Te) substituted xanthine are given in Table 5.2.

When we look closely at the orbitals involved in the excitations (Figure 5.3), we see that the LUMO in all the molecules are localized over the C^6=X (X=O, S) atoms. These observations are very similar to the ones in Thy and the thiothymines (Figure 3.5). We can therefore, invoke the hypothesis that two types of delocalization are in play in Xan, one due to the conjugation between the C^6=X and C^5=C^4 double bonds, and the other due to the size of X that is substituted [42]. One critical difference in the thioxanthine series in comparison to the thiothymines series, is the second bright state in 6tXan and 4tThy. While the second bright state in 4tThy involves a transition from HOMO-1 to LUMO, the excitation in 6tXan involves a transition from HOMO to LUMO+1. The

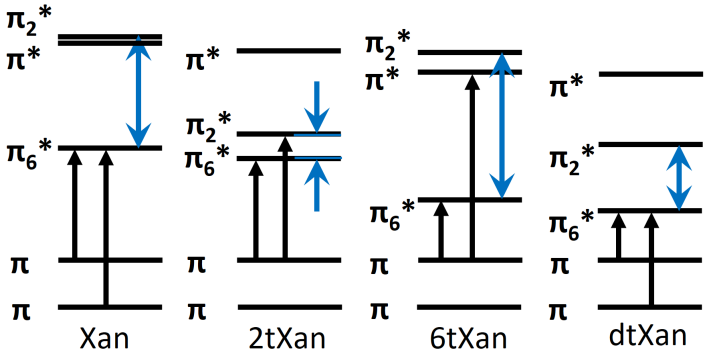

Figure 5.3: Transitions characterizing the first two bright states (black arrows) in Xan and thioxanthines. The blue double-arrows represent the energy difference between the π_2^* and π_6^* orbitals.

LUMO+1 in 6tXan is not the π_2^* orbital, as was observed for the thiothymine series. This orbital roughly corresponds to the orbital labelled as π^* in Figure 5.2. This implies that the π system delocalised over the C^6=X bond does not only include the C^5=C^6 double bond, but may also include the N^9=C^8 double bond.

5.3 Predictions of the Particle-in-a-Box Model

The particle-in-a-box (PIB) model was used, in the same manner as was applied for Thy and the thiothymines (see Chapter 3 for full description), to calculate the HOMO and LUMO energies for Xan and the thioxanthines [42, 64–66]. The HOMO and LUMO energies are calculated for the 2 electron C^2=X system, the 4-electron C^4=C^5—C^6=X system and the 6 electron C^8=N^9—C^4=C^5—C^6=X system. The box lengths for the C^2=X and C^8=N^9—C^4=C^5—C^6=X systems were calculated as shown in Figure 5.4, and the HOMO and LUMO energies for all three systems are given in Table 5.3. These energies for the C^2=X and C^8=N^9—C^4=C^5—C^6=X systems are plotted in Figure 5.5 and they indicate that the HOMO energies do not change much in comparison to the LUMO energies. This is similar to what was seen for Thy and the thiothymines (see Figure 3.8). Therefore, we have focused only on the LUMO energies and these have been

plotted in Figure 5.6.

Table 5.3: HOMO and LUMO energies for the C^2=X, C^4=C^5—C^6=X and C^8=N^9—C^4=C^5—C^6=X systems with different substitutions (X=O, S, Se, Te) from the PIB model.

	C^2=X		C^4=C^5—C^6=X		C^8=N^9—C^4=C^5—C^6=X	
X	HOMO (eV)	LUMO (eV)	HOMO (eV)	LUMO (eV)	HOMO (eV)	LUMO (eV)
O	5.52	22.08	5.09	9.04	5.06	11.38
S	3.18	12.71	4.21	7.48	3.83	8.61
Se	2.69	10.77	3.95	7.02	3.50	7.86
Te	2.18	8.71	3.63	6.45	3.11	6.99

When we consider Xan with substitutions at C^2, the PIB model predicts that the LUMO will be localized over the C^6=X region when X is oxygen or sulphur, irrespective of whether the C^6=O bond is considered to be a part of the C^4=C^5—C^6=O or the C^8=N^9—C^4=C^5—C^6=O system. However, when the C^4=C^5—C^6=O system is considered, it predicts a shift of the LUMO to the C^2=X region when X is Se, while when the C^8=N^9—C^4=C^5—C^6=O system is considered, a shift of the LUMO to the C^2=X region is predicted only when X is Te. This uncertainty is clarified when we see the SA-CASSCF orbitals, optimized for the first 7 singlet states, in Figure 5.7. The shift of the LUMO to the C^2=X region is seen only for Te, thus supporting the hypothesis that the C^6=X π bond is a part of the 6 electron C^8=N^9—C^4=C^5—C^6=X system.

These results indicate the wide generality of the PIB model in predicting LUMO energies between two differently delocalised sites in a molecule, taking into account both the conjugation effect as well as the effect of the size of the substituted atom on the delocalization. Note however, that in the case of the C^8=N^9—C^4=C^5—C^6=X system, the PIB model does not account for the fact the π system is not actually linear. This has been done intentionally to retain the model's simplicity and elegance. The ability of the PIB model to correctly predict the trends in the ordering of the LUMO, despite not accounting for the non-linearity of the π system further substantiates its predictive

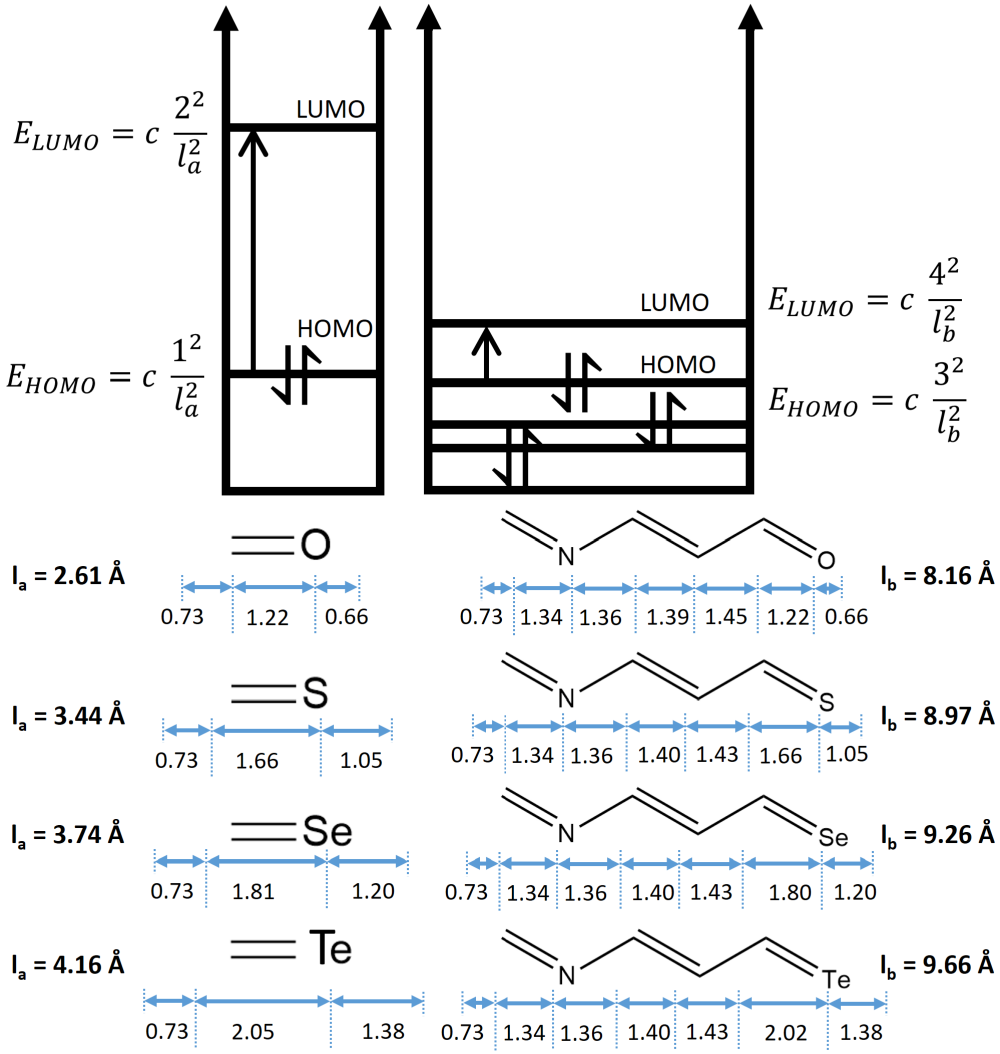

Figure 5.4: Particle-in-a-box models for the C^2=X and C^8=N^9—C^4=C^5—C^6=X (X = O, S, Se, Te) systems. The lengths and energy levels of the two boxes are to scale for the C^2=O and C^8=N^9—C^4=C^5—C^6=O systems. All bond lengths are given in Angstroms and taken from MP2/cc-pVDZ optimized calculations. The additional lengths at the ends of the molecule are covalent radii taken from Ref [67]. The energy states are filled according to Pauli's exclusion principle and the formulae to calculate HOMO and LUMO energies are given alongside. The constant c (37.606 eV) incorporates Planck's constant, mass of electron, a factor of 1/8 and conversion of joules to electron volts. The variables l_a and l_b represent the box length in Å of the C^2=X and C^8=N^9—C^4=C^5—C^6=X systems respectively.

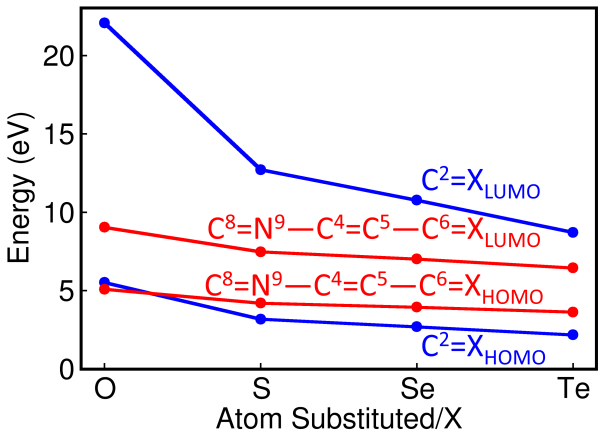

Figure 5.5: HOMO and LUMO energies in eV for the C^2=X and C^8=N^9—C^4=C^5—C^6=X (X = O, S, Se, Te) systems.

ability.

5.4 Topology and Dynamics of the T_1 State of Thioxanthines

An attempt was made to look for two minima on the T_1 surface, analogous to what was found in the thiothymine series. The same protocol as before was used, wherein the Franck-Condon (FC) geometry was used as the starting structure to optimize the nearly planar minimum which involves a transition to the π_6^* orbital (π_4^* orbital in the case of the thiothymines), and a structure where the C^2=X bond is stretched by about 0.2 Å and pyramidalized by about 30° was used as the starting structure to optimize the pyramidalized minimum which involves a transition to the π_2^* orbital. In this manner, two minima were successfully optimized for Xan and the three thioxanthines.

The structures of these minima (indicated as T_1^{ring} and T_1^{pyr}, as previously done for the thiothymines) along with the associated orbitals are shown in Figure 5.8 and the LIIC scans connecting these two minima are shown in Figure 5.9. The discontinuities in the LIIC scans of Xan and 6tXan can be attributed to a sudden change in the active

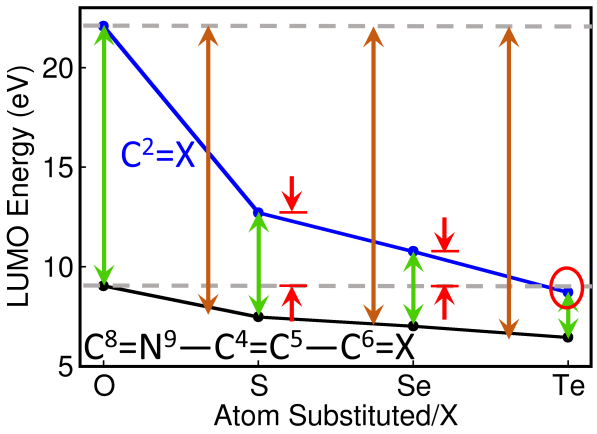

Figure 5.6: LUMO energies (in eV) as calculated from the Particle-in-a-box model for the C^2=X and C^8=N^9—C^4=C^5—C^6=X (X = O, S, Se, Te) systems. The energy gap between the π_2^* and π_6^* orbitals are represented by green double-headed arrows for disubstituted, brown double-headed arrows for 6-substituted, and red double-headed arrows for 2-substituted xanthines. The gray dashed lines are the LUMO energies for X = O for the two systems.

space, with the abrupt inclusion of the π_2^* orbital, which was initially absent at the T_1^{ring} structure. These discontinuities are also seen at the SA-CASSCF level, indicating that these discontinuities will persist even if the more accurate MS-CASPT2 method is used. Note however, that these discontinuities are not due to an abrupt change in the geometry and care has been taken to change the geometry smoothly.

In Xan, 6tXan, and dtXan, the T_1^{ring} minimum is more stable than the T_1^{pyr} minimum by 1.17 eV, 1.99 eV and 0.71 eV at the SS-CASPT2 level, respectively. This is in line with what is suggested by the orbital energies of the π_2^* and π_6^* orbitals. Energies of the orbitals calculated at the Hartree-Fock/cc-pVDZ level of theory (on MP2/cc-pVDZ optimized geometries) suggest that the π_6^* orbital is more stable than the π_2^* orbital in Xan, 2tXan, 6tXan and dtXan by 2.27 eV, 0.54 eV, 3.20 eV and 1.44 eV, respectively. In 2tXan however, T_1^{pyr} is found to be more stable by 0.44 eV. This is in contrast to what is suggested from the orbital energies which indicate that T_1^{ring} and T_1^{pyr} should be very close in energy. Further, if one minimum were indeed more stable than the

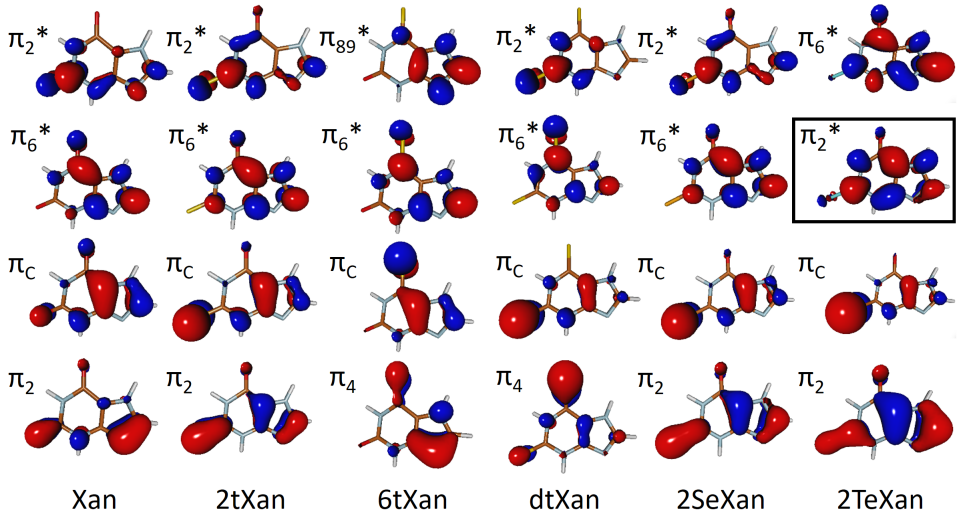

Figure 5.7: Orbitals characterizing the electronic transitions to the lowest two bright states, optimized at the SA-CASSCF level at the MP2 optimized geometry. Subscript '2' denotes location of the orbital primarily on the C^2=X bond, '6' on the C^6=X bond (X = O, S, Se and Te), 'C' on the C^4=C^5 bond, and '89' on the C^8=N^9 bond.

other, orbital energies suggest that it would be the T_1^{ring} minimum. The reason for this peculiar behaviour is explored in the forthcoming section (5.5).

Regarding the decay dynamics from the T_1 state, this is only explored from the T_1^{ring} minimum for Xan, 6tXan and dtXan, and the T_1^{pyr} minimum for 2tXan, based on the relative energies between these minima. The spin-orbit coupling (SOC) for the MECPs, shown in Figure 5.10, associated with the T_1^{ring} minima of Xan, 6tXan, and dtXan are nearly zero, and are not likely to assist in ISC processes (Table 5.4). The MECP associated with the T_1^{pyr} of 2tXan however, has a high SOC of 64.4 cm^{-1}. The LIIC scan connecting this minimum with its crossing shows no barrier, and the energy difference between the T_1^{pyr} minimum and the MECP is only 0.16 eV which is easily surmountable. Thus, we find that of Xan and all three thioxanthines, only 2tXan has a feasible pathway to access the ground state, and is therefore likely to have the shortest T_1 lifetime.

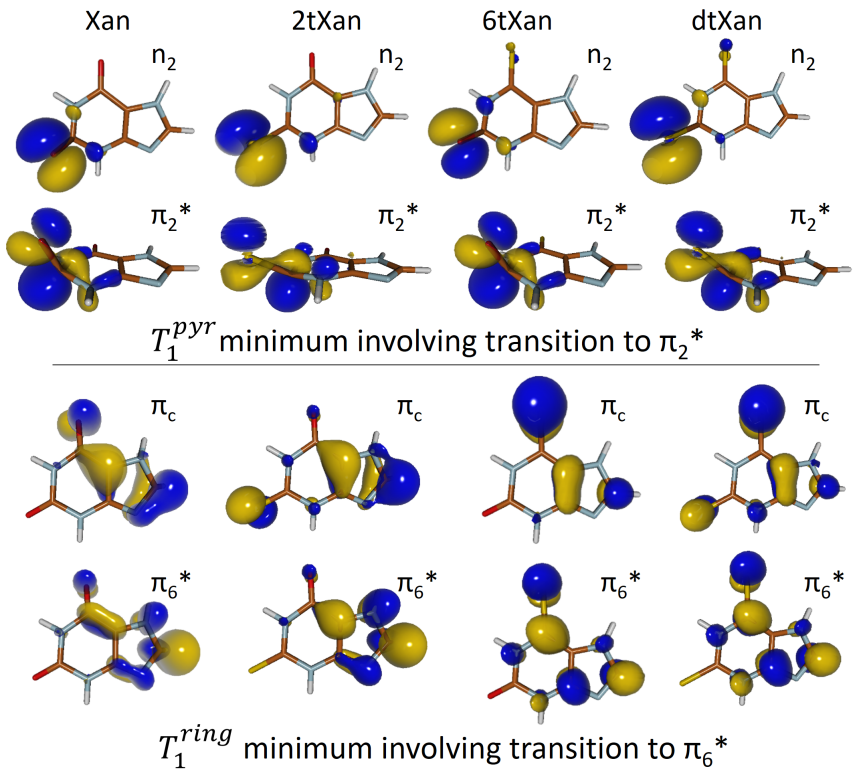

Figure 5.8: Molecular geometries of the two minima on the T_1 PES of Xan and thioxanthines, along with the orbitals involved in the T_1 transition. The minimum with strong pyramidalization at C^2=X (X=O, S) is characterized by a transition to the π_2^* orbital and is denoted as T_1^{pyr}, while the nearly planar structure is characterized by a transition to the π_4^* orbital and is denoted as T_1^{ring}.

5.5 2-Thioxanthine: A Cautionary Tale

In this section, the reason as to why the T_1^{pyr} minimum is more stable than the T_1^{ring} minimum in 2tXan, which is contrary to what is suggested by orbital energy trends is investigated. Initially however, starting with the assumption that the obtained structures (Figure 5.8) were incorrect, several attempts were made to optimize a 'better' T_1^{pyr} or T_1^{ring} minimum. However, all attempts converged to the already obtained structures. Methods were also varied to better refine the energies of the T_1 minima, but the relative energy difference always indicated that the T_1^{ring} minimum was more stable by about

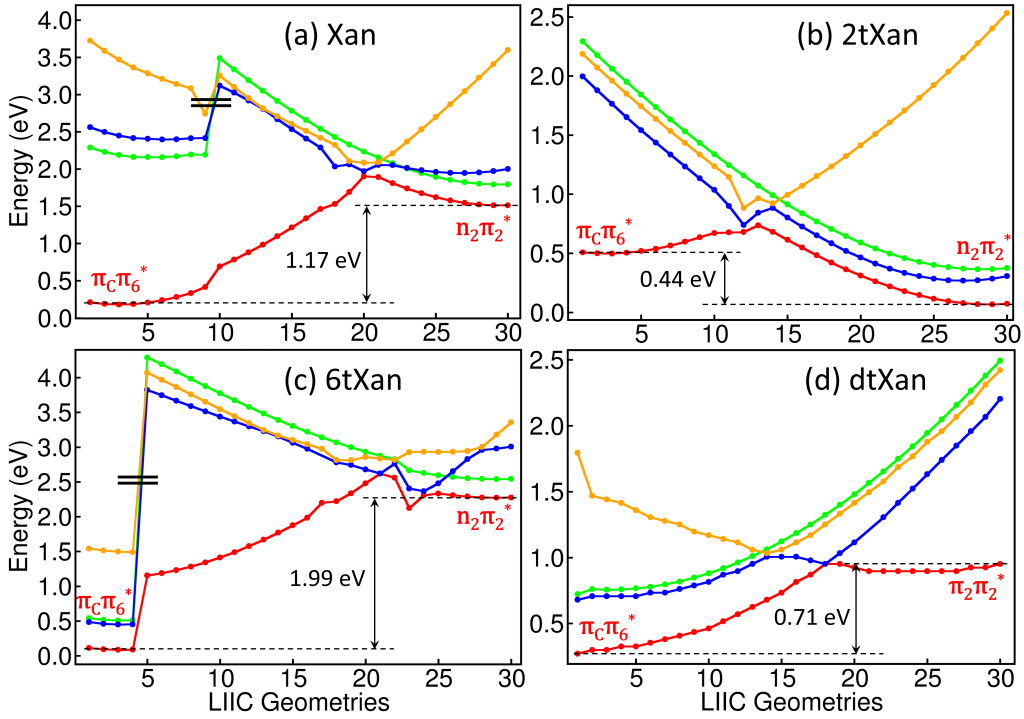

Figure 5.9: LIIC scans connecting the two T_1 minima, T_1^{pyr} and T_1^{ring}, of Xan and thioxanthines. Barriers are not specified as relative energies between minima, which are indicated, overshadow the barriers.

0.4 eV.

We then looked closely at the Hartree-Fock orbital energies, not at the FC geometry as seen previously, but at the T_1 minima. These energies were compared with those of the T_1 minima of 2tThy, where the two minima are almost degenerate. Firstly, only the energies of the orbitals from which the transitions originate (loosely termed as HOMO) are plotted in Figure 5.11, and it is seen that there is very little change in their energies, in either of the molecules or minima. Then, the energies of the orbitals where the transitions end (loosely termed as LUMO) are plotted in Figure 5.12, where, we see an interesting trend. Clearly, the anti-bonding orbital involved in the transition is most stable at its respective minimum. However, these orbitals are stabilized to a different extent with respect to the FC geometry. In 2tThy, the π_4^* orbital is stabilized by 2.14

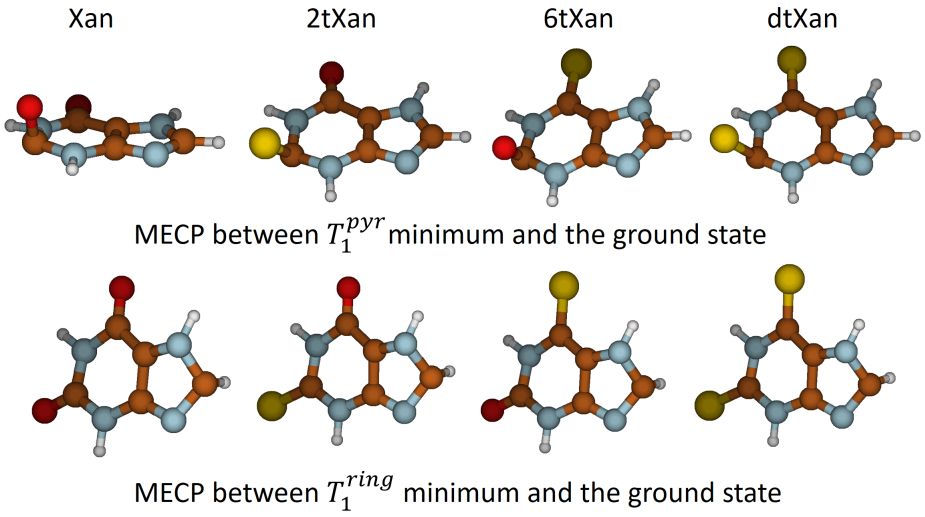

Figure 5.10: Minimum energy crossing points associated with the T_1^{pyr} and T_1^{ring} minima for Xan and the thioxanthines.

Table 5.4: Spin-orbit couplings of the MECPs of xanthine and the thioxanthines, along with the component of the coupling along x, y and z directions.

MECP	x	y	z	SOC[a] (cm^{-1})
Xan (π_2^*)[b]	1.87	25.35	0	25.42
Xan (π_6^*)	-0.01	-0.09	0	0.09
2tXan (π_2^*)	24.07	-59.69	0	64.36
2tXan (π_6^*)	-0.26	-0.14	0	0.30
6tXan (π_2^*)	-2.12	-24.95	0	25.04
6tXan (π_6^*)	-0.01	-0.06	0	0.06
dtXan (π_2^*)	-79.42	69.88	0	105.79
dtXan (π_6^*)	0.01	-0.07	0	0.07

[a]SOC is calculated as the square root of the sum of the squares of the x, y and z components.
[b]π_2^* or π_6^* refer to the anti-bonding orbital which is associated with the nature of the MECP.

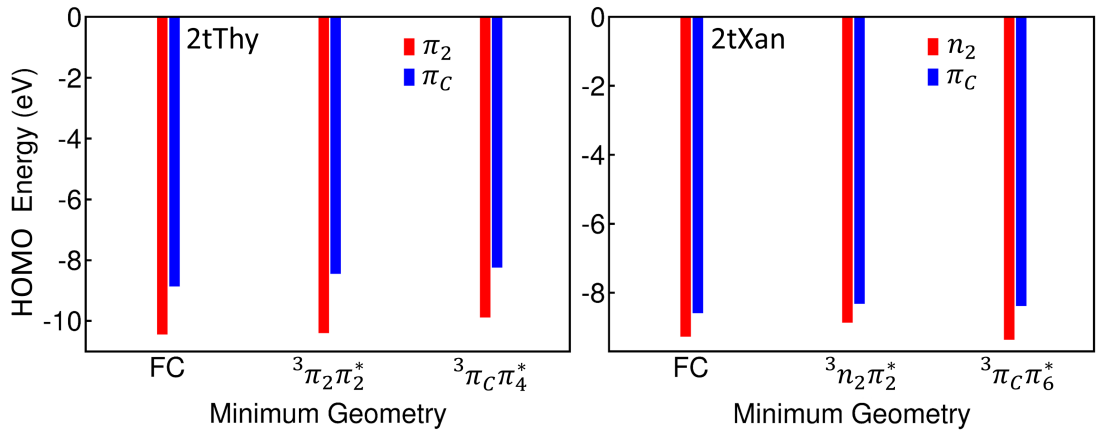

Figure 5.11: Energies in eV of the originating orbitals (called HOMO for simplicity) of the T_1^{pyr} (π_2 in 2tThy and n_2 in 2tXan) and T_1^{ring} (π_C in both) minima in 2tThy and 2tXan, along with the energies of the respective orbitals at the Franck-Condon (FC) geometry. Energies calculated at the Hartree-Fock/cc-pVDZ level of theory.

eV whereas the π_2^* orbitals is stabilized by a smaller magnitude (1.92 eV). This helps to maintain the ordering that these two orbitals had at the FC geometry i.e., the π_4^* orbital being more stable than the π_2^* orbital. In 2tXan, on the other hand, the π_2^* orbitals gets stabilized by 1.77 eV, while the π_6^* orbital only gets stabilized by 1.60 eV. This is in contrast to the ordering at the FC geometry, where the π_6^* orbital is more stable compared to the π_2^* orbital.

It would be imprudent to compare these orbital energies quantitatively with the relative energy difference between the two minima. It is quite clear, however, that orbital energy trends that hold at the FC geometry may not persist at different geometries such as the T_1 minima. In 2tThy, they continued to hold as the anti-bonding orbitals were stabilized in the same manner as their energy trends at the FC geometry. In 2tXan however, they are stabilized differently compared to their ordering at the FC geometry. While the reason as to why this is happening is an interesting question in itself, 2tXan is nevertheless a case where the predictive ability of the orbital energy trends do not hold at geometries other than the FC geometry. The case of this molecule, therefore,

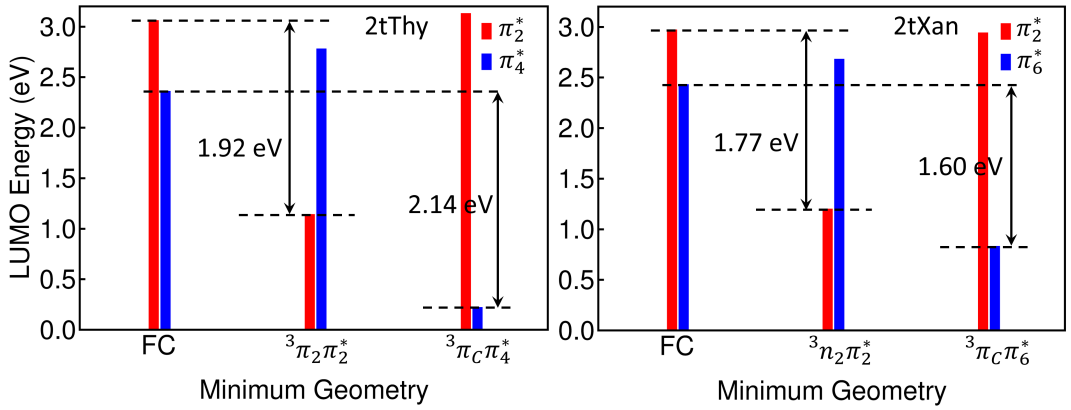

Figure 5.12: Energies in eV of the terminating orbitals (called LUMO for simplicity) of the T_1^{pyr} (π_2^* in both) and T_1^{ring} (π_4^* in 2tThy and π_6^* in 2tXan) minima in 2tThy and 2tXan, along with the energies of the respective orbitals at the Franck-Condon (FC) geometry. Energies calculated at the Hartree-Fock/cc-pVDZ level of theory.

recommends greater caution while using orbital energy trends at the FC geometry to make predictions about relative energies of different geometries.

Chapter 6

How Thiothymines Generate Singlet Oxygen Through Photosensitization

Photosensitization, very generally, is a light mediated physical reaction, where the molecule which is irradiated with light is not the final target. Typically a 'helping' molecule is photoexcited and is then expected to transfer its excess energy to the target molecule, thus exciting the target molecule, while the 'helping' molecule returns to its ground state after losing its excess energy. A common target of photosensitization is the oxygen molecule.

Oxygen, in its ground state, exists in a triplet state, meaning that its two valence molecular orbitals, which are degenerate, are singly occupied with the same spin (see Figure 6.1). This means a total spin, S, of 1 and a spin multiplicity (calculated as 2S+1) of 3, and hence the designation of 'triplet'. Direct photoexcitation of oxygen from its ground triplet state to its excited singlet state is spin-forbidden. However, it is possible to achieve this using a 'helping' molecule or a photosensitizer, and this bimolecular

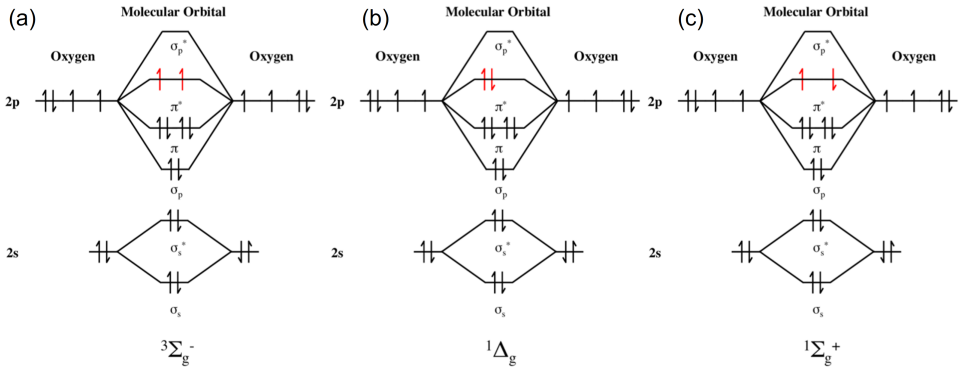

Figure 6.1: Molecular orbital diagrams of the (a) ground triplet, (b) first excited singlet, and (c) second excited singlet states of molecular oxygen, O_2.

energy transfer is represented in Eq. 6.1.

$$^3PS + ^3O_2 \rightarrow PS + ^1O_2 \tag{6.1}$$

Photosensitization of O_2 is widely made use of in organic synthesis [97–101], photovoltaics [102], and is also a key step in photodynamic therapy [21,24,103]. However, very little is known about the mechanism of this bimolecular nonradiative energy transfer reaction [104–108]. Our aim, in this chapter, is to better understand photosensitization, using thiothymines as the setting, since all three thiothymines are known to have significant singlet oxygen yields (see Table 1.1). Specifically, we wish to calculate their rates of photosensitization, and thereby obtain physical and mechanistic understanding of photosensitization.

6.1 Physical Interpretation of Photosensitization

6.1.1 R space and the mode to promote crossing

In the photosensitization reaction the spins of the individual components change, but the spin of the composite system remains a singlet (Eq. 6.2).

$$({}^3PS + {}^3O_2)^1 \rightarrow (PS + {}^1O_2)^1 \tag{6.2}$$

Therefore, this process is spin-allowed unlike intersystem crossing. This photophysical reaction can be thought to start when the photosensitizer (PS) is at its T_1 minimum energy geometry on its T_1 surface and is approached by a ground state O_2 molecule, also in its triplet state. When the distance between the PS and O_2 is large, there is little to no interaction between the two and the energy of the composite system is simply the sum of the energies of the components. The state ordering then, when the PS is in its T_1 minimum geometry, is as shown on the left of Figure 6.2. All of these 4 states are singlet states, and the first three are denoted as SS states (SS0, SS1 and SS2) since the spin multiplicities of the individual components are singlet, and the fourth state is denoted as TT0. SS0 and SS1 are doubly degenerate and correspond to the ${}^1\Delta_g$ states of O_2 while SS2 corresponds to the ${}^1\Sigma_g^+$ state of O_2. The TT0 state corresponds to the reactant state, and any of the three SS states correspond to the product. When internal coordinates of the PS (denoted as R) are changed to the minimum energy crossing point (MECP) geometry of the T_1 with the ground state, keeping the distance with the O_2 molecule (denoted as D) fixed at a large value, the state ordering follows the ordering of O_2, since the S_0 and T_1 energies of the PS are degenerate at this geometry (shown on the right of Figure 6.2). This difference in ordering between the 3 SS and 1 TT states across these two geometries clearly implies that there exists some internal distortion coordinate of the photosensitizer along which the TT0 state crosses the SS2 state. This crossing is

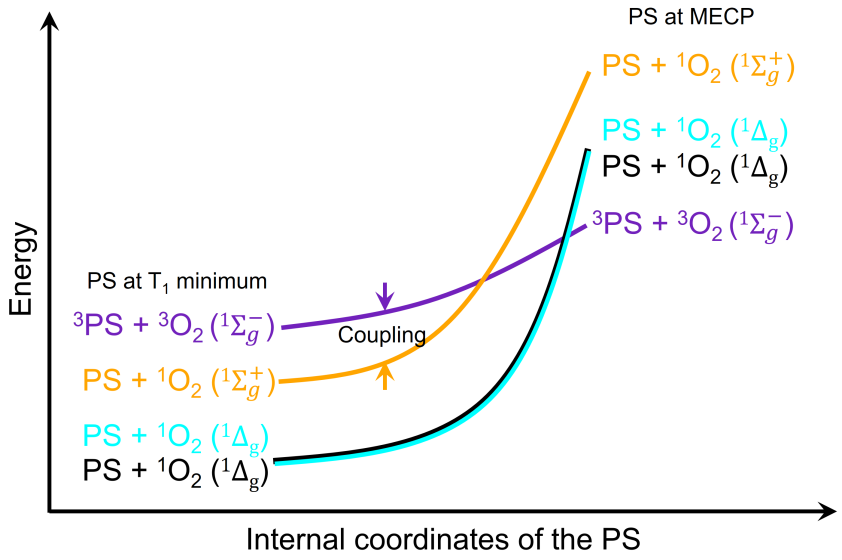

Figure 6.2: Schematic showing the ordering of states for the PS–O_2 composite system, along internal coordinates which promote crossing between the reactant (purple) and product (orange, cyan and black) states. The two states involving the $^1\Delta_g$ state of O_2 (cyan and black) are degenerate.

accessed at a certain barrier, and along the same coordinate the TT0 state also crosses the SS1 and SS0 states at even higher barriers. More detailed information about the internal coordinates that lead to this crossing can be found in Chapter 4, where the geometries of the MECPs have been optimized for all 3 thiothymines.

Since photosensitization is inherently a quantum process, it is not necessary for the reactant to move on its potential energy surface (PES) all the way to reach the crossing point. State transfer can be mediated through diabatic coupling at any point before reaching the crossing. The state orderings of the PS–O_2 composite system at these two geometries of the PS (T_1 minimum and MECP) is incontrovertible when the D is large, since the energy of the composite system is simply the addition of the individual components. We can expect these trends to hold at small D, provided the coupling between the states is small.

6.1.2 D space and diabatic coupling

In the D space, i.e., along the D coordinate with a fixed R, the energy of all states (SS0, SS1, SS2 and TT0) monotonically increase as shown in Figure 6.3 (here R is fixed as the T_1 minimum structure, and the bond length of O_2 is also unchanged). Note however, that moving along this coordinate does not promote crossing of the TT0 state with any of the SS states.

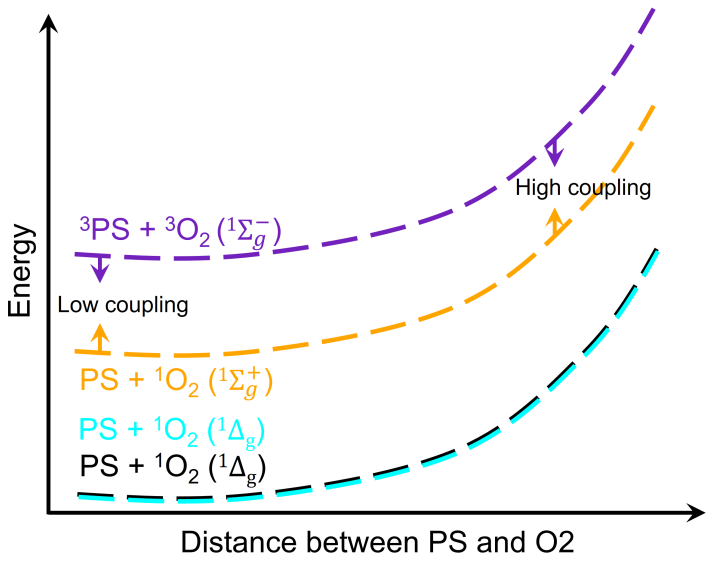

Figure 6.3: Schematic showing the states of the PS–O_2 composite system where the internal coordinates of PS and O_2 are fixed and the distance between them is varied. The internal coordinates of the PS correspond to its T_1 minimum. The states are shown as dashed lines to indicate that these are the states in the D space, and to differentiate them from the R space. Along this coordinate, the energies of the state monotonically increase and so does the diabatic coupling.

The diabatic coupling is calculated between any two states by first considering the adiabatic states and then using the diabatization scheme as given in Reference [28]. Since the diabatic coupling is a measure of the interaction between the PS and O_2, it would be nearly zero at large D and increase gradually as the PS and O_2 come closer. Here we make the usual assumption that the diabatic coupling is only dependent on the

D coordinate and mostly independent of the R coordinate, since the nature of the states do not change significantly when D is fixed and changes are made in the R space. This is illustrated in Figure 6.4, which shows the change in internal coordinates of the PS till both crossings are reached, for the T_1^{ring} conformer of 4tThy along the to4X approach direction, with the D fixed at 2.5 Å. The diabatic coupling between the TT0 and SS2 states can be calculated as half the energy gap between the diabatic states at the point where the two nearly cross (inset in Figure 6.4), and this is found to be 58.2 cm^{-1}. The diabatic coupling between these states, calculated at this D, using the diabatization scheme is calculated to be 27.6 cm^{-1}. This was also confirmed with the other two

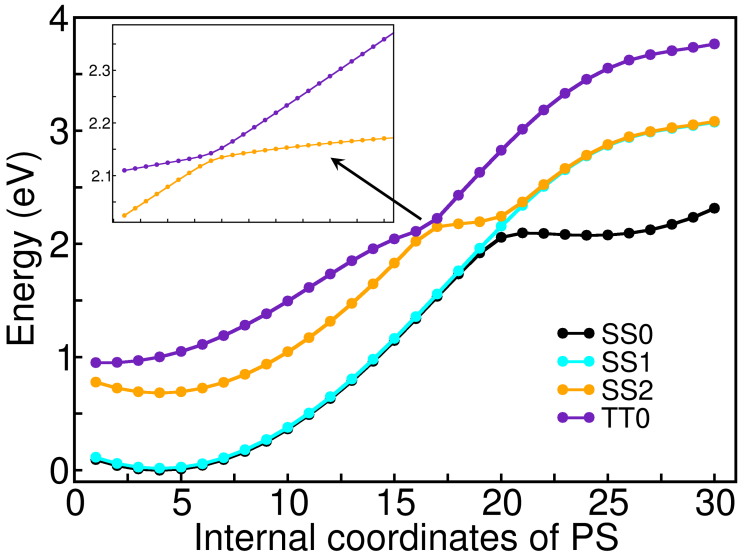

Figure 6.4: Calculated adiabatic energies of states for the PS–O_2 composite system, along the internal coordinates of the PS which promote crossing. The PS considered here is the T_1^{ring} conformer of 4tThy, along the to4X approach direction, with a D value of 2.5 Å. The inset shows more densely calculated points close to the crossing between the TT0 and SS2 states. The diabatic coupling given as half of the energy gap at the crossing is 58.2 cm^{-1}. The diabatic coupling calculated in the D space at this D is 27.6 cm^{-1}.

thiothymines, 2tThy (along to56 direction with a D of 2.8 Å) and dtThy (along to4X direction with a D of 2.4 Å), and the diabatic coupling from the diabatization scheme was calculated to be 6.6 cm^{-1} and 189.5 cm^{-1}, respectively, and that obtained by changing

their internal coordinates was found to be 1.0 cm^{-1} and 115.9 cm^{-1}, respectively. In all three cases, the diabatic coupling calculated with two different methods are similar and of the same order of magnitude.

In the previous section, the ordering of states at the T_1 minimum and MECP geometry of the PS for large D was discussed. While, it may initially seem that these state orderings would not persist at small D, our calculations of these states up to 2.2 Å, for all 3 thiothymines, find that the ordering is maintained. This is more a characteristic of the system being considered than a general point, and is related to this being a weakly coupled system. Since this energy transfer between PS and O_2, which can be thought of as a state transfer between the TT0 and any of the SS states of the PS–O_2 composite system, is mediated by a weak coupling, we are able to treat it perturbatively, using Fermi's golden rule to calculate the rate of nonradiative state transfer.

6.2 Fermi's Golden Rule

Fermi's golden rule (FGR), derived using time-dependent perturbation theory, gives the rate of nonradiative transition between an initial state to a continuum of final states, due to a weak perturbation, and is given as

$$k_{IF} = \frac{2\pi}{\hbar} \int |\langle \Psi_I | \hat{H}_{IF} | \Psi_F \rangle|^2 \delta(E_I - E_F) dE_F \tag{6.3}$$

where, $\hat{H}_{IF}$ is the Hamiltonian that couples the initial and final states, and Ψ_I and Ψ_F are the molecular wavefunctions of the initial and final states, respectively. In the case of photosensitization, where state is transfer is taking place between two states of the same spin multiplicity, $\hat{H}_{IF}$ becomes the electronic coupling, V. The Dirac delta function in Eq. 6.3 ensures conservation of energy.

Within the Born-Oppenheimer approximation, Ψ_I and Ψ_F can be split into electronic (ψ) and vibrational (ϕ) parts. Further, since the coupling V does not depend on the

nuclear coordinates, the vibrational part of the wavefunction is unchanged by V.

$$k_{IF} = \frac{2\pi}{\hbar} \int |\langle \psi_I | V | \psi_F \rangle|^2 |\langle \phi_i | \phi_f \rangle|^2 \delta(E_I - E_F) dE_F \tag{6.4}$$

where, $|\langle \phi_i | \phi_f \rangle|^2$, which is the square of the overlap of the vibrational wavefunctions is called the Franck-Condon Factor (FCF). Since FGR considers the transition from the lowest vibrational state of the initial electronic state, it can be written as

$$k_{IF} = \frac{2\pi}{\hbar} |\langle \psi_I | V | \psi_F \rangle|^2 \int |\langle \phi_i | \phi_{\{f\}} \rangle|^2 \delta(\Delta E_{IF} + E_i - E_{\{f\}}) dE_f \tag{6.5}$$

where, $\Delta E_{IF} = E_I - E_F$, is the electronic energy gap, and the integration is carried out over all the vibrational states of the final electronic state. The integral of the FCF along with the delta function is called Franck-Condon weighted density of states or FCWD.

$$\begin{aligned} k_{IF} &= \frac{2\pi}{\hbar} |\langle \psi_I | V | \psi_F \rangle|^2 \int FCF \ \delta(\Delta E_{IF} + E_i - E_{\{f\}}) dE_f \\ k_{IF} &= \frac{2\pi}{\hbar} |V_{IF}|^2 \ FCWD \end{aligned} \tag{6.6}$$

In the following subsections, we look at ways to calculate the FCWD.

6.2.1 Classical limit of Fermi's golden rule

Calculation of the FCWD can be simplified by considering the classical limit of Eq. 6.5. This equation, however, being quantum mechanical, considers the microscopic transition rate. For a macroscopic equivalent of this expression, a thermally equilibrated manifold of the initial vibrational states, $\{i\}$, needs to be considered [109].

$$k_{IF} = \frac{2\pi}{\hbar} |V_{IF}|^2 \frac{1}{\int e^{-E_{I\{i\}}\beta} dE_i} \int \int e^{-E_{I\{i\}}\beta} |\langle \phi_i | \phi_{\{f\}} \rangle|^2 \delta(\Delta E_{IF} + E_{\{i\}} - E_{\{f\}}) dE_f dE_i \tag{6.7}$$

where, $\beta = 1/k_BT$. In the classical limit, i.e., when $k_BT << \hbar\omega$ for all vibrational frequencies, Eq. 6.7 reduces to the Marcus expression [109],

$$k_{IF} = \frac{2\pi}{\hbar}|V_{IF}|^2 \frac{1}{\sqrt{4\pi\lambda k_BT}} e^{\frac{-\Delta G^{\ddagger}}{k_BT}} \tag{6.8}$$

where, λ is the reorganization energy and $\Delta G^{\ddagger}$ is the Gibbs free energy of the reaction. Ignoring entropy contributions [28], Eq. 6.8 reduces to

$$k_{IF} = \frac{2\pi}{\hbar}|V_{IF}|^2 \frac{1}{\sqrt{4\pi\lambda k_BT}} e^{\frac{-\Delta E^{\ddagger}}{k_BT}} \tag{6.9}$$

This is a classical interpretation of FGR, and the barrier, $\Delta E^{\ddagger}$, is the energy required for the reactant state to reach the crossing (see Figure 6.2). Unlike a quantum process, where the state transfer can take place even before the PS–O_2 reaches the crossing, within the classical regime, the state transfer can take place only after reaching the crossing.

As previously stated, Eq. 6.9 is rigorously valid when $k_BT << \hbar\omega$ for all vibrational frequencies. While modeling photosensitization, it is adequate for the mode that is responsible for the deactivation of the isolated PS, i.e., the mode along which the T_1 minimum moves to reach the MECP with the ground state, to be less than 200 cm^{-1} (this values corresponds to 1 k_BT at 298 K) [28]. This is essentially the mode along with the TT0 surface of the PS–O_2 composite system crosses with the SS2 state.

6.2.2 Time-dependent variant of Fermi's golden rule

If the classical limit of FGR is not considered, handling the delta function poses a computational difficulty. This can be handled in one of two ways: (a) the delta function can be approximated to an energy window, and all the FCFs which fall within this window can be explicitly calculated [110], or (b) the inverse Fourier transform of the delta function can be taken [111–113]. Since the delta function is a function of energy,

taking its inverse Fourier transform would convert it to the time space and therefore this becomes a time-dependent variant of FGR. Alternatively, approximating the delta function to an energy window is the time-independent variant of FGR.

In the present study, we have chosen the time-dependent variant of FGR, mainly because the time-independent variant requires the computation of FCFs at very high quantum numbers, which is computationally prohibitive. On taking the inverse Fourier transform of the delta function, we get the following form of FGR in atomic units,

$$k_{IF} = |V_{IF}|^2 \int_{-\infty}^{\infty} G(\tau) e^{i\tau(\Delta E_{IF} + E_i)} d\tau \tag{6.10}$$

where,

$$G(\tau) = \sum_{\{f\}} |\langle \phi_i | \phi_{\{f\}} \rangle|^2 e^{i\tau E_{\{f\}}} \tag{6.11}$$

Here, $G(\tau)$ is the generating function for the vibrational wavefunctions, which within the harmonic approximation are the eigenfunctions of the harmonic oscillator. Upon using Mehler's formula [114], to get a closed-form expression for this infinite sum in N dimensions, we get,

$$G(\tau) = (\sqrt{2}\pi)^{-N} (det(\mathbf{S}^{-1}\mathbf{\Omega}_I\mathbf{\Omega}_F))^{\frac{1}{2}} \int e^{-\frac{1}{4}((\mathbf{Q}_F+\bar{\mathbf{Q}}_F)^\dagger \mathbf{\Omega}_F \mathbf{B} (\mathbf{Q}_F+\bar{\mathbf{Q}}_F))} \times$$
$$e^{-\frac{1}{4}((\mathbf{Q}_F-\bar{\mathbf{Q}}_F)^\dagger \mathbf{\Omega}_F \mathbf{B}^{-1} (\mathbf{Q}_F-\bar{\mathbf{Q}}_F) + 2\mathbf{Q}_I^\dagger \mathbf{\Omega}_I \mathbf{Q}_I + 2\bar{\mathbf{Q}}_I^\dagger \mathbf{\Omega}_I \bar{\mathbf{Q}}_I)} dQ_{I_1} dQ_{I_2} \ldots dQ_{I_N} d\bar{Q}_{I_1} d\bar{Q}_{I_2} \ldots d\bar{Q}_{I_N} \tag{6.12}$$

where, $\mathbf{\Omega}_I$ is a diagonal matrix with elements $\Omega_{ii} = \omega_i$, and ω_i corresponds to the frequencies of the initial state. $\mathbf{\Omega}_F$, $\mathbf{S}$ and $\mathbf{B}$ are diagonal matrices with elements $\Omega_{ii} = \omega_i$, $S_{ii} = sinh(i\omega_i\tau)$ and $B_{ii} = tanh(i\omega_i\tau/2)$, respectively, and ω_i corresponds to the frequencies of the final state. $\mathbf{Q}_I$ and $\mathbf{Q}_F$ are column vectors composed of the mass-weighted normal mode coordinates of the initial and final states, respectively. Equation 6.12 con-

tains two sets of mass-weighted normal mode coordinates, one barred and one unbarred one, and this is a result of separating the FCF into two separate integrals. While this step may seem inscrutable, it is done for the convenience of applying Mehler's formula.

A more detailed derivation to obtain Eq. 6.12 from Eq. 6.10 can be found in the supporting information of Reference [111].

Duschinsky relation and imaginary modes

The initial and final states are approximated as harmonic oscillators, as a result of which the normal modes of the final states, $\mathbf{Q}_F$, are related to the normal modes of the initial state, $\mathbf{Q}_I$ by a Duschinsky transformation [115]:

$$\mathbf{Q}_F = \mathbf{J}\mathbf{Q}_I + \mathbf{D} \tag{6.13}$$

where, $\mathbf{J} = \mathbf{Q}_F^{\dagger}\mathbf{Q}_I$, the Duschinsky rotation matrix, is the transformation matrix between the two sets of normal modes, and $\mathbf{D} = \mathbf{Q}_F^{\dagger}(\mathbf{R}_I - \mathbf{R}_F)$, the displacement vector, is the change in the geometries ($\mathbf{R}$) between the initial and final states, written in the normal mode space of the final state. Further, the initial and final geometries need to satisfy the Eckart conditions [116], before the calculation of $\mathbf{D}$. In our work we have implemented the algorithm described in Reference [117] to fulfill the Eckart conditions.

The Duschinsky relation greatly simplifies the calculation of Eq. 6.12 which reduces to,

$$\begin{aligned} G(\tau) = (2\sqrt{2}\pi)^{-N}(det(\mathbf{S}^{-1}\mathbf{\Omega}_I\mathbf{\Omega}_F))^{\frac{1}{2}} \int e^{-\frac{1}{4}(\mathbf{X}^{\dagger}\mathbf{\Omega}_I\mathbf{X}+\mathbf{Y}^{\dagger}\mathbf{\Omega}_I\mathbf{Y})} \\ \times e^{-\frac{1}{4}(\mathbf{X}^{\dagger}\mathbf{J}^{\dagger}\mathbf{\Omega}_F\mathbf{B}\mathbf{J}\mathbf{X}+2\mathbf{X}^{\dagger}\mathbf{J}^{\dagger}(\mathbf{\Omega}_F\mathbf{B}+\mathbf{B}^{\dagger}\mathbf{\Omega}_F^{\dagger})\mathbf{D}+4\mathbf{D}^{\dagger}\mathbf{\Omega}_F\mathbf{B}\mathbf{D})} \\ \times e^{-\frac{1}{4}(\mathbf{Y}^{\dagger}\mathbf{J}^{\dagger}\mathbf{\Omega}_F\mathbf{B}^{-1}\mathbf{J}\mathbf{Y})} dX_1 \dots dX_N d_1 \dots dY_N \end{aligned} \tag{6.14}$$

where, $\mathbf{X} = \mathbf{Q}_I + \bar{\mathbf{Q}}_I$ and $\mathbf{X} = \mathbf{Q}_I - \bar{\mathbf{Q}}_I$. On solving the standard integrals in Eq. 6.14,

$G(\tau)$ reduces to,

$$G(\tau) = 2^{\frac{N}{2}} \sqrt{\frac{det(\mathbf{S}^{-1}\mathbf{\Omega}_I\mathbf{\Omega}_F}{det(\mathbf{J}^\dagger\mathbf{\Omega}_F\mathbf{B}\mathbf{J}+\mathbf{\Omega}_I)det(\mathbf{J}^\dagger\mathbf{\Omega}_F\mathbf{B}^{-1}\mathbf{J}+\mathbf{\Omega}_I)}} \times e^{\mathbf{D}^\dagger(\mathbf{\Omega}_F\mathbf{B}\mathbf{J}(\mathbf{J}^\dagger\mathbf{\Omega}_F\mathbf{B}\mathbf{J}+\mathbf{\Omega}_I)^{-1}\mathbf{J}^\dagger\mathbf{\Omega}_F\mathbf{B}-\mathbf{\Omega}_F\mathbf{B})\mathbf{D}} \tag{6.15}$$

Finally, the photosensitization rate is calculated by substituting the expression for $G(\tau)$ from Eq. 6.15, in Eq. 6.16, which includes a Boltzmann factor,

$$k_{IF} = e^{-E_I\beta}|V_{IF}|^2 \int_{-\infty}^{\infty} G(\tau)e^{i\tau(\Delta E_{IF}+E_i)}d\tau \tag{6.16}$$

and performing a time integration. Since the time integration of $G(\tau)e^{i\tau(\Delta E_{IF}+E_i)}$ gives the FCWD, it can be abbreviated as FCWD(τ).

To be able to exploit the simplification due to the Duschinsky transformation, we need to calculated the optimized geometries and normal modes of the initial and final states. These optimizations and normal mode calculations need to be carried out on the PS–O_2 system at several D values, for the TT0 and SS2 states which are the initial and final states, respectively. Here, a complication arises due to the fact that we need to carry out constrained optimization of the PS–O_2 complexes, with the D as the constraint. This is because the energy of the TT0 and SS2 states increase with decreasing D, and if the D is not constrained between the PS and O_2 while optimizing, they are likely to jump apart. This leads to imaginary eigenvalues along the modes that have not been optimized. While a simple solution might simply be to eliminate these modes, there are unequal number of such imaginary modes between the TT0 and SS2 states. Therefore, we have set the values of these imaginary frequencies to a low value of 100 cm^{-1}. The reasoning here is that, an imaginary mode, in general, corresponds to an unbound state. However, the assumption that all vibrational wavefunctions are stationary states is implicit in the derivation of the FCWD(τ) function [111]. Therefore, to best imitate an unbound

potential we have assigned these imaginary modes to very low frequencies of 100 cm^{-1}.

Damping factor

To calculate FCWD, a time integration of FCWD(τ) needs to be carried out, which is a complex function. Conveniently, the imaginary part of FCWD(τ) is an odd function and therefore its integral can be ignored (since the limits of integration are $-\infty$ and ∞). Further, the real part is an even function, and its integral can be taken as twice the value of the integral over positive time. The real part of the FCWD(τ) function over positive time is an oscillating function, as shown in Figure 6.5a, and we found that the function does not get damped even after 3 ps. This complicates the integration step, as we cannot

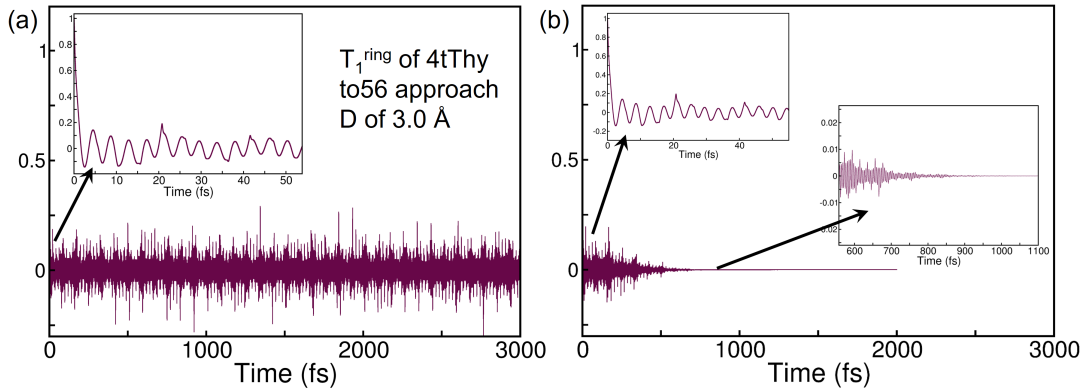

Figure 6.5: The real parts of the FCWD(τ) function without any damping factor in (a) and with a Gaussian damping factor of 0.001 cm^{-1} in (b).

determine at what τ to stop the integration. The inset of Figure 6.5a, however, suggests that the bulk of the area under the curve is within the first few oscillations and the rest of the function would simply cancel each other out. If this were true, then the value of the integral should start converging after some τ. However, we see from Table 6.1 that the value does not converge for different time intervals.

Therefore, we have chosen to damp FCWD(τ) using a Gaussian damping function [111]. The rates do not change significantly on using various damping parameters as

Table 6.1: Integral values of FCWD(τ) for different time intervals, for the three different thiothymines along select orientation directions and D values.

τ	2tThy (T_1^{ring}) Å to2X, D=2.6 Å	4tThy (T_1^{ring}) Å to56, D=3.0 Å	dtThy (T_1^{ring}) to4X, D=3.6 Å
30 fs	29.116	52.152	23.106
1 ps	6.595	51.365	32.371
2 ps	12.625	63.475	3.774
3 ps	3.678	50.379	30.902

seen in Table 6.2. We have used a damping parameter of 0.001 cm^{-1} and carried out the time integration till 2 ps, by which time, the function most certainly gets damped (Figure 6.5b). This damping factor is chosen such that the function gets damped between 1 and 2 ps. The reasoning here is that the rate calculation is carried out for a certain configuration of O_2 and the PS, at a particular D. But in the timescale of picoseconds, which is the timescale of nuclear motion, the O_2 is likely to change its position with respect to the PS. Therefore, a couple of picoseconds is all the time that the PS has to transfer its energy to the O_2 molecule. Moreover, the damping factor also accounts for any radiative damping that the system may undergo.

Table 6.2: Value of FCWD with the use of different damping parameters, along with the integration time, time taken for the function to get damped, the resulting photosensitization rate and the real time taken for the integration.

η (cm^{-1})	FCWD	k (s^{-1})	t–int[a] (fs)	t–damp[b] (fs)	t–real[c] (min)
0.01	40.489	1.6×10^6	500	350	7
0.005	38.860	1.5×10^6	2500	550	46
0.001	32.243	1.2×10^6	2500	1200	64
0.0005	29.882	1.2×10^6	3000	1700	93

[a]Integration time, [b]time after which the function gets damped, and [c]real time taken for the calculation in minutes

6.3 Orientation Directions Based on Orbital Overlap

The diabatic coupling strongly depends on the orientation of the PS with respect to O_2 as the two approach each other. Typically, the diabatic calculation would have to be performed for several orientation directions [118]. In our study, however, we have chosen orientation directions which maximize orbital overlap between the frontier orbitals of O_2 (π^*) and the PS [27]. Further, the nature of the lowest triplet state in all 3 thiothymines was found to be $\pi\pi^*$ (Chapter 4). Therefore, we have chosen three approach directions (shown in Figure 6.6), labelled as 'to56' (when O_2 approaches the C^5 and C^6 double bond in the PS), 'to2X' and 'to4X' (when O_2 approaches the carbonyl or thione at the 2nd and 4th positions, respectively). In all 3 approaches, the O_2 is kept parallel to the

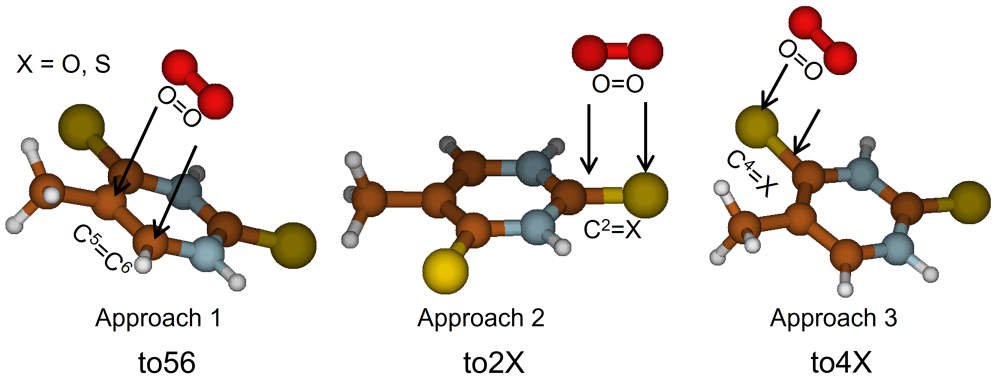

Figure 6.6: The 3 approach directions along which the diabatic coupling and rate is calculated in this study.

PS, as this maximizes orbital overlap more than if the two were either perpendicular to each other or in the same plane [27].

To obtain the diabatic coupling, the projection of the nonadiabatic coupling is taken along $\vec{D}_{to56}$, $\vec{D}_{to2X}$ and $\vec{D}_{to4X}$ vectors for the to56, to2X and to4X directions, respec-

tively, which are given by Eq. 6.17

$$\begin{aligned}\vec{D}_{to56} &= \frac{\vec{Q}^{PS}_{C5} + \vec{Q}^{PS}_{C6}}{2} - \frac{\vec{Q}_{O1} + \vec{Q}_{O2}}{2} \\ \vec{D}_{to2X} &= \frac{\vec{Q}^{PS}_{C2} + \vec{Q}^{PS}_{X2}}{2} - \frac{\vec{Q}_{O1} + \vec{Q}_{O2}}{2} \\ \vec{D}_{to4X} &= \frac{\vec{Q}^{PS}_{C4} + \vec{Q}^{PS}_{X4}}{2} - \frac{\vec{Q}_{O1} + \vec{Q}_{O2}}{2}\end{aligned} \tag{6.17}$$

where, $\vec{Q}^{PS}$ and $\vec{Q}_O$ denote the position vector of the atoms in the PS and O_2, respectively. The initial D is taken to be 3.8 Å, since the PS–O_2 energy was found to be simply additive of the energies of the PS and O_2 at this distance. The final D considered was 2.2 Å, because by this distance, the energy of the initial TT0 state increases to such an extent that the rate is all but extinguished due to the Boltzmann factor in Eq. 6.7.

6.4 Rates of Photosensitization

6.4.1 Computational Methodology

Geometry optimizations, frequency and energy calculations on the composite PS–O_2 system was carried out at the SA-CASSCF [35,36] level of theory with a state-averaging that included the first 4 singlet states. The active space consisted of 10 electrons in 8 orbitals, denoted as 10,8, of which 6,4 belonged to the O_2 and 4,4 belonged to the PS. The orbitals for O_2 included its π and π^* orbitals. For the PS, π and π^* orbitals were included such that they were involved in the transitions of the T_1 state. The 6-31G** basis set was used for all calculations. All calculations were performed using the Molpro 2012 [52,53] quantum chemical software package, and molecular orbitals were visualized using Molden [54].

6.4.2 Rates with classical limit of Fermi's golden rule

The validity of the classical limit of FGR for thiothymines is evaluated by calculating the frequency of the mode which is responsible for deactivation of the PS from its T_1 minimum to its MECP with the ground state. This has been done by expressing the difference in geometries between the MECP and T_1 minimum structures in terms of the normal modes of the T_1 minimum. Finally, the total resultant frequency of the mode is calculated as a linear combination of the frequency of each mode multiplied by the contribution of that mode. This procedure has been followed since the geometry changes between the MECP and T_1 minimum were too diverse to be assigned to any one normal mode of the T_1 minimum through visual inspection. This resultant frequency for 2tThy (T_1^{ring}), 2tThy (T_1^{pyr}), 4tThy (T_1^{ring}) and dtThy (T_1^{ring}) was calculated to be 199 cm^{-1}, 141 cm^{-1}, 379 cm^{-1} and 358 cm^{-1}, respectively. Note here, that both T_1 minima of 2tThy have been considered owing to small the energy gap between them, as was seen in Chapter 4.

Since the frequency of the deactivating mode is required to be less than 200 cm^{-1}, the calculated values suggest that this method is unsuitable for 4tThy and dtThy. Regardless, the photosensitization rates were calculated for the thiothymines. The rates for both minima of 2tThy as a function of D, for all 3 approach directions probed in this work, are shown in Figure 6.7. For 4tThy and dtThy, however, the photosensitization rates are well below 10^{-3} s^{-1}.

The relative photosensitization rates given by this method are not consistent with experimental results. $^1O_2$ yields, obtained experimentally for 2tThy, 4tThy and dtThy are 0.36, 0.42 and 0.46, respectively [14], indicating that all 3 molecules have a substantial ability to photosensitize O_2. Moreover, the rate at which molecular O_2 quenches the T_1 state of 2tThy and 4tThy is found to be $(5.1 \pm 0.1) \times 10^9$ $M^{-1}s^{-1}$ [58] and $(6.4 \pm 1.0) \times 10^9$ $M^{-1}s^{-1}$ [59], respectively. This number can be thought of as a proxy for the photosensitization rate and these values imply that 2tThy and 4tThy would have similar

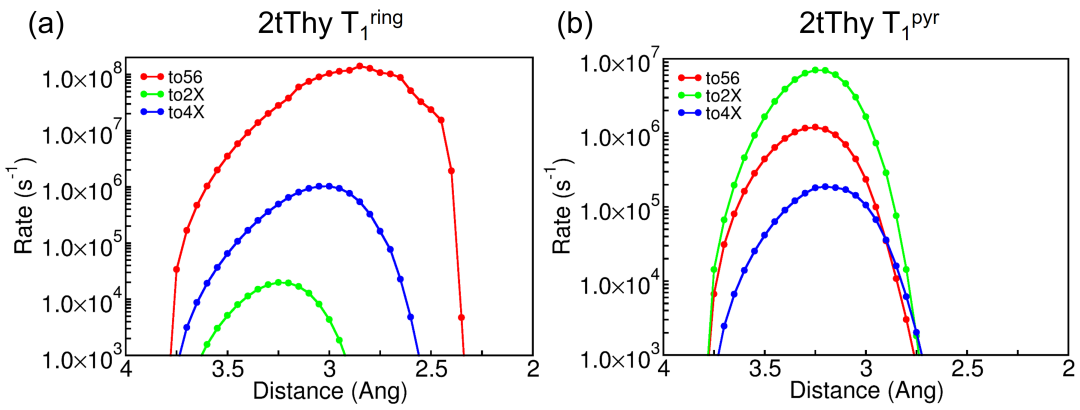

Figure 6.7: Photosensitizing rates as a function of D calculated for the (a) T_1^{ring} and (b) T_1^{pyr} minima of 2tThy, using the classical approximation of Fermi's golden rule.

photosensitization rates. Clearly, this classical treatment is inadequate and suggests the need for a better approach.

Improved calculation of barriers

The rate within the classical limit of FGR has a square dependence on the diabatic coupling and an exponential dependence on the barrier to reach the crossing (Eq. 6.9) [28]. While the calculated diabatic coupling is found to be quite similar across the thiothymines, the barrier shows significant difference. The barrier calculated in 2tThy (both conformers) is about 0.2 eV, while the barrier in 4tThy and dtThy is between 0.8 eV and 1.1 eV. The high barrier in 4tThy and dtThy essentially extinguishes any rate that may arise because of the diabatic coupling. To see if a better calculation of the barrier is possible, we have calculated the barriers explicitly from the R space i.e., for different D, we have changed the geometry in the R space along the coordinate that promotes crossing. This is computationally more expensive albeit more accurate than the procedure described in Reference [28] which uses the isolated PS, and not the composite system for the barrier calculation. An example of such a calculation is Figure 6.4, however, the purpose of Figure 6.4 was to calculate the diabatic coupling from

the R space. The barrier is calculated from Figure 6.4 as the energy difference between the starting point and the crossing point on the TT0 surface, and this is repeated for several D. Additionally, the increase in the energy of the TT0 state at that particular D, with respect to a very large D (3.8 Å), is also added to the barrier. While this is a more expensive way of getting the barriers, the failure of the currently calculated barriers to capture the experimental results, necessitates this.

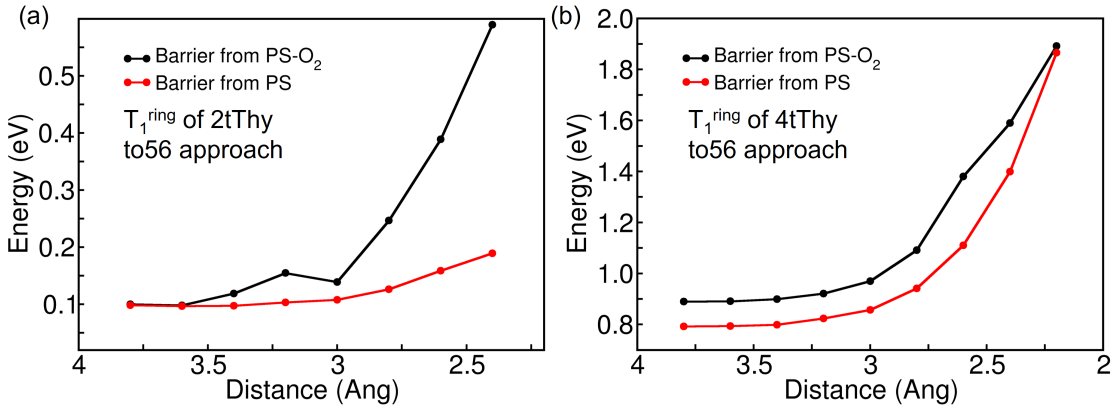

Figure 6.8: The barrier for the crossing between the TT0 and SS2 states calculated from the PS–O_2 composite system and the isolated PS is compared for the T_1^{ring} conformer of (a) 2tThy and (b) 4tThy.

The barrier calculated this way is compared with the barrier calculated using the isolated PS and is shown in Figure 6.8, for the T_1^{ring} conformer of 2tThy and 4tThy along the to56 approach direction. While obtaining barriers from the isolated PS works fairly well in the case of 4tThy, the method calculates inaccurate barriers for 2tThy. Nevertheless, the method described by Bai and Barbatti [28], is a computationally efficient method.

6.4.3 Rates with time-dependent variant of Fermi's golden rule

The photosensitization rates as a function of D, for all 3 approach directions, as calculated from the time-dependent variant of FGR, is shown in Figure 6.9. The rates are slightly lower than 10^9 s^{-1}, which is the order of magnitude for the experimental

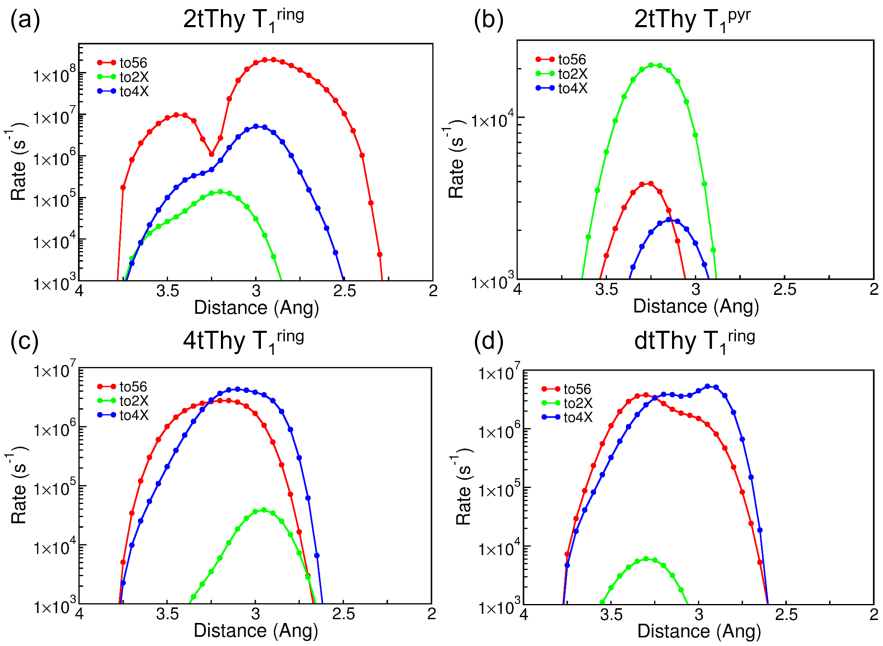

Figure 6.9: Photosensitizing rates as a function of D calculated for both T_1 minima of 2tThy, T_1^{ring} in (a) and T_1^{pyr} in (b), and the T_1^{ring} minimum of 4tThy in (c) and dtThy in (d), using the time-dependent variant of Fermi's golden rule.

rate at which molecular oxygen quenches the triplet states of 2tThy and 4tThy [58, 59]. However, these experimental quenching rates are calculated in solvent (acetonitrile) at high concentrations of O_2, while the rates modelled in this study is between 1 PS and 1 O_2 molecule, in the gas phase. The success of this method, however, lies in the fact that the relative photosensitization rates for the T_1^{ring} minimum of all three thiothymines, correctly depict experimental observations. In the following section, we use the results from this method to get physical insights into the process of photosensitization.

6.5 Mechanistic Insights into Photosensitization

The diabatic coupling, which is a key component in the rate calculation, increases as the PS and O_2 come close together. It is also strongly dependent on the overlap between the π^* orbitals of O_2 and the PS. The diabatic couplings, as a function of D are shown

in Figure 6.10, and the numbers in the plot correspond to the diabatic coupling values at the smallest D considered (2.2 Å). The orbitals which define the nature of the T_1 minimum of the thiothymines are also shown alongside.

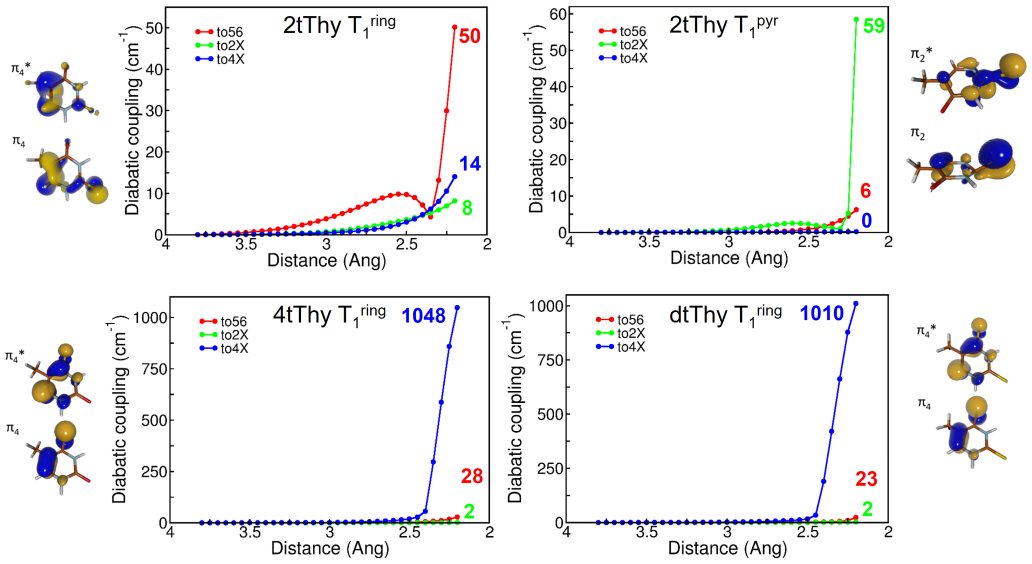

Figure 6.10: Diabatic couplings plotted as a function of D for both T_1 minima of 2tThy and the T_1^{ring} minimum of 4tThy and dtThy, for all 3 approach directions. The numbers indicated within the plots correspond to the diabatic coupling at the smallest D considered (2.2 Å). The orbitals involved in the respective T_1 minima are shown alongside the plots.

The direct relation between the diabatic coupling and molecular overlap is clearly illustrated in all cases. The T_1^{ring} minimum in all 3 thiothymines have very little diabatic coupling along the to2X direction and this can be directly correlated with the little to no electron density over the C^2=X region in all these molecules. Also, the only conformer to have significant electron density along this region (T_1^{pyr} of 2tThy) is accordingly seen to have the highest diabatic coupling along the to2X direction. In the T_1^{ring} minimum orbitals of all 3 thiothymines, 4tThy and dtThy have significant electron density along the C^4=S bond, while 2tThy only has density along the C^5=C^6 bond. This is manifested in the highest diabatic coupling being present along the to4X direction in 4tThy and dtThy and along the to56 direction in 2tThy. Overall, the highest coupling in 4tThy and

dtThy (along to4X) is about 2 orders of magnitude higher than the highest coupling in 2tThy (along to56), and this trend can also be tied back to the extent of orbital overlap. In 4tThy and dtThy, the π^* orbitals of O_2 overlap with π^* orbitals which involve the larger S atom as opposed to the smaller O in 2tThy. While one can argue that the S atom is involved in the T_1^{pyr} of 2tThy, which also has a coupling of the same order as the T_1^{ring} of 2tThy, this is likely because the C^2=S bond here is weaker due to strong pyramidalization.

The highest photosensitization rate is of the order of 10^8 s^{-1} in 2tThy (T_1^{ring}) and 10^7 s^{-1} in 4tThy and dtThy (Figure 6.9). Diabatic coupling values however (Figure 6.7) suggest that the rate should be higher in 4tThy and dtThy. However, while the rates (Eq. 6.7) have a square dependence on the diabatic coupling, the Boltzmann factor can quench the rate with an exponential scaling. The Boltzmann factor as a function of D, along all 3 orientation directions, for all the thiothymines is shown in Figure 6.11. The

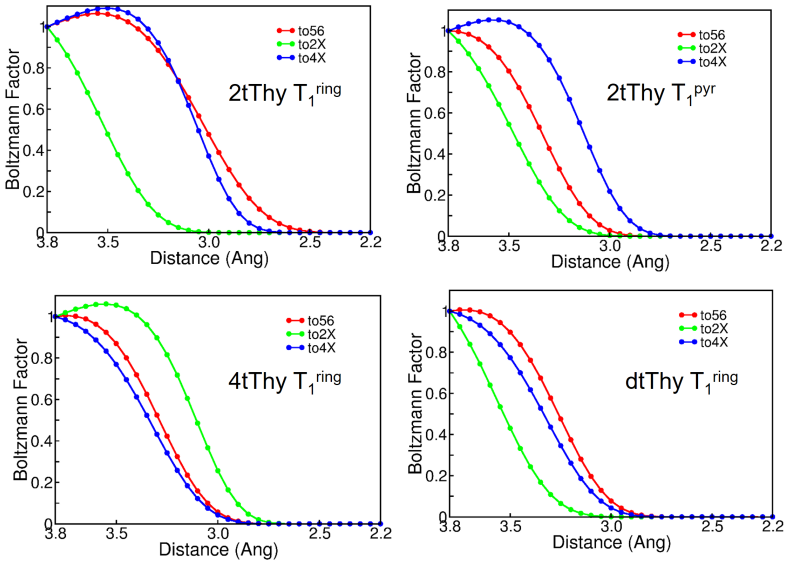

Figure 6.11: Boltzmann factors plotted as a function of D for both T_1 minima of 2tThy and the T_1^{ring} minimum of 4tThy and dtThy, for all 3 approach directions.

Boltzmann factor falls off faster in 4tThy and dtThy as compared to 2tThy. Interestingly,

this is for the same reason that the diabatic coupling in 4tThy and dtThy was higher than in 2tThy: as the O_2 approaches a double bond which involves the S atom, the steric hindrance is greater than if O_2 were approaching a double bond which involved the O atom, due to the greater size of S. This is also clearly illustrated in Figure 6.11 when we see that the approach direction that results in the Boltzmann factor falling the fastest in 2tThy and 4tThy is to2X and to4X – the double bonds with the S atom. By this reasoning, we would expect the to56 direction to be equivalent in all cases, however, we see that it decays comparatively slowly in the T_1^{ring} minimum of 2tThy. This is certainly a contributor to the high photosensitization rate of 2tThy (T_1^{ring}) along the to56 approach, but we have been unable to identify its origin.

The photosensitization rate in all molecules and all 3 approach directions increases as the PS and O_2 come close, reaches a maximum value, and then starts to fall off as the D decreases even further (Figure 6.9). This is also true when the classical approximation of FGR is used (Figure 6.7). The initial increase in rate is due to the increase in the diabatic coupling. The falling off of the rate at small D is due to the repulsive nature of the interactions between PS and O_2. This was already seen schematically in Figure 6.3, and in Figure 6.12, the actual energies of the states are shown for the dtThy-O_2 composite system, along the 2X approach direction. Over a span of 1.6 Å, the energy of the reactant state (purple state in Figure 6.12) increases by about 2.4 eV. As this energy increases, the Boltzmann factor attached along with the rate (Eq. 6.7) very quickly quenches the rate that may result from the strong coupling at this D.

While the increase in energy is expected at small D, it is surprising that there are no stabilizing forces as the electron clouds of O_2 and PS interact at intermediate D. This is because these energies have been calculated at the CASSCF level which does not account for London dispersion forces. However, using CASPT2 would have been very expensive for such a large system, especially since different approach directions need to be considered. To illustrate this, we have calculated the energy of the ground

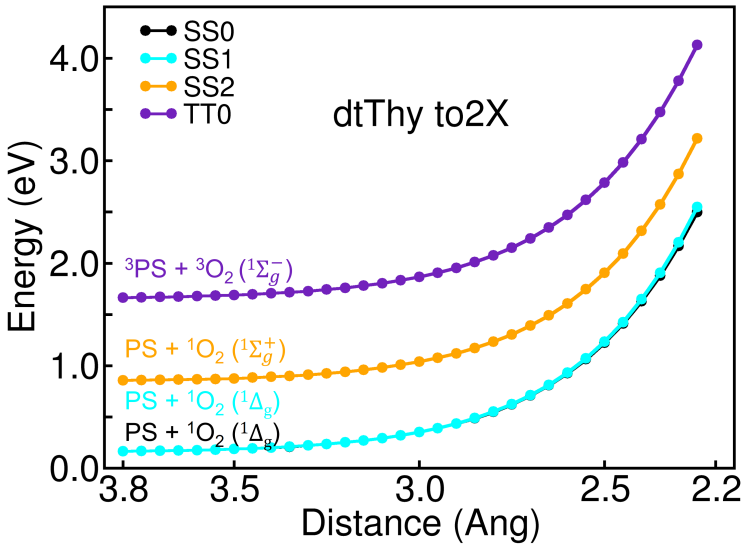

Figure 6.12: Calculated energies of the first 4 singlet states, 3 of which are of SS nature and the other is of TT nature, for the dtThy–O_2 composite system, along the to2X approach direction, for decreasing values of D. The first two states, SS0 and SS1 are degenerate through most of the D values.

state, which in this case is the SS0 state at HF (does not account for dispersion forces [119]) and MP2 levels of theory (accounts for dispersion forces) as shown in Figure 6.13 for one representative case (T_1^{ring} of dtThy along the to2X approach; the same system the one in Figure 6.12). We see clearly that the HF energies increase right from the beginning, while the MP2 energies initially get stabilized before they start increasing. The stabilization at MP2 level of theory however, is very small and there would not be a significant change in the rates currently calculated, even if the more expensive CASPT2 method was used.

This study illustrates that even within the thiothymine series, there is enough electronic variation that the classical limit of FGR which worked well for 2tThy, no longer gives physically meaningful results for 4tThy and dtThy. The classical limit of FGR, however, is not without its uses, being a computationally efficient method which does not require optimization and frequency calculations of the PS–O_2 composite system [28,118]. The system however needs to be carefully evaluated before this variant of FGR can be

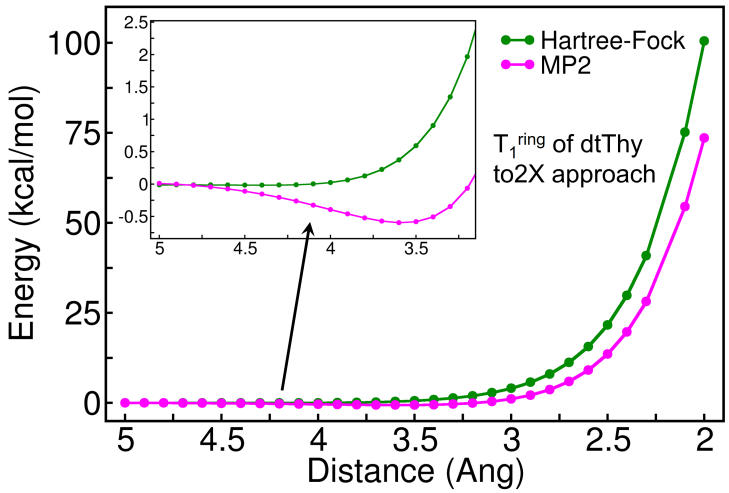

Figure 6.13: Hartree-Fock and MP2 energies in the D space for the T_1^{ring} conformer of dtThy along the to2X approach. While the Hartree-Fock energies increase even at large D, MP2 energies initially get stabilized due to dispersion forces before increasing at smaller D.

used.

To the best of our knowledge, this is the first time that the time-dependent variant of FGR, which has previously been used for internal conversion [120–123] and intersystem crossing [87, 111] rates, has been used in the case of a bimolecular nonradiative energy transfer process.

List of Publications

Publications included in this thesis

1. Manae, M. A. and Hazra, A. "Interplay between Conjugation and Size-Driven Delocalization Leads to Characteristic Properties of Substituted Thymines" *J. Phys. Chem. A,* **2017,** *121,* 8147–8153.

2. Manae, M. A. and Hazra, A. "Triplet Decay Dynamics in Sulfur Substituted Thymine: How Position of Substitution Matters" *DOI:10.1021/acs.jpca.9b08214*

3. Manae, M. A. and Hazra, A. "How Thiothymines Generate Singlet Oxygen Through Photosensitization" *Manuscript under preparation*

Publications not included in this thesis

1. Manae, M. A. and Hazra, A. "Helping Students Understand the Role of Symmetry in Chemistry Using the Particle-in-a-Box Model" *J. Chem. Educ.,* **2016,** *93,* 1056–1060.

2. Pal, S.; Manae, M. A.; Khade, V. V. and Khan, S. "Reactivity of N-heterocyclic carbene, 1,3-bis(2,6-diisopropylphenyl)imidazol-2-ylidene, towards heavier halogens (Br_2 and I_2)" *J. Indian Chem. Soc.,* **2018,** *95,* 765–770.

3. Manae, M. A. and Hazra, A. "Graphical Representation of Hydrogenic Orbitals: Incorporating Both Radial and Angular Parts of the Wave Function" *J. Chem. Educ.,* **2019,** *96,* 187–190.

Title: Interplay between Conjugation and Size-Driven Delocalization Leads to Characteristic Properties of Substituted Thymines

Author: Meghna A. Manae, Anirban Hazra

Publication: The Journal of Physical Chemistry A

Publisher: American Chemical Society

Date: Oct 1, 2017

PERMISSION/LICENSE IS GRANTED FOR YOUR ORDER AT NO CHARGE

This type of permission/license, instead of the standard Terms & Conditions, is sent to you because no fee is being charged for your order. Please note the following:

- Permission is granted for your request in both print and electronic formats, and translations.
- If figures and/or tables were requested, they may be adapted or used in part.
- Please print this page for your records and send a copy of it to your publisher/graduate school.
- Appropriate credit for the requested material should be given as follows: "Reprinted (adapted) with permission from (COMPLETE REFERENCE CITATION). Copyright (YEAR) American Chemical Society." Insert appropriate information in place of the capitalized words.
- One-time permission is granted only for the use specified in your request. No additional uses are granted (such as derivative works or other editions). For any other uses, please submit a new request.

BACK CLOSE WINDOW

References

[1] Manindar Kaur, Abdur Rob, Julianne Caton-Williams, and Zhen Huang. Biochemistry of nucleic acids functionalized with sulfur, selenium, and tellurium: roles of the single-atom substitution. In *Biochalcogen Chemistry: The Biological Chemistry of Sulfur, Selenium, and Tellurium*, pages 89–126. ACS Publications, 2013.

[2] Wei-Mei Ching, Birgit Alzner-DeWeerd, and Thressa C Stadtman. A selenium-containing nucleoside at the first position of the anticodon in selenotrnaglu from clostridium sticklandii. *Proceedings of the National Academy of Sciences*, 82(2):347–350, 1985.

[3] Thressa C Stadtman. Specific occurrence of selenium in enzymes and amino acid trnas. *The FASEB journal*, 1(5):375–379, 1987.

[4] P Ajitkumar and Joseph D Cherayil. Thionucleosides in transfer ribonucleic acid: diversity, structure, biosynthesis, and function. *Microbiological reviews*, 52(1):103, 1988.

[5] N Connor Payne, Andrew Geissler, Aileen Button, Alexandru R Sasuclark, Alayne L Schroll, Erik L Ruggles, Vadim N Gladyshev, and Robert J Hondal. Comparison of the redox chemistry of sulfur-and selenium-containing analogs of uracil. *Free Radical Biology and Medicine*, 104:249–261, 2017.

[6] Gertrude B Elion. The purine path to chemotherapy. *Science*, 244(4900):41–47, 1989.

[7] Anna L Taylor, Christopher JE Watson, and J Andrew Bradley. Immunosuppressive agents in solid organ transplantation: Mechanisms of action and therapeutic efficacy. *Critical reviews in oncology/hematology*, 56(1):23–46, 2005.

[8] David S Cooper. Antithyroid drugs. *New England Journal of Medicine*, 352(9):905–917, 2005.

[9] Brennan Ashwood, Marvin Pollum, and Carlos E Crespo-Hernández. Photochemical and photodynamical properties of sulfur-substituted nucleic acid bases. *Photochemistry and photobiology*, 95(1):33–58, 2019.

[10] Serra Arslancan, Lara Martínez-Fernández, and Inés Corral. Photophysics and photochemistry of canonical nucleobases' thioanalogs: From quantum mechanical studies to time resolved experiments. *Molecules*, 22(6):998, 2017.

[11] Takenori Yamada and Hideo Fukutome. Vacuum ultraviolet absorption spectra of sublimed films of nucleic acid bases. *Biopolymers: Original Research on Biomolecules*, 6(1):43–54, 1968.

[12] R Abouaf, J Pommier, and H Dunet. Electronic and vibrational excitation in gas phase thymine and 5-bromouracil by electron impact. *Chemical physics letters*, 381(3-4):486–494, 2003.

[13] Leigh B Clark, Gary G Peschel, and Ignacio Tinoco Jr. Vapor spectra and heats of vaporization of some purine and pyrimidine bases1. *The Journal of Physical Chemistry*, 69(10):3615–3618, 1965.

[14] Marvin Pollum, Steffen Jockusch, and Carlos E. Crespo-Hernández. 2,4-dithiothymine as a potent uva chemotherapeutic agent. *J. Am. Chem. Soc.*, 136(52):17930–17933, 2014. PMID: 25506742.

[15] Marvin Pollum, Steffen Jockusch, and Carlos E Crespo-Hernández. Increase in the photoreactivity of uracil derivatives by doubling thionation. *Physical Chemistry Chemical Physics*, 17(41):27851–27861, 2015.

[16] Carlos E Crespo-Hernández, Boiko Cohen, Patrick M Hare, and Bern Kohler. Ultrafast excited-state dynamics in nucleic acids. *Chemical reviews*, 104(4):1977–2020, 2004.

[17] Chris T Middleton, Kimberly de La Harpe, Charlene Su, Yu Kay Law, Carlos E Crespo-Hernández, and Bern Kohler. Dna excited-state dynamics: from single bases to the double helix. *Annual review of physical chemistry*, 60:217–239, 2009.

[18] Bhaskar G Maiya. Photodynamic therapy - old and new photosensitizers. *Resonance*, 5(06):15–29, 2000.

[19] Georg T Wondrak, Myron K Jacobson, and Elaine L Jacobson. Endogenous uva-photosensitizers: mediators of skin photodamage and novel targets for skin photoprotection. *Photochemical and photobiological sciences*, 5(2):215–237, 2006.

[20] T Takemura, N Ohta, S Nakajima, and I Sakata. Critical importance of the triplet lifetime of photosensitizer in photodynamic therapy of tumor. *Photochemistry and photobiology*, 50(3):339–344, 1989.

[21] Thomas J Dougherty, Charles J Gomer, Barbara W Henderson, Giulio Jori, David Kessel, Mladen Korbelik, Johan Moan, and Qian Peng. Photodynamic

therapy. *JNCI: Journal of the national cancer institute*, 90(12):889–905, 1998.

[22] W.D. James, T.G. Berger, and D.M. Elston. *Andrews' Diseases of the Skin: Clinical Dermatology*. Saunders Elsevier, 2006.

[23] Dennis EJGJ Dolmans, Dai Fukumura, and Rakesh K Jain. Photodynamic therapy for cancer. *Nature reviews cancer*, 3(5):380, 2003.

[24] Barbara W Henderson and Thomas J Dougherty. How does photodynamic therapy work? *Photochemistry and photobiology*, 55(1):145–157, 1992.

[25] Mario Barbatti, Adélia JA Aquino, Jaroslaw J Szymczak, Dana Nachtigallová, Pavel Hobza, and Hans Lischka. Relaxation mechanisms of uv-photoexcited dna and rna nucleobases. *Proceedings of the National Academy of Sciences*, 107(50):21453–21458, 2010.

[26] Christel M Marian. Spin–orbit coupling and intersystem crossing in molecules. *Wiley Interdisciplinary Reviews: Computational Molecular Science*, 2(2):187–203, 2012.

[27] Juan José Serrano-Pérez, Gloria Olaso-Gonzalez, Manuela Merchan, and Luis Serrano-Andres. Singlet oxygen generation in puva therapy studied using electronic structure calculations. *Chemical Physics*, 360(1-3):85–96, 2009.

[28] Shuming Bai and Mario Barbatti. Divide-to-conquer: A kinetic model for singlet oxygen photosensitization. *Journal of chemical theory and computation*, 13(11):5528–5538, 2017.

[29] A. Szabo and N.S. Ostlund. *Modern Quantum Chemistry: Introduction to Advanced Electronic Structure Theory*. Dover Books on Chemistry. Dover Publications, 1996.

[30] T. Helgaker, P. Jorgensen, and J. Olsen. *Molecular Electronic-structure Theory*. Wiley, 2008.

[31] C. Cohen-Tannoudji, B. Diu, and F. Laloė. *Quantum mechanics. 2*. Textbook physics. John Wiley and Sons, 1977.

[32] J. Leszczynski. *Handbook of Computational Chemistry*. Handbook of Computational Chemistry. Springer, 2012.

[33] Edwin E Salpeter. *Quantum Mechanics of One-and Two-Electron Atoms*. Plenum Press, 1977.

[34] Andreas Berning, Marcus Schweizer, Hans-Joachim Werner, Peter J Knowles, and Paolo Palmieri. Spin-orbit matrix elements for internally contracted multireference configuration interaction wavefunctions. *Molecular Physics*, 98(21):1823–1833, 2000.

[35] Peter J Knowles and Hans-Joachim Werner. An efficient second-order mc scf method for long configuration expansions. *Chemical physics letters*, 115(3):259–267, 1985.

[36] Hans-Joachim Werner and Peter J Knowles. A second order multiconfiguration scf procedure with optimum convergence. *The Journal of chemical physics*, 82(11):5053–5063, 1985.

[37] Chr Møller and Milton S Plesset. Note on an approximation treatment for many-electron systems. *Physical review*, 46(7):618, 1934.

[38] Paolo Celani and Hans-Joachim Werner. Multireference perturbation theory for large restricted and selected active space reference wave functions. *The Journal of Chemical Physics*, 112(13):5546–5557, 2000.

[39] Björn O Roos, Kerstin Andersson, Markus P Fülscher, Per-åke Malmqvist, Luis Serrano-Andrés, Kristin Pierloot, and Manuela Merchán. Multiconfigurational perturbation theory: Applications in electronic spectroscopy. *Advances in chemical physics: new methods in computational quantum mechanics*, 93:219–331, 1996.

[40] James Finley, Per-Åke Malmqvist, Björn O Roos, and Luis Serrano-Andrés. The multi-state caspt2 method. *Chemical physics letters*, 288(2-4):299–306, 1998.

[41] Paul Adrien Maurice Dirac. The quantum theory of the emission and absorption of radiation. *Proceedings of the Royal Society of London. Series A, Containing Papers of a Mathematical and Physical Character*, 114(767):243–265, 1927.

[42] Meghna A Manae and Anirban Hazra. Interplay between conjugation and size-driven delocalization leads to characteristic properties of substituted thymines. *The Journal of Physical Chemistry A*, 121(42):8147–8153, 2017.

[43] Shuming Bai and Mario Barbatti. Why replacing different oxygens of thymine with sulfur causes distinct absorption and intersystem crossing. *The Journal of Physical Chemistry A*, 120(32):6342–6350, 2016.

[44] J. Clayden, N. Greeves, and S. Warren. *Organic Chemistry*. OUP Oxford, 2012.

[45] Björn O Roos and Kerstin Andersson. Multiconfigurational perturbation theory with level shift—the cr2 potential revisited. *Chemical physics letters*, 245(2-3):215–223, 1995.

[46] Ove Christiansen, Henrik Koch, and Poul Jörgensen. Perturbative triple excitation corrections to coupled cluster singles and doubles excitation energies. *The Journal of chemical physics*, 105(4):1451–1459, 1996.

[47] Thom H Dunning Jr. Gaussian basis sets for use in correlated molecular calculations. i. the atoms boron through neon and hydrogen. *The Journal of chemical physics*, 90(2):1007–1023, 1989.

[48] David E Woon and Thom H Dunning Jr. Gaussian basis sets for use in correlated molecular calculations. iii. the atoms aluminum through argon. *The Journal of chemical physics*, 98(2):1358–1371, 1993.

[49] Angela K Wilson, David E Woon, Kirk A Peterson, and Thom H Dunning Jr. Gaussian basis sets for use in correlated molecular calculations. ix. the atoms gallium through krypton. *The Journal of chemical physics*, 110(16):7667–7676, 1999.

[50] David Feller. The role of databases in support of computational chemistry calculations. *Journal of computational chemistry*, 17(13):1571–1586, 1996.

[51] Kirk A Peterson, Detlev Figgen, Erich Goll, Hermann Stoll, and Michael Dolg. Systematically convergent basis sets with relativistic pseudopotentials. ii. small-core pseudopotentials and correlation consistent basis sets for the post-d group 16–18 elements. *The Journal of chemical physics*, 119(21):11113–11123, 2003.

[52] Hans-Joachim Werner, Peter J Knowles, Gerald Knizia, Frederick R Manby, and Martin Schütz. Molpro: a general-purpose quantum chemistry program package. *Wiley Interdisciplinary Reviews: Computational Molecular Science*, 2(2):242–253, 2012.

[53] H-J Werner, PJ Knowles, G Knizia, FR Manby, M Schütz, P Celani, T Korona, R Lindh, A Mitrushenkov, G Rauhut, et al. Molpro, version 2012.1, a package of ab initio programs. *See http://www. molpro. net*, 2012.

[54] Gijs Schaftenaar and Jan H Noordik. Molden: a pre-and post-processing program for molecular and electronic structures. *Journal of computer-aided molecular design*, 14(2):123–134, 2000.

[55] Gunther Zechmann and Mario Barbatti. Photophysics and deactivation pathways of thymine. *The Journal of Physical Chemistry A*, 112(36):8273–8279, 2008.

[56] A. Bondi. van der waals volumes and radii. *The Journal of physical chemistry*, 68(3):441–451, 1964.

[57] R Abouaf, J Pommier, and H Dunet. Electronic and vibrational excitation in gas phase thymine and 5-bromouracil by electron impact. *Chemical physics letters*, 381(3-4):486–494, 2003.

[58] Hikaru Kuramochi, Takashi Kobayashi, Tadashi Suzuki, and Teijiro Ichimura. Excited-state dynamics of 6-aza-2-thiothymine and 2-thiothymine: Highly efficient intersystem crossing and singlet oxygen photosensitization. *J. Phys. Chem. B*, 114(26):8782–8789, 2010. PMID: 20552955.

[59] Yosuke Harada, Tadashi Suzuki, Teijiro Ichimura, and Yao-Zhong Xu. Triplet formation of 4-thiothymidine and its photosensitization to oxygen

studied by time-resolved thermal lensing technique. *J. Phys. Chem. B*, 111(19):5518–5524, 2007. PMID: 17439266.

[60] Serhiy Perun, Andrzej L Sobolewski, and Wolfgang Domcke. Conical intersections in thymine. *The Journal of Physical Chemistry A*, 110(49):13238–13244, 2006.

[61] Juan José Serrano-Pérez, Remedios Gonzalez-Luque, Manuela Merchan, and Luis Serrano-Andres. On the intrinsic population of the lowest triplet state of thymine. *The Journal of Physical Chemistry B*, 111(41):11880–11883, 2007.

[62] Huiyan Sun, Sibo Jiang, Julianne Caton-Williams, Hehua Liu, and Zhen Huang. 2-selenouridine triphosphate synthesis and se-rna transcription. *Rna*, 19(9):1309–1314, 2013.

[63] Julianne Caton-Williams and Zhen Huang. Synthesis and dna-polymerase incorporation of colored 4-selenothymidine triphosphate for polymerase recognition and dna visualization. *Angewandte Chemie International Edition*, 47(9):1723–1725, 2008.

[64] D.A. McQuarrie. *Quantum Chemistry*. University Science Books, 2008.

[65] P.W. Atkins and R.S. Friedman. *Molecular Quantum Mechanics*. OUP Oxford, 2011.

[66] I.N. Levine. *Quantum Chemistry*. Pearson Prentice Hall, 2009.

[67] Beatriz Cordero, Verónica Gómez, Ana E Platero-Prats, Marc Revés, Jorge Echeverría, Eduard Cremades, Flavia Barragán, and Santiago Alvarez. Covalent radii revisited. *Dalton Transactions*, 21:2832–2838, 2008.

[68] FJ Lopez, L Arias, R Chan, DE Clarke, TR Elworthy, APDW Ford, A Guzman, S Jaime-Figueroa, JR Jasper, DJ Morgans Jr, et al. Synthesis, pharmacology and pharmacokinetics of 3-(4-aryl-piperazin-1-ylalkyl)-uracils as uroselective α1a-antagonists. *Bioorganic and medicinal chemistry letters*, 13(11):1873–1878, 2003.

[69] Toshio Itahara, Yukiko Fujii, and Miki Tada. Oxidation of thymines by peroxosulfate ions in water. *The Journal of Organic Chemistry*, 53(15):3421–3424, 1988.

[70] Rakesh Kumar. 5-bromo (or chloro)-6-azido-5, 6-dihydro-2-deoxyuridine and-thymidine derivatives with potent antiviral activity. *Bioorganic and medicinal chemistry letters*, 12(3):275–278, 2002.

[71] Christian Reichardt and Carlos E Crespo-Hernández. Ultrafast spin crossover in 4-thiothymidine in an ionic liquid. *Chemical Communications*, 46(32):5963–5965, 2010.

[72] Christian Reichardt and Carlos E Crespo-Hernández. Room-temperature phosphorescence of the dna monomer analogue 4-thiothymidine in aqueous solutions after uva excitation. *The Journal of Physical Chemistry Letters*, 1(15):2239–2243, 2010.

[73] Yosuke Harada, Chie Okabe, Takashi Kobayashi, Tadashi Suzuki, Teijiro Ichimura, Nobuyuki Nishi, and Yao-Zhong Xu. Ultrafast intersystem crossing of 4-thiothymidine in aqueous solution. *The Journal of Physical Chemistry Letters*, 1(2):480–484, 2009.

[74] Bin-Bin Xie, Qian Wang, Wei-Wei Guo, and Ganglong Cui. The excited-state decay mechanism of 2, 4-dithiothymine in the gas phase, microsolvated

surroundings, and aqueous solution. *Physical Chemistry Chemical Physics*, 19(11):7689–7698, 2017.

[75] Sebastian Mai, Philipp Marquetand, and Leticia Gonzalez. Intersystem crossing pathways in the noncanonical nucleobase 2-thiouracil: A time-dependent picture. *The journal of physical chemistry letters*, 7(11):1978–1983, 2016.

[76] Lara Martínez-Fernández, Giovanni Granucci, Marvin Pollum, Carlos E Crespo-Hernández, Maurizio Persico, and Inés Corral. Decoding the molecular basis for the population mechanism of the triplet phototoxic precursors in uva light-activated pyrimidine anticancer drugs. *Chemistry–A European Journal*, 23(11):2619–2627, 2017.

[77] Ganglong Cui and Walter Thiel. Intersystem crossing enables 4-thiothymidine to act as a photosensitizer in photodynamic therapy: an ab initio qm/mm study. *The journal of physical chemistry letters*, 5(15):2682–2687, 2014.

[78] Ganglong Cui and Wei-hai Fang. State-specific heavy-atom effect on intersystem crossing processes in 2-thiothymine: A potential photodynamic therapy photosensitizer. *The Journal of chemical physics*, 138(4):044315, 2013.

[79] Marvin Pollum and Carlos E. Crespo-Hernández. Communication: The dark singlet state as a doorway state in the ultrafast and efficient intersystem crossing dynamics in 2-thiothymine and 2-thiouracil. *The Journal of Chemical Physics*, 140(7):071101, 2014.

[80] Katarzyna Taras-Goślińska, Gotard Burdziński, and Grażyna Wenska. Relaxation of the t1 excited state of 2-thiothymine, its riboside and

deoxyriboside-enhanced nonradiative decay rate induced by sugar substituent. *Journal of Photochemistry and Photobiology A: Chemistry*, 275:89–95, 2014.

[81] Katarzyna Taras-Goślińska, Grażyna Wenska, Bohdan Skalski, Andrzej Maciejewski, Gotard Burdziński, and Jerzy Karolczak. Intra-and intermolecular electronic relaxation of the second excited singlet and the lowest excited triplet states of 1, 3-dimethyl-4-thiouracil in solution. *Photochemistry and photobiology*, 75(5):448–456, 2002.

[82] Grazyna Wenska, Katarzyna Taras-Goślińska, Adam Łukaszewicz, Gotard Burdziński, Jacek Koput, and Andrzej Maciejewski. Mechanism and dynamics of intramolecular triplet state decay of 1-propyl-4-thiouracil and its α-methyl-substituted derivatives studied in perfluoro-1, 3-dimethylcyclohexane. *Photochemical and Photobiological Sciences*, 10(8):1294–1302, 2011.

[83] Victoria Vendrell-Criado, Jose A Sáez, Virginie Lhiaubet-Vallet, M Consuelo Cuquerella, and Miguel A Miranda. Photophysical properties of 5-substituted 2-thiopyrimidines. *Photochemical and Photobiological Sciences*, 12(8):1460–1465, 2013.

[84] Shuming Bai and Mario Barbatti. On the decay of the triplet state of thionucleobases. *Physical Chemistry Chemical Physics*, 19(20):12674–12682, 2017.

[85] José A Sánchez-Rodríguez, Abed Mohamadzade, Sebastian Mai, Brennan Ashwood, Marvin Pollum, Philipp Marquetand, Leticia González, Carlos E Crespo-Hernández, and Susanne Ullrich. 2-thiouracil intersystem crossing photodynamics studied by wavelength-dependent photoelectron and

transient absorption spectroscopies. *Physical Chemistry Chemical Physics*, 19(30):19756–19766, 2017.

[86] Daisuke Koyama, Matthew J Milner, and Andrew J Orr-Ewing. Evidence for a double well in the first triplet excited state of 2-thiouracil. *The Journal of Physical Chemistry B*, 121(39):9274–9280, 2017.

[87] Thomas J Penfold, Etienne Gindensperger, Chantal Daniel, and Christel M Marian. Spin-vibronic mechanism for intersystem crossing. *Chemical reviews*, 118(15):6975–7025, 2018.

[88] MA El-Sayed. Spin-orbit coupling and the radiationless processes in nitrogen heterocyclics. *The Journal of Chemical Physics*, 38(12):2834–2838, 1963.

[89] Abed Mohamadzade, Shuming Bai, Mario Barbatti, and Susanne Ullrich. Intersystem crossing dynamics in singly substituted thiouracil studied by time-resolved photoelectron spectroscopy: Micro-environmental effects due to sulfur position. *Chemical Physics*, 515:572–579, 2018.

[90] Roberto Improta, Fabrizio Santoro, and Lluis Blancafort. Quantum mechanical studies on the photophysics and the photochemistry of nucleic acids and nucleobases. *Chemical reviews*, 116(6):3540–3593, 2016.

[91] Hui Yu, Jose A Sanchez-Rodriguez, Marvin Pollum, Carlos E Crespo-Hernández, Sebastian Mai, Philipp Marquetand, Leticia González, and Susanne Ullrich. Internal conversion and intersystem crossing pathways in uv excited, isolated uracils and their implications in prebiotic chemistry. *Physical Chemistry Chemical Physics*, 18(30):20168–20176, 2016.

[92] Olivier Reelfs, Peter Karran, and Antony R Young. 4-thiothymidine sensitization of dna to uva offers potential for a novel photochemotherapy. *Photochemical and Photobiological Sciences*, 11(1):148–154, 2012.

[93] Emilios Gemenetzidis, Oksana Shavorskaya, Yao-Zhong Xu, and Giuseppe Trigiante. Topical 4-thiothymidine is a viable photosensitiser for the photodynamic therapy of skin malignancies. *Journal of Dermatological Treatment*, 24(3):209–214, 2013.

[94] Marvin Pollum, Minh Lam, Steffen Jockusch, and Carlos E Crespo-Hernández. Dithionated nucleobases as effective photodynamic agents against human epidermoid carcinoma cells. *ChemMedChem*, 13(10):1044–1050, 2018.

[95] Adel El Azhary, Guntram Rauhut, Peter Pulay, and Hans-Joachim Werner. Analytical energy gradients for local second-order møller–plesset perturbation theory. *The Journal of chemical physics*, 108(13):5185–5193, 1998.

[96] H Weiler-Feilchenfeld and Z Neiman. Dipole moments and electronic structure of some xanthine and thioxanthine derivatives. *Journal of the Chemical Society B: Physical Organic*, pages 596–598, 1970.

[97] John D Nguyen, Erica M D'amato, Jagan MR Narayanam, and Corey RJ Stephenson. Engaging unactivated alkyl, alkenyl and aryl iodides in visible-light-mediated free radical reactions. *Nature Chemistry*, 4(10):854, 2012.

[98] Joseph W Tucker and Corey RJ Stephenson. Shining light on photoredox catalysis: theory and synthetic applications. *The Journal of organic chemistry*, 77(4):1617–1622, 2012.

[99] Shunichi Fukuzumi and Kei Ohkubo. Selective photocatalytic reactions with organic photocatalysts. *Chemical Science*, 4(2):561–574, 2013.

[100] Jun Xuan and Wen-Jing Xiao. Visible-light photoredox catalysis. *Angewandte Chemie International Edition*, 51(28):6828–6838, 2012.

[101] Davide Ravelli, Maurizio Fagnoni, and Angelo Albini. Photoorganocatalysis: What for? *Chemical Society Reviews*, 42(1):97–113, 2013.

[102] Yuen Yap Cheng, Burkhard Fückel, Rowan W MacQueen, Tony Khoury, Raphaël GCR Clady, Tim F Schulze, NJ Ekins-Daukes, Maxwell J Crossley, Bernd Stannowski, Klaus Lips, et al. Improving the light-harvesting of amorphous silicon solar cells with photochemical upconversion. *Energy and Environmental Science*, 5(5):6953–6959, 2012.

[103] Jianzhang Zhao, Wanhua Wu, Jifu Sun, and Song Guo. Triplet photosensitizers: from molecular design to applications. *Chemical Society Reviews*, 42(12):5323–5351, 2013.

[104] Liang Shen and Hong-Fang Ji. Theoretical investigation of the photosensitization mechanisms of urocanic acid. *Journal of Photochemistry and Photobiology B: Biology*, 91(2-3):96–98, 2008.

[105] E Laura Coitiño, Andy Mella, and Gloria I Cárdenas-Jirón. Theoretical assessment of the photosensitization mechanisms of porphyrin–ruthenium (ii) complexes for the formation of reactive oxygen species. *Journal of Photochemistry and Photobiology A: Chemistry*, 294:68–74, 2014.

[106] Elise Dumont, Meilani Wibowo, Daniel Roca-Sanjuan, Marco Garavelli, Xavier Assfeld, and Antonio Monari. Resolving the benzophenone dna-

photosensitization mechanism at qm/mm level. *The journal of physical chemistry letters*, 6(4):576–580, 2015.

[107] Cesar Espinoza, Angel Trigos, and Manuel E Medina. Theoretical study on the photosensitizer mechanism of phenalenone in aqueous and lipid media. *The Journal of Physical Chemistry A*, 120(31):6103–6110, 2016.

[108] Lara Martínez-Fernández, Giovanni Granucci, Marvin Pollum, Carlos E Crespo-Hernández, Maurizio Persico, and Inés Corral. Decoding the molecular basis for the population mechanism of the triplet phototoxic precursors in uva light-activated pyrimidine anticancer drugs. *Chemistry–A European Journal*, 23(11):2619–2627, 2017.

[109] Mordechai Bixon and Joshua Jortner. Electron transfer - from isolated molecules to biomolecules: Part 1. *Advances in Chemical Physics*, 106:35–202, 1999.

[110] Alessandro Toniolo and Maurizio Persico. Efficient calculation of franck–condon factors and vibronic couplings in polyatomics. *Journal of Computational Chemistry*, 22(9):968–975, 2001.

[111] Mihajlo Etinski, Jörg Tatchen, and Christel M Marian. Time-dependent approaches for the calculation of intersystem crossing rates. *The Journal of chemical physics*, 134(15):154105, 2011.

[112] Raffaele Borrelli and Andrea Peluso. The temperature dependence of radiationless transition rates from ab initio computations. *Physical Chemistry Chemical Physics*, 13(10):4420–4426, 2011.

[113] Raffaele Borrelli, Amedeo Capobianco, and Andrea Peluso. Hole hopping rates in single strand oligonucleotides. *Chemical Physics*, 440:25–30, 2014.

[114] F Gustav Mehler. Ueber die entwicklung einer function von beliebig vielen variablen nach laplaceschen functionen höherer ordnung. *Journal für die reine und angewandte Mathematik*, 66:161–176, 1866.

[115] F Duschinsky. The importance of the electron spectrum in multi atomic molecules. concerning the franck-condon principle. *Acta Physicochim. URSS*, 7:551–566, 1937.

[116] Carl Eckart. Some studies concerning rotating axes and polyatomic molecules. *Physical Review*, 47(7):552, 1935.

[117] Sergey V Krasnoshchekov, Elena V Isayeva, and Nikolay F Stepanov. Determination of the eckart molecule-fixed frame by use of the apparatus of quaternion algebra. *The Journal of Chemical Physics*, 140(15):154104, 2014.

[118] Shuming Bai and Mario Barbatti. Spatial factors for triplet fusion reaction of singlet oxygen photosensitization. *The journal of physical chemistry letters*, 8(21):5456–5460, 2017.

[119] A. Stone. *The Theory of Intermolecular Forces*. OUP Oxford, 2013.

[120] Yingli Niu, Qian Peng, Chunmei Deng, Xing Gao, and Zhigang Shuai. Theory of excited state decays and optical spectra: application to polyatomic molecules. *The Journal of Physical Chemistry A*, 114(30):7817–7831, 2010.

[121] M Hayashi, AM Mebel, KK Liang, and SH Lin. Ab initio calculations of radiationless transitions between excited and ground singlet electronic states of ethylene. *The Journal of chemical physics*, 108(5):2044–2055, 1998.

[122] R Islampour and M Miralinaghi. Dynamics of radiationless transitions: Effects of displacement- distortion- rotation of potential energy surfaces on

internal conversion decay rate constants. *The Journal of Physical Chemistry A*, 111(38):9454–9462, 2007.

[123] Qian Peng, Yuanping Yi, Zhigang Shuai, and Jiushu Shao. Excited state radiationless decay process with duschinsky rotation effect: Formalism and implementation. *The Journal of chemical physics*, 126(11):114302, 2007.